micelle

hexagonal

surfactant

Lamellar

vesicle

SOCIETY FOR MATERIALS CHEMISTRY

Society for Materials Chemistry was established in 2007 with following aims and objectives:

(a) to help the advancement, dissemination and application of the knowledge in the field of materials chemistry,

(b) to promote active interaction among all material scientists, bodies, institutions and industries interested in achieving the advancement, dissemination and application of the knowledge of materials chemistry,

(c) to disseminate information in the field of materials chemistry by publication of bulletins, reports, newsletters, journals.

(d) to provide a common platform to young researchers and active scientists by arranging seminars, lectures, workshops, conferences on current research topics in the area of materials chemistry,

(e) to provide financial and other assistance to needy deserving researchers for participation to present their work in symposia, conference, etc.

(f) to provide an incentive by way of cash awards to researchers for best thesis, best paper published in journal/ national/international conferences for the advancement of materials chemistry,

(g) to undertake and execute all other acts as mentioned in the constitution of SMC.
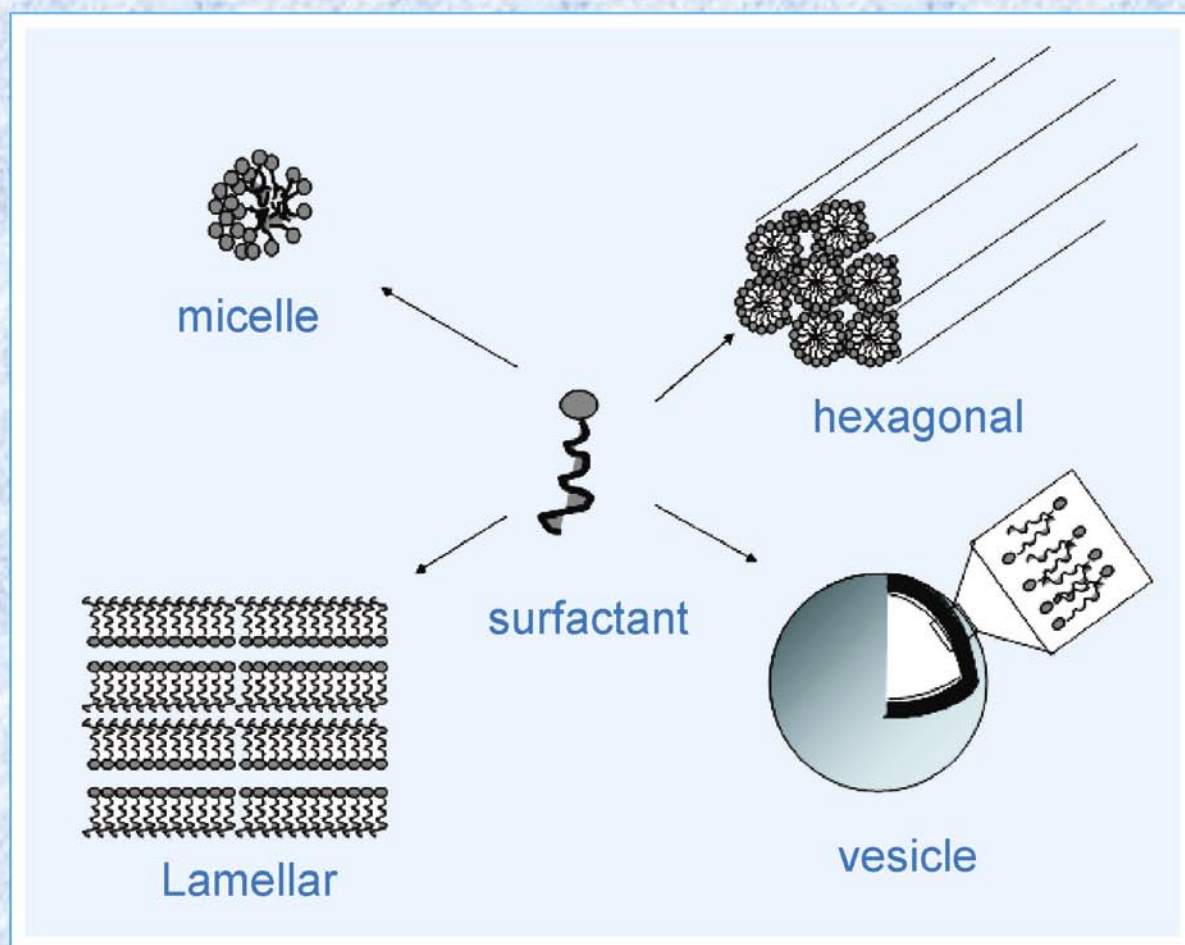
SMC Bulletin

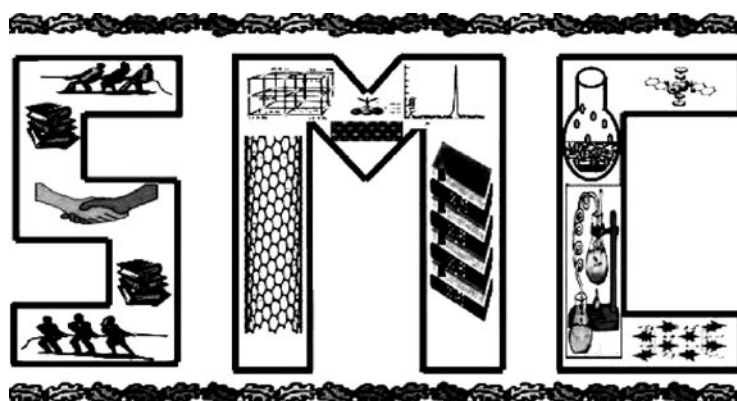## A Publication of the Society for Materials Chemistry

Volume 1   No. 1 & 2   December 2010

SOCIETY FOR MATERIALS CHEMISTRY

SMC Bulletin

Vol. 1, No.1 & 2   **December 2010**

Editorial Board

Pl☐
Front cover shows a schematic representation of a few self assembled structures of amphiphiles formed in aqueous/non-aqueous solvents.

Editorial Note

We are happy to present the inaugural issue of the SMC bulletin to the members of Society for Materials Chemistry. This issue contains eight research articles invited from various experts in the field of materials chemistry in our country. Generally, the articles deal with the synthesis, characterization and application of materials like nano gold, organic thin films, niobates and tantalates, pyrochlores and fluorescent materials. The last article, however, covers the materials chemistry aspects in pyrochemical reprocessing of spent metallic fuel (U-Pu-Zr alloy) used in Indian Fast Breeder Reactor.

A list of major materials characterization facilities available in BARC has also been included in this issue and we do hope that our members will find it quite informative.

We sincerely thank Dr. S. Banerjee, Chairman AEC & Secretary, DAE and Dr. R.K. Sinha, Director, BARC for their encouraging messages. We place on record our deep gratitude to Dr. T. Mukherjee, President, SMC, Dr. D. Das, Vice-President, SMC, and the members of Executive Committee for their valuable support, guidance and encouragement in bringing out this bulletin.

Invaluable help received from various reveiwers belonging to Chemistry Group, BARC is gratefully acknowledged. We are also grateful to head of the divisions in BARC for giving their consent during compilation of major materials characterization facilities available in BARC. Last but not the least we express our gratitude to all the authors who have accepted our request to contribute articles in the bulletin.

We suggest that the future issue of the bulletin should be thematic one and the next isuue will be on "Nanomaterials and their applications". We will appreciate receiving feedbacks from our readers on this issue.

Editors

डॉ. श्रीकुमार बॅनर्जी
Dr. Srikumar Banerjee

अध्यक्ष, परमाणु ऊर्जा आयोग
व
सचिव, परमाणु ऊर्जा विभाग
Chairman, Atomic Energy Commission
&
Secretary, Department of Atomic Energy

भारत सरकार
Government of India

October 8, 2010

MESSAGE

The evergrowing demand of materials with desired properties for advanced applications in nuclear, space, defence, aviation and transport and biomedical sectors has been providing both opportunity and challenges to the material scientists worldwide. R&D in material science has contributed significantly to the success and growth of our programme in areas like nuclear reactors, fuel cycle facilities, radiation technology applications etc. Material scientists in coordination with engineers at DAE have been playing an important role in establishing the methodologies for the development and fabrication of nuclear fuel, fuel recycle, vitrification and utilization of radioisotopes for pharmaceuticals and therapeutic use.

I am delighted to note that the Society for Materials Chemistry is going to publish its bulletin bi-annually and the inaugural issue of this bulletin will be released during DAE-BRNS 3rd International Symposium on Materials Chemistry at BARC in December 2010. I understand that the bulletin will publish feature and research articles on variety of topics in the Materials Chemistry including Nuclear Materials, Nanomaterials and Clusters, Materials for Energy Conversion, and Functional Materials in general.

I hope that the articles in SMC bulletin will highlight the advances made in the field of materials chemistry and the bulletin will be found quite informative by the scientific community especially the young researchers working in the area of materials.

My best wishes for the success of the bulletin

(Srikumar Banerjee)

अणुशक्तिभवन, छत्रपति शिवाजी महाराज मार्ग, मुंबई - 400 001, भारत
दूरभाष : +(91) (22) 2202 2543 ● फैक्स : +(91) (22) 2204 8476 / 2284 3888 ● तार: एटमर्ग
Anushakti Bhavan, Chhatrapati Shivaji Maharaj Marg, Mumbai - 400 001, India
Phone: +(91) (22) 2202 2543 ● Fax: +(91) (22) 2204 8476 / 2284 3888 ● Grams: ATOMERG
E-mail: chmn@dae.gov.in

रतन कुमार सिन्हा, एफएनएई, डी एससी (एच सी)
Ratan Kumar Sinha, FNAE, D Sc (hc)

भारत सरकार
Government of India

निदेशक, भाभा परमाणु अनुसंधान केंद्र
सदस्य, परमाणु ऊर्जा विभाग
Director, Bhabha Atomic Research Centre
Member, Atomic Energy Commission

MESSAGE

Increasing demands of newer, novel and advanced materials with tailormade properties for societal and industrial applications have been driving the growth of material science since time immemorial. In recent times the search of novel materials for advanced applications in areas like nuclear, space, defence, health, aviation and transport has provided both opportunities and challenges to the researchers in the field of materials science, where chemists have played a significant role.

BARC has ongoing programmes on materials research for harnessing power from nuclear fission, fossil fuels, solid oxide fuel cells, hydrogen and solar energy in environment friendly manner through the concerted efforts of materials scientists and engineers at the center.

I am happy to note that the Society for Materials Chemistry has planned to publish its bulletin bi-annually. I understand that the bulletin will publish feature and research articles on various topics in the field of Materials Chemistry including Nuclear Materials. I wish all success to SMC bulletin and hope that it will serve as a potent medium to highlight the advances made in the field and will be quite useful to the scientific community, particularly the young researchers working in the area of materials.

6.9.2010

(R.K. Sinha)

From the President's Desk

Dear Fellow members,

In 2006, Chemistry Division, BARC, organised the DAE-BRNS 1st International Symposium on Materials Chemistry (ISMC-2006), supported by the Board of Research in Nuclear Sciences (BRNS) and the Mumbai Chapter of Materials Research Society of India (MRSI). During this symposium the idea of forming a Society for Materials Chemistry was suggested by several eminent participants. Accordingly, the Society for Materials Chemistry (SMC) has been formed with Chemistry Division, BARC as it's headquarter. An adhoc-committee, appointed in early 2007, was instrumental in successfully organising the DAE-BRNS 2nd International Symposium on Materials Chemistry (ISMC-2008) at BARC in 2008. The present duly elected executive council assumed its charge in September 2009. SMC along with Chemistry Division, BARC, is now organising the DAE-BRNS 3rd International Symposium on Materials Chemistry (ISMC-2010) at Bhabha Atomic Research Centre during December 7-11, 2010. Meanwhile SMC has become a vibrant national scientific society with over 400 life members.

In the beginning of this year the society planned to publish a half-yearly bulletin to highlight recent developments in the field of materials chemistry and to apprise the members and the scientific community about its activities. The bulletin envisages to publish articles on various topics in the materials chemistry including nuclear materials, materials for energy conversion, high purity materials, thin films, nanomaterials and clusters, magnetic materials, carbon based materials, catalysis, surface chemistry, fuel cells materials, soft condensed materials, chemical sensors, biomaterials, organic & organometallics, polymer based materials, computational research in materials chemistry, etc.

I am happy to note that the inaugural issue is being brought out particularly when we are holding the DAE-BRNS 3rd International Symposium on Mateials Chemistry at BARC. I appreciate the efforts of the editorial team in bringing out this bulletin. I hope that the members, particularly those young researchers working in the area of materials, will find the bulletin quite informative. I expect that the bulletin will provide a platform to highlight the advances made in the field of materials chemistry and hope that the members will contribute articles in the bulletin to enrich the goals of SMC.

T. Mukherjee

CONTENTS

A Journey with Gold

Tarasankar Pal* and Sougata Sarkar

Department of Chemistry, Indian Institute of Technology Kharagpur 721302, India
*Corresponding author; E-mail: tpal@chem.iitkgp.ernet.in

Abstract

Gold in the nanoregime has provided wealth of information to the world of materials. Stabilization of gold nanoparticles (AuNP) and also its alloying find innumerable applications which are now being unfolded. The core-shell particle would be useful for spectroscopic applications. Suitable supports make AuNP a new generation catalyst for redox reactions and its attachment with biomolecules shows an avenue for drug delivery.

Keywords: gold nanoparticles, core-shell particle, aggregation, catalyst.

Gold is the noblest coinage metal and can be found in its metallic form. It has become associated with the human civilization for its fascinating luster from the antiquity. The luster is explained from the relativistic effect. The electronic transition responsible for this absorption is a transition from the 5d to the 6s level. An analogous transition occurs in Ag but the relativistic effects are lower in Ag so while the 4d experiences some expansion and the 5s some contraction, the 4d-5s distance in Ag is still much greater than the 5d-6s distance in Au because the relativistic effects in Ag are smaller than those in Au. Thus, nonrelativistic gold would be white. The relativistic effects are raising the 5d orbital and lowering the 6s orbital [1].

The first known civilization is the Egyptian one which remains associated with gold. The Romans used it for making coloured glasses, Indians used it for medication. Rutherford's infamous alpha particle experiment with gold film for elucidation of atomic structure is the one unique application of metallic gold. Michael Faraday in the year 1857 prepared gold sol [2] and kept that for the future generation for astonishing applications. Now the material world still discovers newer facets of gold for its elegance. So the journey with noble gold has become a novel strategy.

Gold and silver are almost like twins. The first one is more costly and the second one is the best conductor of electricity. They mix together in all proportions and produce gold-silver alloy. This is because of their similar lattice fringe. It is just like alcohol in water. One can physically reduce the size of metallic gold particle to a tiny nanometer (10^{-9} meter) size. The physical method to produce nanoparticles is known as 'top-down' approach. In a 'bottom-up' procedure gold compounds are chemically reduced to the metallic state. The size reduction of metallic gold particles brings astonishing properties to the nanosize gold. The surface-to-volume ratio increases and hence the surface activity is dramatically enhanced in gold nanoparticle (AuNP). This is due to the effect of drastic increase in surface atom and as a result of which the AuNPs become useful in the world of materials. The novel catalytic property, spectroscopic property etc. emerges out with the AuNPs. To represent their electronic structures the density of states need to be looked into from a different angle. The Fermi level of AuNP shifts towards the conduction band as a general case of metallic nanoparticles [3].

In this context it is pertinent to mention that the shift of Fermi level can be observed while the metallic nanoparticles become associated with nucleophiles. Stronger nucleophiles like cyanide, thiocyanate, iodide etc. affect the Fermi level to a great extent. So both the size effect (Fig. 1) as well as the effect of nucleophiles affects the shift of Fermi level in the similar sense. There happens a miraculous change in the redox property of metals (Table 1) in the nanometer size regime.

This effect is easily quantified spectrophotometrically in case of AuNP. The AuNP in question thus become vulnerable to oxidation. Hence one can dissolve gold in aqueous media without the need of any mineral acid [4]. Under these circumstances the size dependent redox and hence the catalytic property emerges out from AuNP bearing different size [5].

One can easily visualize that in a metallic nanoparticle there are many many atoms those club together. The atom in the centre of the assembly remains surrounded by atoms of the same kind. Thus the central atom becomes coordinatively saturated.
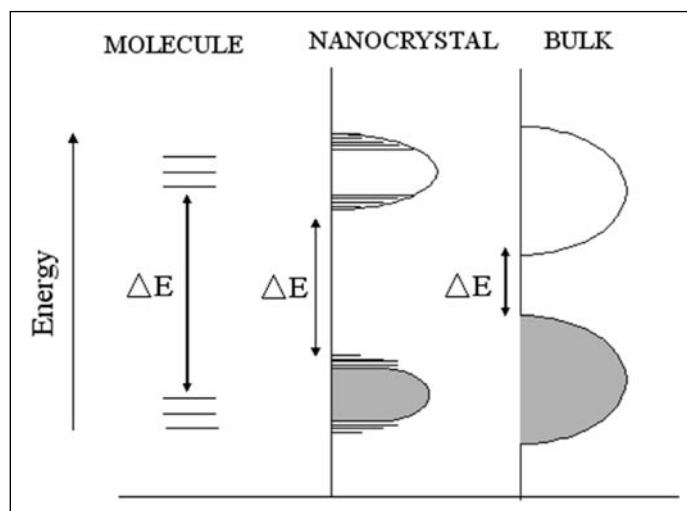
Fig. 1: Schematic representation of the density of states of a semiconductor nanocrystal as compared to a molecule or bulk material

Coordinatively Saturated Metal Atom
Coordinatively Unsaturated Metal Atom
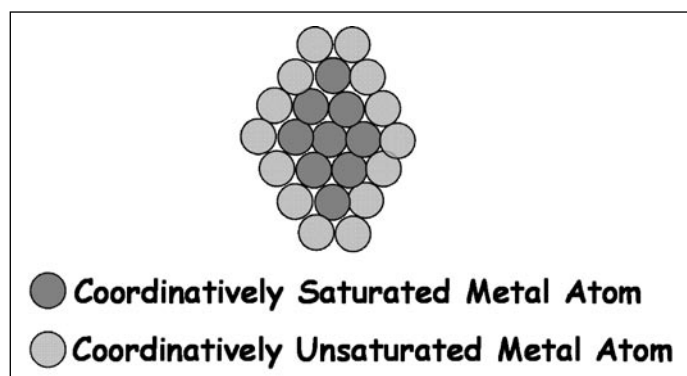
Fig. 2: Change in the number of surface atoms

This picture of the saturation of the coordination number of the central atom is different from the atoms in the surface (Fig. 2). It may be said that the surface atoms are coordinatively unsaturated because of the inherited unsaturation and high surface energy they become unstable. Hence atoms, ions, molecules are easily adsorbed onto the surface of nanoparticles. Thus nanoparticles become the wonderful carrier for the adsorbed species. There comes the beauty of drug delivery by nanoparticles. In this context AuNPs are unique [6]. There surface are not easily poisoned due to nobility of AuNP and can be monitored easily again by a spectrophotometer.

The presence of AuNP in aqueous medium can be monitored easily because of rich Plasmon absorption by the particles in the visible range of electromagnetic radiation (Fig. 3 c). This is also true for copper and silver nanoparticles (Fig. 3 a, b) . However, the surface oxidation makes the

other two coinage metal nanoparticles unsuitable for drug delivery. Anyway all the coinage metal nanoparticles in a suitable dispersion medium exhibit oscillation of their free conduction band electron upon absorption of suitable electromagnetic radiation. This is known as Plasmon absorption.

Table 1: Influence of Nucleophiles on Redox Potential of Gold

Redox Couple	Reduction Potential (Volt)
$Au^+/Au(atom)$	-1.50
$[Au(CN)_2]^-/Au$	-0.60
AuI/Au	+0.50
$[Au(SCN)_2]^-/Au$	+0.69
$[Au(Br)_2]^-/Au$	+0.96
Au^+/Au	+1.68
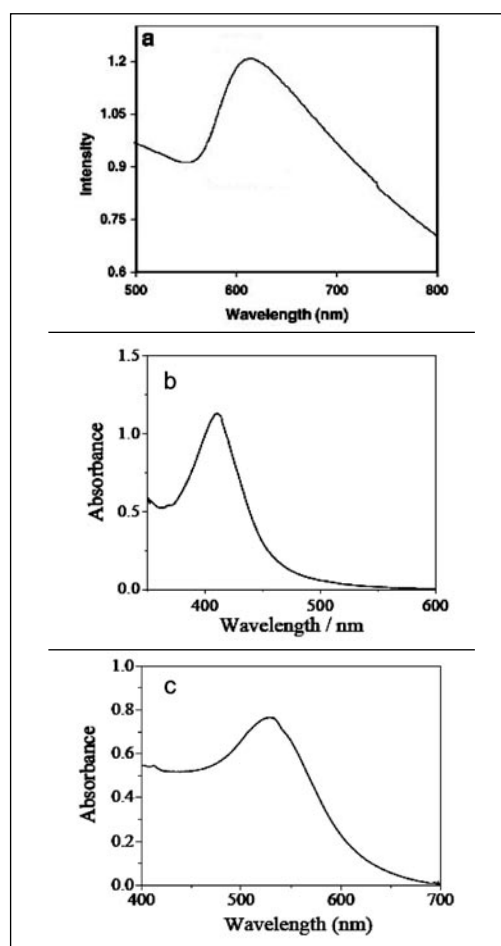
Fig. 3: Plasmon absorption band for (a) copper (b) silver and (c) gold nanoparticles.

The AuNP in dispersion shows fascinating colours in aqueous medium. The Plasmon absorption of AuNP is not observed when the size goes below sub-nanometer range. But the AuNP becomes pink in the nanometer range. Upon aggregation of AuNPs in solution they show blue colour. This is a general observation while AuNPs are with spherical geometry. In this case the major axis and minor axis of the particles are same and AuNP in dispersion show the maximum absorption at ~520 nm (Fig. 3 c). The colour of AuNP in a dispersion medium is described by Mie theory [7]. This theory has been derived by G. Mie as a consequence of the solution of Maxwell equation. The maximum absorption changes depending on the size, shape and medium of dispersion of AuNPs. The Mie theory cannot explain the colour imparted by the non-spherical particles in dispersion. There the Mie theory is the modified to explain the colour change and particle-particle interaction and Maxwell-Garnet theory gains ground [8]. When AuNP deviates from spheroid and becomes elongated with the increase in major axis it shows two Plasmon absorption bands (Fig. 4). One in the blue region near the original band position ~ 520 nm and other is in the red region > 600 nm wavelength. This band in the red region is very much susceptible to effect of the external agencies and called the longitudinal Plasmon absorption band. The band at 520 nm region appears for the transverse vibration of a non-spherical AuNP [3].
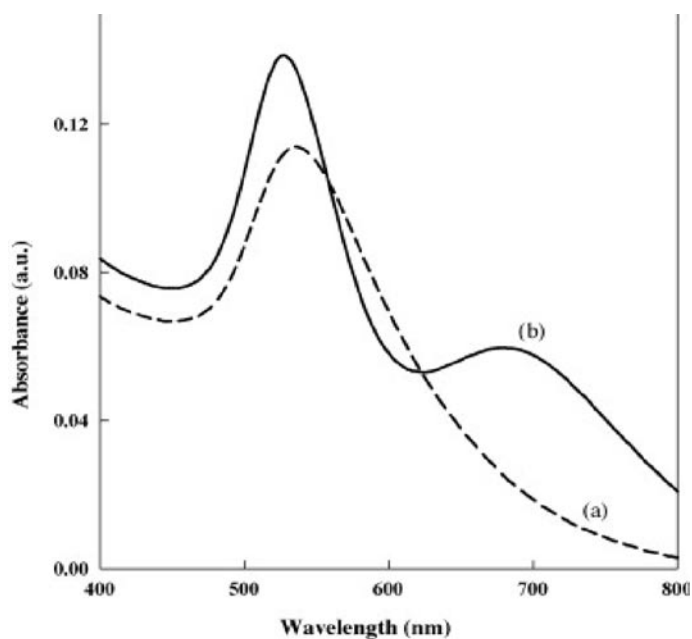
Fig. 4: Plasmon absorption band for (a) spherical and (b) rod shaped gold nanoparticles.

The particles at the nucleation stage bears very high surface energy as a result of the very high surface energy they coalesce together and goes easily to the bulk stage. The particles can be stabilized at the point of nucleation and the stabilizing agents are known as capping agents. These capping agents may be ions, surfactants, polymers and ligands. The nature of the capping agents is responsible for the morphology of the evolved particles. Again, capping agents have selectivity and they selectively cap crystal planes [9]. Thus judiciously selecting the capping agents it is now possible to produce size selective synthesis. The morphology of nanoparticles bears different surface energy and thus size selective catalysis is now the talk of the present day research [10].

Once a few nanoparticles are produced in solution the growth of nanoparticles takes place autocatalytically. This can be easily monitored for AuNP by spectrophotometry, conductivity, cyclic voltametry etc. In spectrophotometry the auto catalytic growth kinetics follow a sigmoidal curve (Fig. 5).
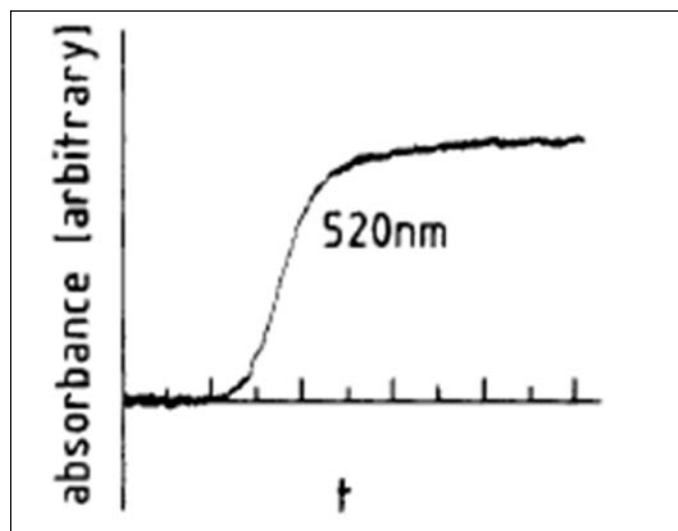
Fig. 5: Sigmoidal curve to indicate the growth kinetics of AuNPs in aqueous medium.

During growth, the particles might remain poly dispersed with wide size distribution. Then the particles might change their size at the expense of the small particles. This process of evolution of particles of comparable size has been explained by Oswald ripening [11]. There the capping agents play distinctive roles. The preparation of AuNPs with tight size distribution is now very important as the property of the particles changes with size (Fig. 4) and also with shape [3].

So far it has been discussed the nanoparticle preparation in aqueous medium. The olden literature coins them as 'hydrosol'. Now how to transfer the hydrosol of metals to a nonpolar organic medium is a challenge. This has been solved by Brust et al. and that too for AuNP taking thiol as the capping agent [12]. Thus 'organosol' has been produced. It may be spelt out that they are the ligand stabilized metal nanoparticles in organic solvents. The beauty of this organosol system is that as they can be dried into powder and redispersed again in an apolar solvent for the readymade application in organic synthesis. Thus the organosol may be looked as a molecular compound [13]. It is known that organosol is stabilized through a process which is known as 'steric stabilization' through the exploitation of long chain capping agents. There the donor atoms in the capping agent in the long chains should be chosen with care keeping the 'hard-soft' acid base theory in mind. It can be mentioned that AuNPs are best stabilized by 'S' donors and silver by 'N' donor containing capping agents. However, the length of the chains really matter to compete with the hard-soft character of the metal NPs.

It is always easy to synthesis monometallic nanoparticle. The synthesis of bi- even poly-metallic nanoparticles is possible. The bi-metallic nanoparticles may be of two types: alloyed and core-shell particles (Fig. 6). Alloying of two metals have been looked into in their nanoregimes with great care considering the lattice fringes of the participating metals as has already been mentioned. Otherwise they would be segregated. Standard reduction potential values should be considered for fabricating a core-shell bimetallic nanoparticle. The example out of Au and Ag nanoparticles would be the ideal example. The standard reduction potential of Au(III)/Au(0) is +1.50 V and that of Ag(I)/Ag(0) is +0.79 V at 25 °C. This widely different value easily speaks for the nobility of gold over silver. They form alloy in all proportion and because of the nobility, Au(III) ions are reduced easily. However co-reduction of both the metal ions would generally result in producing alloyed nanoparticles. Interesting result emerges out when Ag(I) ions are added to a solution containing pre-formed Au(0) and reversal of the experimental manipulation i.e., addition of Au(III) ions to a solution containing Ag(0) ions. In the first case under favorable situation Au core and Ag shell is obtained easily. The standard reduction potential supports the facile reduction of Ag(I) onto the pre-formed Au(0). Interestingly in the later case also Au core and Ag shell structure would be obtained. This is going to happen because of the
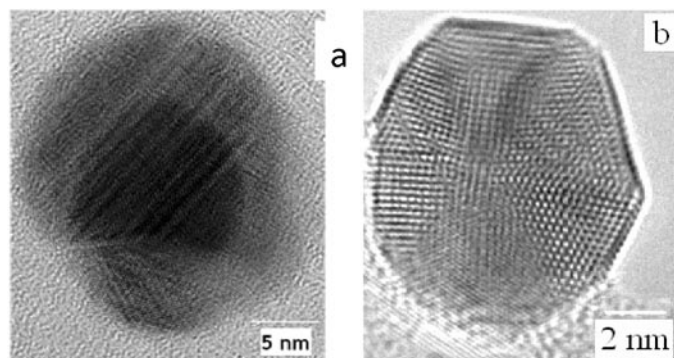
Fig. 6: (a) Core-Shell and (b) Alloy structure.
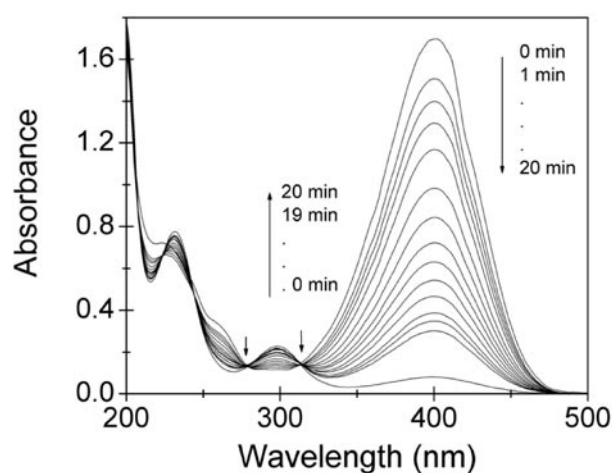
Fig. 7: UV-Vis spectra for the reduction of 4-nitrophenol measured at 1 min interval using Au nanoparticles as catalyst. Condition: [4-NP] = 10^{-4}M, [NaBH$_4$] = 6.67 × 10^{-3} M, Au nanoparticles 10 μL.

oxidation of pre-formed Ag(0) by the added Au(III) ions. In a special cases hollow core shell [14], or inverted [15] or normal core shell structures [16] will emerge out.

Gold nanoparticle has now been recognized as a magic particle in the world of nanoscience and nanotechnology. While nanoscience is still on the making to supply functionalized materials of AuNPs as a deliverable for variety applications eventually it becomes nanotechnology. There gold nanoparticle plays a pivotal role. Well documented quantum size effect with Au NPs smaller than 2 nm has already shown promise in different walks of science. Haruta's golden discovery [17] has stimulated the world of catalysis bringing newer possibilities. However, side by side the model 4-nitrophenol to 4-aminophenol reaction (Fig. 7) has proved by now how good your Au NP catalyst is [18].

References

1. P. Pyykko, J. Desclaux, *Accounts of Chemical Research*, 12 (**1979**) 276

2. M. Faraday, *Phil. Trans. Roy. Soc.*, 147 (**1857**) 145.

3. S. K. Ghosh, T. Pal, *Chem. Rev,* 107 (**2007**) 4797.

4. T. Pal, N. R. Jana and T. K. Sau, *Corrosion Sci.*, 39 (**1997**) 981.

5. T. Pal, T. K. Sau and N. R. Jana, Langmuir, 13 (**1997**) 1481.

6. C. A. Mirkin et al. *Nature,* 451 (**2008**) 553.

7. G. Mie, *Annal. Phys.,* 5(**1908**) 377.

8. J. C. Maxwell Garnett, *Philos. Trans. R. Soc.*, 203 (**1904**) 805; Philios. Trans. R. Soc., 205 (**1906**) 237.

9. T. Pal et al. *J. Phys. Chem. C* (**2010**) Communicated.

10. M. A. Mahmoud, B. Snyder and M. A. El-Sayed, *J. Phys. Chem. Lett.*, 1 (**2010**) 28.

11. R. Finsy, *Langmuir,* 20 (**2004**) 2975.

12. M. Brust, M. Walker and D. Bethell. D. J. Schiffrin, R. Whyman, *Chem. Commun.* (**1994**) 801.

13. S. Nath, S. Jana, M. Pradhan and T. Pal, *J. Coll. Interface Sci.*, 341 (**2010**) 333.

14. J. Zeng, Q. Zhang, J. Chen and Y. Xia, *Nano Lett.*, 10 (**2010**) 30.

15. W. Stefanie, F. Polzer, Y. Lu, Y. Mei and M. Ballauff, *J. Phys. Chem. C,* 114 (**2010**) 8814 .

16. N. Toshima et al. *J. Phys. Chem. C,* (**2010**) ASAP.

17. M. Haruta, T. Kobayashi, H. Sano and N. Yamada, *Chem. Lett.,* 16 (**1987**) 405.

18. N. Pradhan, A. Pal and T. Pal, *Colloid Surf. A,* 196 (**2002**) 247.

Smart Materials by Exploiting Molecular Self Assembly

P. A. Hassan
Chemistry Division
Bhabha Atomic Research Centre, Trombay, Mumbai-400 085
Email: hassan@barc.gov.in

Abstract

Self assembly of amphiphiles plays a key role in making and organizing materials with controlled size, shape and order. This article put together some of the important developments in this area with special reference to the activities at Chemistry Division, Bhabha Atomic Research Centre. The structural polymorphism in a variety of amphiphilic systems comprising surfactants, block copolymers or polyelectrolyte-surfactant complexes were investigated by neutron scattering and other complementary tools. Methods have been developed to fine tune the size and shape of aggregates and use them as micro-reactor for the synthesis of nanostructured materials. Surfactant assisted growth of pentagonal silver nanorods have been investigated. Applications of self assembled materials in drug delivery and emerging areas were discussed.

Keywords: self assembly, amphiphile, surface functionalization, silver nanorod.

Introduction

Self-assembly is a common fundamental process whereby non-covalent interactions among amphiphilic molecules control the formation of organized, dynamic, nano-scale structures. This phenomenon is very common in many natural and synthetic formulations comprising biological molecules (lipids), surfactants, block copolymers, liquid crystals and so on. Amphiphiles are molecules possessing distinct hydrophilic and hydrophobic parts. Due to this nature, under certain conditions, they have the ability to accumulate at interfaces thereby changing the properties of the surface or self assemble in to structures with a few nanometers in dimension, at least in one direction. Understanding the properties of self assembled structures and methods for their preparation and structural characterization are key both to their direct utilization and to their exploitation in creating other functional materials and devices. With this objective, we have been investigating the molecular and thermodynamic parameters that control the structure of various organized assemblies and its role in developing advanced materials with tailor made properties. This article is divided in to three parts; the first part deals with tuning the microstructure of self assembled soft materials, second part discusses synthesis of nanostructured materials using self assembly and finally a few biotechnological applications of self assembly.

Structure and Dynamics of Organized Assemblies

Much of the natural materials are product of organized molecular assemblies and humans are the best example of it. Understanding the microstructure and dynamics of molecular self assembly is important for its applications in creating other functional materials and devices. Surfactant molecules (amphiphiles) can spontaneously assemble into a gamut of spatially organized structures, in both aqueous and non-aqueous solvents. Fig. 1 shows schematic representation of a few self assembled structures of surfactants in a suitable solvent.

The geometry of the aggregates depends broadly on various factors like nature of the surfactant molecule, surfactant concentration, ionic strength of the solution, nature of the counter-ion etc. The question of what will be the preferred geometry of the aggregates formed in a surfactant-water system was investigated in detail. As a result, some models have emerged which are helpful in organizing the results and predicting the structure of supramolecular assemblies formed in surfactant solutions. At the heart of understanding this phenomenon lie considerations regarding the packing of the surfactant molecules in the aggregates and the role of the bending elastic energy of the surfactant monolayers [1].

The aggregation of amphiphiles into various structures such as micelles, bilayers, vesicles etc. arise from the interplay of two opposing forces. The 'hydrophobic effect' of the hydrocarbon tails tends to bring the molecules

closer together so as to avoid any contact with water, i.e., minimizing the area-to-volume ratio. On the other hand, the repulsion between the hydrophilic headgroups tends to maximize the area-to-volume ratio. The repulsive interactions arises form the 'solvation' of the head groups which will tend to keep the hydrophilic part away from each other.
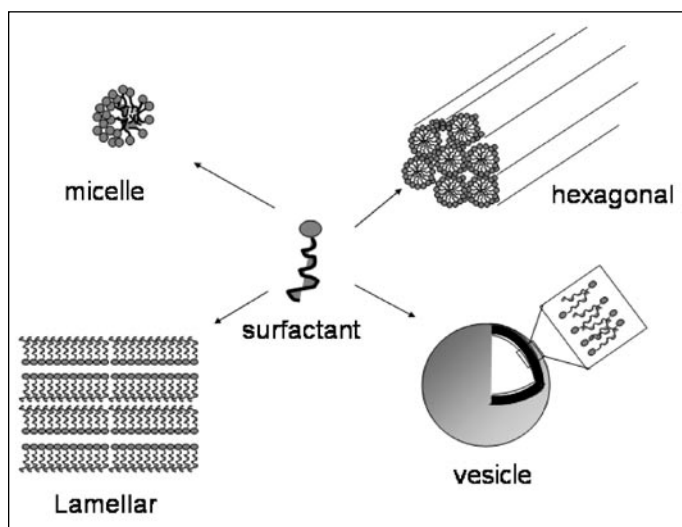

Fig.1: Schematic representation of a few self assembled structures of amphiphiles formed in aqueous/non-aqueous solvents.

In the case of ionic surfactants, there is an additional contribution from the electrostatic repulsion of the head groups which will further increase the effective head group area per molecule. The shape of the aggregate that best satisfies the above two demands depends primarily on three factors, namely, the volume (V) of the hydrophobic part, length (L) of the hydrophobic chain and the effective head group area (a) of the surfactant molecule.

The electrostatic contribution to the free energy of formation of micelles can be influenced by the addition of electrolytes or co-surfactants. As a result, the characteristics of the aggregates can be easily controlled by the changes in the solution conditions such as temperature, concentration and ionic strength. Charged spherical micelles can grow into rod-like structures by the addition of electrolytes that shields the electrostatic repulsion. The addition of electrolytes decreases the effective repulsion between head groups of surfactants thereby inducing a structural transition in micelles. Conventional electrolytes influence the electrostatic free energy by changing the ionic strength of the medium while co-surfactants or hydrophobic salts may influence the free energy by a decrease of the surface

charge density. Typically, addition of substantial quantities of inorganic electrolytes is necessary to induce the formation of rod-like micelles. However, only millimolar quantities of hydrophobic salts are sufficient to induce the transition from spherical to rod-like micelles. Appropriate hydrophobic salts contain an aromatic counterion that adsorbs on the surface of the micelles and thereby decreases their surface charge density. A series of hydrophobic salts that induces structural changes in both cationic and anionic micelles have been reported [2-4]. In particular, the feasibility of tuning the length of rod-like micelles from a few nanometers to about 100 nm by judicial choice of additives has been demonstrated. Typical additives for anionic micelles include aniline hydrochloride (AHC) and its derivatives such as o-toluidine hydrochloride (OTHC), m-toluidine hydrochloride (MTHC) and p-toluidine hydrochloride (PTHC). Fig. 2a shows typical small angle neutron scattering (SANS) spectra of micellar solutions that contain globular and rod-like assemblies. The variation in the lengths of rod like micelles (L_m) formed by sodium dodecyl sulfate (SDS) micelles (50 mM) at different concentrations of hydrophobic salts OTHC and MTHC (x_{salt} is the molar ratio of salt to surfactant) are depicted in Fig. 2b. Ortho and meta isomers of the salt show appreciable difference in the growth behavior at equal salt concentrations. The propensity for the strong growth of micelles in the presence of OTHC and MTHC is evident from the change in micellar length at salt concentrations much lower than that of surfactant; i.e $x_{salt} < 1$. The high degree of charge neutralization provided by these salts is a manifestation of the fact that the aromatic counter ions are adsorbed on the surface of the micelles. When the substitution is at the meta position, i.e., for MTHC, micellar growth is favored at lower salt concentrations than for OTHC. The variation in growth behavior is explained in terms of the difference in the chemical environments of the substituents at the ortho and meta positions. Micellar parameters obtained from light and neutron scattering experiments at different temperatures also support enhanced growth of micelles in the presence of MTHC as compared to OTHC. Stimuli sensitive supramolecular aggregates can also be created by elf assembly of surfactants and hydrophobic amino acids [5,6]. The above approach is not limited to the formation of short rigid rods but can be extended to form long, flexible worm-like micelles. Cryogenic temperature transmission electron microscopy (cryo-TEM) of vitrified samples permits the visualization of long polymer like assemblies in certain surfactant solutions. The rheological properties of entangled

wormlike micellar solutions are similar to those of semi-dilute polymer solutions with a difference that the micelles are dynamic in nature (breaking and recombining rapidly). Wormlike micelles can thus be viewed as substitutes for polymers in applications that require thickening or drag reduction. For example, wormlike micellar solutions are currently being used as hydraulic fracturing fluids for enhanced oil recovery. Thus, self assembly can be employed to modulate the flow behavior of fluids with high sensitivity to temperature as the polymer-like structure is formed through non-covalent interaction. Microstructure, dynamics and several applications of worm-like assemblies have been reviewed recently [7].

in the molecular weight of the polymer in the two blocks offer a way to control the dimensions of the micelles. Several groups have investigated the synthesis, properties and applications of a wide variety of block copolymer assemblies. Structural transitions in such block copolymer assemblies can be induced by changes in the solubility of the two polymer blocks [8,9].

Moulding Advanced Materials through Self Assembly

One immediate consequence of self assembly is its ability to create hydrophobic and hydrophilic compartments in fluids. These compartments can be used as solubilization sites for various reactants and hence as a microreactor for

Fig. 2: a) SANS spectra of sodium dodecyl sulfate (SDS) micelles (globular and rod-like) with and without p-toluidine hydrochloride (PTHC). b) Estimated length (L_m) of rod-like micelles formed by SDS in the presence of different organic additives, o-toluidine hydrochloride (OTHC) and m-toluidine hydrochloride (MTHC)

The maximum extended length of a hydrocarbon chain in a conventional surfactant molecule is typically 10-30 Å. This limits the maximum radius that can be attained for a rod-like assembly. To expand the size scale of the aggregates formed, new class of amphiphilic materials can be employed, namely block copolymers. These are typically polymers having different solubility characteristics (say poly-ethylene and poly-propylene) linked together by covalent bond. The difference in the solubility of the two segments drives them in to self assembled structures similar to those of surfactants but with a larger size compared to conventional micelles. Thus, these block copolymers can be viewed as surfactants for "macro" micelles. Changes

different classes of materials such as metals, semiconductors, polymers and ceramics. Technological developments in various fields, such as adsorption, separation, catalysis, drug delivery, sensors and photonic crystals require the development of ordered porous materials with controllable pore dimensions. Mesoporous materials with pore dimensions at the scale of a few nanometers can meet the demands of the growing applications emerging in processes involving large molecules such as proteins and petroleum products. Zeolites or microporous materials, whose pore sizes are at the scale of a few angstroms, cannot meet these demands. These motivations led to the development of mesoporous materials. Mesoporous silicates prepared using

a surfactant self assembly template is one commentable development in this area. Quaternary ammonium cationic surfactants such as cetyltrimethylammonium bromide (CTAB) were used as templates to prepare highly ordered mesoporous silicate molecular sieves under hydrothermal conditions. The pore size in such kind of materials can be tuned in the range of a few tens of nanometers. Several excellent reviews have summarized the synthesis, characterization, and applications of mesoporous silicates [10]. The organic-inorganic self-assembly in the precursors of such material is driven by weak noncovalent bonds such as hydrogen bonds, van der Waals forces, and electrostatic interactions between the surfactants and inorganic species. It is reported that a synergetic self assembly between organic surfactants and inorganic precursors is generally involved in the formation of inorganic/organic mesostructured composites. Removal of surfactants from the composite material by heat treatment leads to the formation of highly ordered mesoporous materials. Thus, cooperative self-assembly of surfactants and additives is particularly essential for the formation of highly ordered mesostructures. With the advances in the knowledge on the surfactant self-assembly, the mesoporous materials can be rationally designed and the synthesis can be controlled. Thus, cooperative assembly of organic-inorganic composites not only provides new materials with controlled ore dimension but also opens avenue for the generation of a variety of technologically important materials with highly ordered nanochannels, large surface area catalysts and attractive liquid-crystal structures. Surfactants have also been employed as structure directing agents for the synthesis various inorganic and polymeric materials. Conducting polymers such as polyaniline (PANI) have been attracting considerable attention in recent years due to their potential as tailorable semiconducting materials for use in electronics and optoelectronics. One of the problems associated with successful application of this polymer is the difficulty in processing of this material due to its very low solubility in different solvents. One approach to improve processability of this material has been to prepare them as colloidal nanoparticles. PANI nanoparticles were synthsised in anionic micelles of varying size to control the particle size of the polymer [11]. Polymerization of aniline in micelles of different size leads to colloidal PANI particles of varying size. A direct correlation between the sizes of the polymer particles and sizes of the micelles was observed. The ability to manipulate the shapes of inorganic nanoparticles remains an important goal of modern materials science. Fig. 3 shows a representative TEM image of silver nanocrystals prepared by the reduction of silver salts in a surfactant medium. Of particular interest is the production of silver nanorods by controlling the reaction conditions. Surfactant assisted growth of silver nanorods with aspect ratio 5 to 20 have also been investigated [12]. The role of crystal defects (twinning) and preferential adsorption of surfactants in inducing the nanorod formation is identified.

Interfacial Engineering for Diagnostics and Therapy

Colloidal particles with well defined particle size, morphology, microstructure and surface characteristics are currently offering great promise as supports in a large number of biotechnological, pharmaceutical and medical applications such as diagnostics (assays), bioseparation, NMR imaging, cosmetics and drug delivery systems (DDS) [13]. For this reason, a large amount of work has been done to the design and preparation of colloids with appropriate properties for interacting with biologically active macromolecules. Some of the commonly used strategies for the development of such materials include polymerization in microheterogeneous media to produce colloidal dispersions, interfacial modification of the preformed particles, self assembled structures of surfactants and block copolymers, polyelectrolyte-surfactant complexes and engineered multifunctional dendrimer particles.
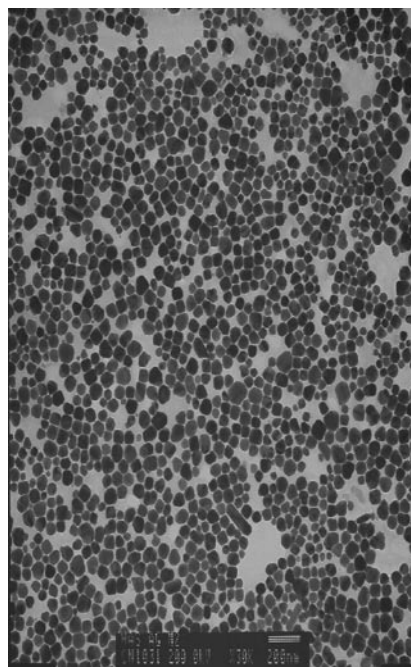

Fig. 3: Silver nanocrystals prepared by the reduction of silver nitrate in the presence of sodium dodecyl sulfate micelles

The production of surface-functionalized materials has long been motivated as a result of their application in technologies that require the interaction of biomolecules with a given substrate either as film or as colloidal support. This obviously concerns the biotechnological field where one often wants to immobilize temporarily or permanently a biomolecule on a suitable substrate. Surface functionalization of materials is of is of great importance in bio-diagnostics whether it is used as colloidal particles as in latex agglutination assays or as solid-phase supports as in immunoassays. Bio-diagnostics involves the detection of biological macromolecules such as proteins, viruses, bacteria, toxins etc through a bio-recognition process. In general, it involves biological recognition event that is coupled with a suitable transducer to monitor the recognition process. The biological component gives rise to a signal as a result of the biochemical reaction of the analyte which is detected by the transducer. This can be used with or without amplification for the estimation of the concentration of the analyte in a given sample. The specific interaction between an antigen and antibody (biological macromolecules) has been made use of in the selective estimation of various proteins. Stable immobilization of one of the assay reagents (biomolecules) on a suitable substrate with complete retention of their biological recognition properties is a crucial step in developing efficient biosensors. Polystyrene is a commonly used solid support for immobilization of antibodies in immunoassays [14]. There are different approaches for immobilizing biomolecules on polystyrene surfaces. Among them, passive adsorption and covalent coupling are the most common methods. Passive adsorption predominantly makes use of the hydrophobic interaction between the solid phase and the biomolecules. Different covalent immobilization procedures have been reported in literature. An active amino group can be introduced to polystyrene by nitration of the aromatic ring followed by reduction. The amino polystyrene was further activated by chemical reactions such as diazotization and the resulting surface was used for antibody immobilization. Covalent binding using bifunctional cross-linking agents such as glutaraldehyde and activation of the surface using isocyanate or carbodiimide are also employed. Most of the covalent immobilization approaches are tedious and involve severe chemical treatment or multistep procedures. Thus, there is a need to develop simple, yet efficient immobilization strategies since this could offer immense potential in diagnostic applications. Surface modification through self assembled monolayers, adsorption of polymers or nanoparticles with specific functionalities and grafting of functional materials etc. are also used for efficient binding of biomolecules on the surfaces. Amine/imine functional groups of polyaniline modified surfaces have shown improved binding of triiodothyronine(T_3) antibodies on polystyrene surface that can be used as a substrate for the detection of human thyroid hormone in nanograms/ml level using radioimmunoassay (RIA) [15]. The percentage of rabbit IgG coated on polyaniline modified tubes, as estimated using IgG-^{125}I, was found to be 90 ± 1.8 % as compared to 42 ± 5 % in unmodified tubes. The percentage binding of T_3-^{125}I to antibody coated on polyaniline-modified polystyrene tubes through physical adsorption was found to be 36 ± 2 % as compared to 28 ± 4 % that was observed for unmodified tubes. A schematic representation of the functionalized polystyrene surface using polyaniline for the development of immunoassays is depicted in Fig. 4. The role of functionalized surfaces using polyaniline in immunoassays is many fold; nanoparticulate adsorption enhances the surface roughness leading to enhanced surface area, electrostatic binding of antibodies due to the charged nature of the surface that varies with the pH of deposition and covalent or non-covalent binding of antibodies through coupling of amino group.
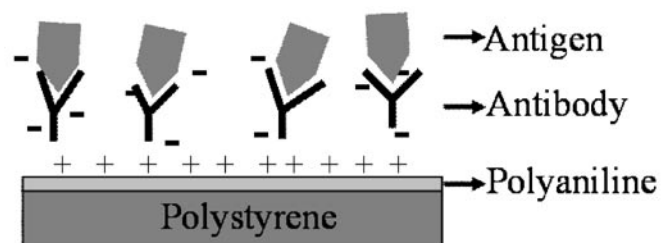
Fig.4: Schematic representation of the surface modification of polystyrene using polyamine for enhanced binding of antibodies in immunoassays

The formation of particulate systems with defined particle size and shape is of eminent interest in drug delivery applications. For example, particles utilized as carriers in drug delivery applications generally should be in the nanometer range, uniform in size and, preferably, spherical in shape to enhance their ability to cross cell membranes and reduce the risk of undesired clearance from the body through liver and spleen. Surfactants and block copolymers spontaneously assemble in to structures such as micelles, vesicles, microemulsions and liquid crystalline phases. These assemblies have a unique structure in which hydrophilic and hydrophobic compartments with

a dimension of a few nanometers to tens of nanometers are dispersed in a solvent. The issue most frequently addressed in pharmaceutical products by these systems is solubility. A low solubility and poor dissolution characteristics of many drugs reduces their bioavailability. Other issues such as drug payload, protection against degradation by endogenous enzymes and excretion of active ingredient by the immune system are also addressed with the help of novel drug delivery systems. It appears that the structural features of amphiphilic assemblies can be advantageously utilized to overcome the drug delivery challenge. Redkar et al reported that multilamellar vesicles (onion phases) that are capable of drug encapsulation can be prepared from a biodegradable surfactant PEG-8 Distearate (PEG-8-DS) [16]. Sumatriptan succinate (SS), a potent antimigraine drug is encapsulated in the aqueous layers of vesicles. Drug loaded vesicles were prepared by shearing lyotropic lamellar phases of the surfactant in presence of drug. The onion phases were characterized by polarized microscopy and small angle neutron scattering (SANS). The bilayer spacing of the vesicles of PEG-8-DS was observed to be 72 Å from SANS spectra. SANS study of the drug encapsulated vesicles reveals that upon encapsulation of drug, the bilayer spacing is increased to about 79 Å. Self assembled drug delivery systems with suitable surface functionalities have been prepared through electrostatic complexation of anticancer drug doxorubicin[17].

Conclusions

In conclusion, self assembly offers a powerful method for creating several nanostructured materials with emerging applications. This amphiphilic nature of surfactants makes them attractive material for interface modification as well as formation of new self assembled structures in solution. Knowledge of the behavior of molecules at the interfaces and how it affects the chemical and physical phenomena of a multiphase system are important to fine tune the formulations for specific applications. From the large variety of applications in different areas, it is evident that self assembly attracts the attention of chemists, physicists, biologists and chemical engineers. By proper manipulation of intermolecular forces, it is possible to fine tune the size and shape of self assembled structures. Self assembly goes a long way in controlling the geometry of other functional materials such as polymers, metals, ceramics and semiconductors. Surface functionalization with appropriate reactive groups has now become a prerequisite in the handling of materials for biotechnological applications.

References

1. P. Schurtenberger, *Curr Opin Colloid Interface Sci* 1 (**1996**) 773.

2. G. Garg, P. A. Hassan, V. K. Aswal and S. K. Kulshreshtha, *J. Phys. Chem* B, 109 (**2005**) 340.

3. P. A. Hassan and J. V. Yakhmi, *Langmuir,* 16 (**2000**) 7187.

4. P. A. Hassan and C. Manohar, *J Phys Chem B*, 102 (**1998**) 7120.

5. G. Verma, V. K. Aswal, S. K. Kulshreshtha, P. A. Hassan and E. W. Kaler, *Langmuir* 24 (**2008**) 683.

6. G. Verma, V. K. Aswal and P. Hassan, *Soft Matter*, 5 (**2009**) 2919

7. S. Ezrahi, E. Tuval and A. Asrin, *Adv. Coll. Interface Sci*. 128 (**2006**) 77.

8. R. Ganguly, V. K.Aswal, P. A. Hassan, I. K. Gopalakrishnan and J. V. Yakhmi, *J. Phys. Chem. B*, 109 (**2005**) 5653.

9. R. Ganguly, V.K. Aswal and P.A. Hassan, *J. Colloid and Interface Sc*. 315 (**2007**) 693.

10. Y. Wan and D. Zhao, *Chem. Rev*. 107 (**2007**) 2821.

11. P. A. Hassan, S. N. Sawant, N. C. Bagkar, and J. V. Yakhmi, *Langmuir,* 20 (**2004**) 4874,

12. C. Ni, P. A. Hassan and E. W. Kaler, *Langmuir*, 21 (**2005**) 3334.

13. C. Pichot, *Curr Opin Colloid Interface Sci* 9 (**2004**) 213.

14. S. E. Kakabakos, E. Livaniou, G. P. Evangelatos and D. S. Ithakissios, *Clin. Chem.*, 36 (**1990**) 492.

15. T. Karir, P. A. Hassan, S. K. Kulshreshtha, G. Samuel, N. Sivaprasad and M. Venkatesh, *Anal. Chem*. 78 (**2006**) 3577.

16. M. Redkar, P. A. Hassan, V. K. Aswal and P. Devarajan, *J. Pharm. Sci*. 96 (**2007**) 2436

17. J. Bhattacharjee, G. Verma, V. K. Aswal and P. A. Hassan, *Pramana - Journal of Physics* 71 (**2008**) 991.

Evaporated Organic Thin Films

Monica Katiyar* and Saumen Mandal

Department of Materials Science and Engineering & Samtel Center for Display Technologies
Indian Institute of Technology, Kanpur 208016, UP
*Corresponding author; E-mail: mk@iitk.ac.in

Abstract

Organic thin films are life line of organic electronics which is a promising technology for large area and low cost applications such as large area displays, solid state lighting, solar cells, and RFID tags, etc. Materials chemistry of organic thin films is not only determined by the constituent molecules, but also by the processing technologies used to make them. In this paper we study the relationship between various processing parameters and film structure of evaporated pentacene films. Our results indicate that for organic thin films of small molecules, microstructure and crystallinity is determined by the nucleation density and interaction with the substrate. This is a consequence of weak van der Waals forces responsible for crystallization in organic materials, and its effect on relative substrate-film and film-film interaction.

Keywords: organic electronics, thin films, Pentacene, large area display, organic thin film transistor, AFM.

Introduction

Organic electronics is relatively young technology that has been used commercially in many products, eg. displays in cameras, mobiles, etc. It continues to hold promise for many more large area and low cost applications such as large area displays, solid state lighting, solar cells and RFID tags, etc. It has also opened a new research area in materials chemistry of organic thin films. The organic material may be a small molecule or polymer [1], and its thin film has a distinct structure. Organic chemists can control the exact electronic structure of molecules (oligomers or polymers). But as we move from molecules to materials, more often than not, organic materials (mostly in thin film form) exhibit properties very different from their constituent molecules. Therefore, there is need to understand materials chemistry of organic thin films. Moreover, materials chemistry is not only determined by the constituent molecules, but also by the processing technologies used to make organic thin films. At IIT Kanpur, depending on applications and organic materials of interest we are focusing on three technologies, viz. conventional physical vapour deposition, spin coating, and printing.

In this article, we focus on organic thin films of evaporated small molecules. The case study of pentacene (Fig. 1), as it is an important material for organic thin film transistors, is discussed here. The high electron mobility ($\sim$2 cm^2/Vs) of pentacene has led to intensive research on various aspects including electronic structure [2], charge transport mechanisms [3] and thin film nucleation [4] and growth [5]. The field effect mobility of pentacene has been attributed to depend on its crystal structure [6], morphology [7] and grain size [8]. These properties can be tuned by changing the nature of substrate [9, 10], deposition rate [11], substrate temperature [6], thickness and surface treatment [12, 13]. Generally two different triclinic phases, thin film (d = 1.54 nm) and bulk (d = 1.44 nm), are observed in evaporated pentacene films [14, 15]. Thin film phase has been argued to be responsible for higher mobility [6, 16] due to lower spacing between two pentacene molecules. However, there is a report showing phase has no effect on field effect mobility [8]. Similarly, the role of grain size and grain boundary is also controversial. Generally grain boundary acts as a barrier for hole hopping. So, theoretically larger the grain size, higher will be mobility [17, 18]. However, some reports are not in agreement with the above explanation in case of organic systems [8, 19]. Depending on the deposition parameters, five different morphologies, viz. dendritic, lamellar, pyramidal, inclined, giant grain, have been observed in AFM studies [7, 8]. In lamellar structure, pentacene molecules remain flat on SiO$_2$ substrate, which leads to lower mobility. Whereas, in case of other morphologies they align with an angle of 17.1 or 25.2° with surface (SiO$_2$ substrate) normal [7]. Dendritic, pyramidal and inclined morphologies show higher mobilities. It is argued that giant grain morphologies have lower mobilities due to large amount of cracks and defects.

Since small molecule organic materials form molecular crystals held by van der Waal forces, it is possible to deposit
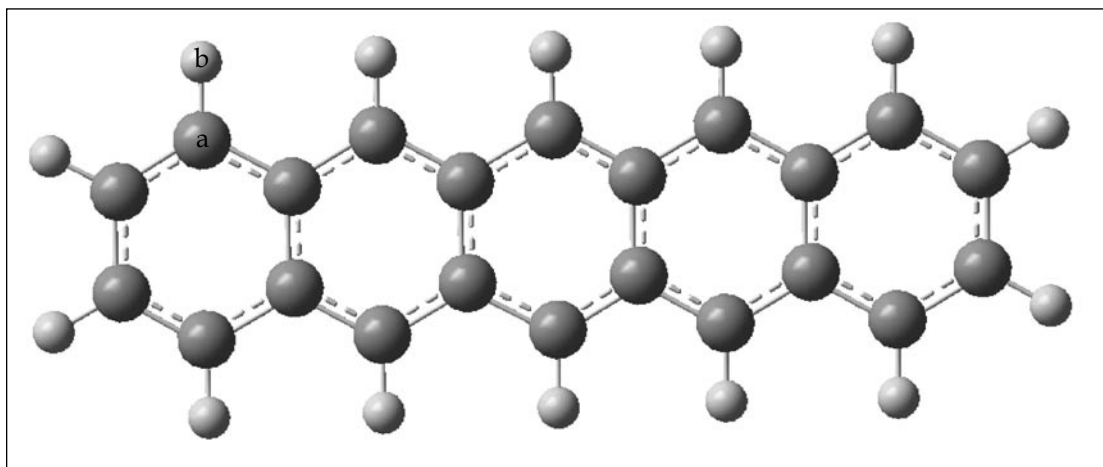
Fig. 1: Molecular structure of pentacene. a is carbon and b is hydrogen atom.

crystalline films at low temperatures compared to inorganic thin films. We present variation of film structure of pentacene as a function of substrate temperature (60-70 °C), deposition rate (0.5-1.5 nm/min), octadecyltrichlorosilane (OTS) treatment, and film thickness. These results are correlated with the electronic properties of pentacene film – especially field effect mobility. It has been reported that field effect mobility of pentacene can vary by orders of magnitude by changing the thermal evaporation parameters - nature of substrate, deposition rate, substrate temperature and surface treatment. The field effect mobility of pentacene is measured from a top contact organic thin film transistor (OTFT), and it is correlated with the structural features observed in pentacene films, such as crystal structure, grain size and morphology. Our discussion will highlight the differences between inorganic and organic thin film deposition.

Experimental

Heavily doped n type Si (100) with 200nm SiO_2 layer was taken as substrate. After RCA cleaning, 50 nm thick pentacene film was deposited on SiO_2 surface in a thermal evaporator with vacuum level of 3×10^{-6} mbar. Before deposition, substrate was preheated at 100 °C to eliminate adsorbed water [20]. Three experiments were done, in the first set of experiments pentacene deposition was varied from 0.5 to 1.5 nm/min while substrate temperature was kept constant at 70 °C. In the second set, the substrate temperature was 70 °C and 60 °C at 1.5 nm/min deposition rate. Finally, OTFT were fabricated on untreated and octadecyltrichlorosilane (OTS) treated SiO_2 at 1.5 nm/min and 70 °C, while pentacene thickness was kept 35 and 50nm.

For OTS treatment, 0.1M solution was first made by adding OTS in chloroform [13]. The Si substrate was kept in the solution for 24 hours. After that, the substrate was cleaned by chloroform and placed in the thermal evaporator for pentacene deposition. No preheating was performed for OTS treated substrate, because it is already hydrophobic. For top contact OTFT, gold source and drain contacts were fabricated using shadow masking in a thermal evaporator with vacuum level of 3×10^{-6} mbar. Top contact OTFT was characterized using Keithley 4200 in air. Pentacene crystal structure is characterized using X-ray diffraction (XRD). XRD was performed with grazing angle 2°; and with a scan rate 0.05°/min to observe crystallinity of pentacene film. Morphology was observed using Atomic Force Microscopy (AFM) analysis.

Results & Discussion

Effect of deposition rate

Fig. 2 depicts change in the field effect mobility of pentacene as deposition rate is changed from 0.5 to 1.5nm/min at 70 °C substrate temperature. The mobility improves by two orders of magnitude. This is concomitant with the change in crystal structure from a mixture of bulk phase and thin film phase to prominent thin film and bulk phase as shown in Fig. 3, but thin film phase is dominant at higher deposition rate. Change in film morphology and grain size is shown in Fig. 4. Morphology is dendritic in all cases, but grain size and intergranular spacing is changing with deposition rate. For 0.5 nm/min, spacing between the grains is large. Increase in the deposition rate to 1.5 nm/min results in decrease of intergranular spacing and grain size.
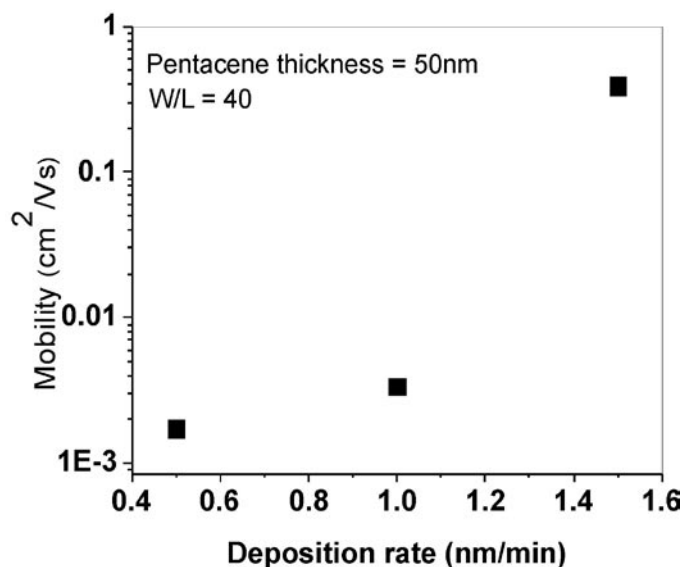
Fig. 2: Change in mobility of pentacene based OTFT as a function of deposition rate. Substrate temperature is 70 ^{0}C.
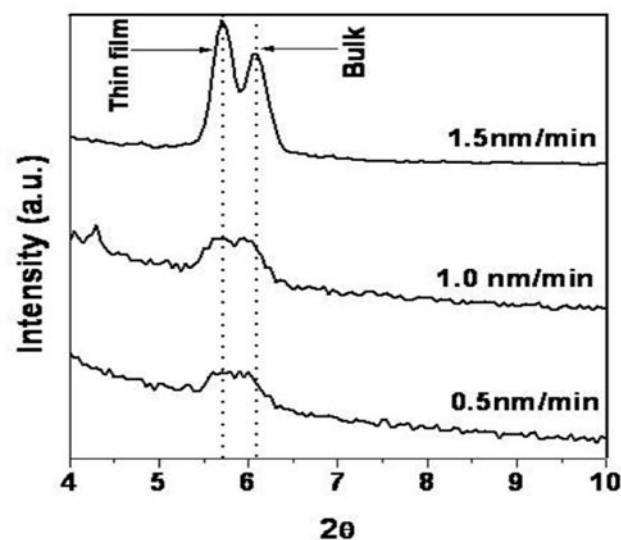
Fig. 3: XRD of pentacene films (50 nm) deposited at 0.5 nm/min, 1 nm/min and 1.5 nm/min deposition rate on untreated SiO$_2$ substrate. Substrate temperature is 70 ^{0}C in all cases. Dotted vertical lines show the position of thin film and bulk phase.
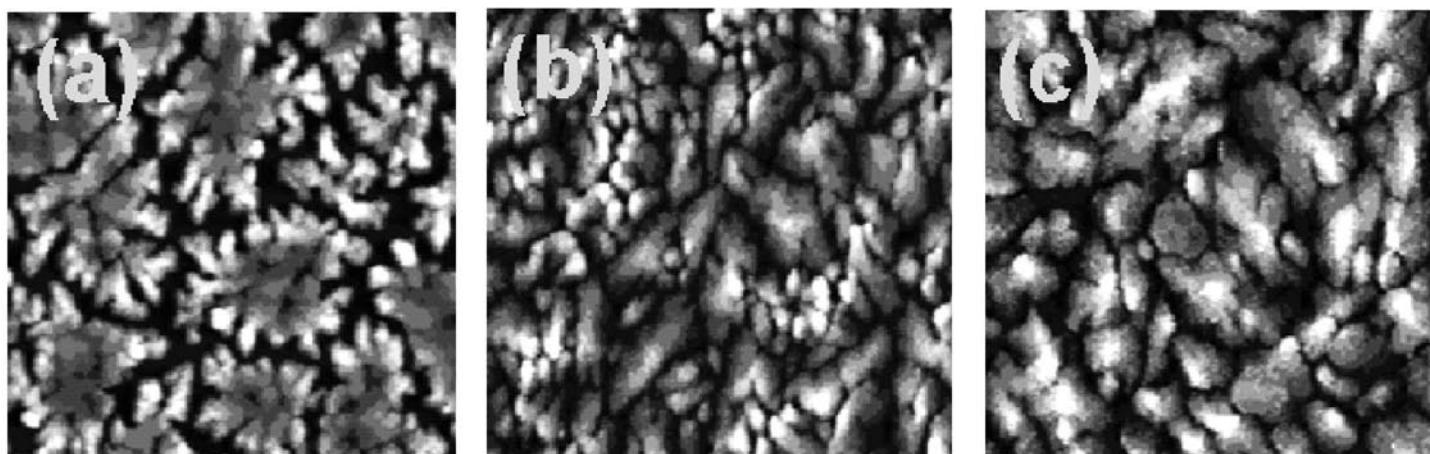
Fig. 4: AFM images (7μm × 7μm) of pentacene films (50 nm) deposited at (a) 0.5 nm/min, (b) 1 nm/min and (c) 1.5 nm/min deposition rate on untreated SiO$_2$ substrate. Substrate temperature is 70 ^{0}C in all cases.

If we compare with inorganic thin films, generally higher deposition rate leads to poor crystallinity, here we observe a reverse trend. This is because growth flux of inorganic films is usually atomic, whereas growth flux for organic film is consisting of organic molecules. Inorganic thin films have stronger ionic or covalent bonds, whereas organic films have weak van der Waals bonds. During inorganic film deposition, atoms are adsorbed on the substrate, and diffuse around in order to form nuclei and participate in film growth or eventually get desorbed from the substrate. Since higher substrate temperatures are required for the formation of inorganic crystal surface diffusion of atoms determines the crystallinity of the film. Therefore, low deposition rate provides more time for surface diffusion and better crystallinity.

In the case of organic thin films, deposited organic molecule is large in size and their diffusion may be restricted, but they easily crystallize at low temperatures. Therefore, at higher deposition rate, we will get high nucleation rate leading to better crystallinity and dense microstructure.

Thin film phase is a metastable phase whereas bulk phase is stable. Higher deposition rate basically promotes dominant metastable phase formation. The phase is determined by alignment of adsorbed pentacene molecule with respect to the surface normal (decided by the substrate reactivity) and relaxation of nuclei to a more stable structure. Higher deposition rate deters structure relaxation, as a result we have dominant thin film phase at higher deposition rate. At higher magnification AFM image gives a clear picture of growth of pentacene films. AFM image (Fig. 5) shows the faceted terrace like thin layers of pentacene. The grain size of the film was 2.05 µm. These grains have a layered structure with a uni-molecular step height of roughly 2 nm, which is consistent with XRD data that shows c axis is 1.55 nm [21].

Effect of substrate rate

When substrate temperature is reduced from 70 °C to 60 °C at the deposition rate of 1.5 nm/min, the mobility improves from 0.39 to 0.44 cm^2/Vs. Effect of change in substrate temperature from 70 °C to 60 °C on phase is
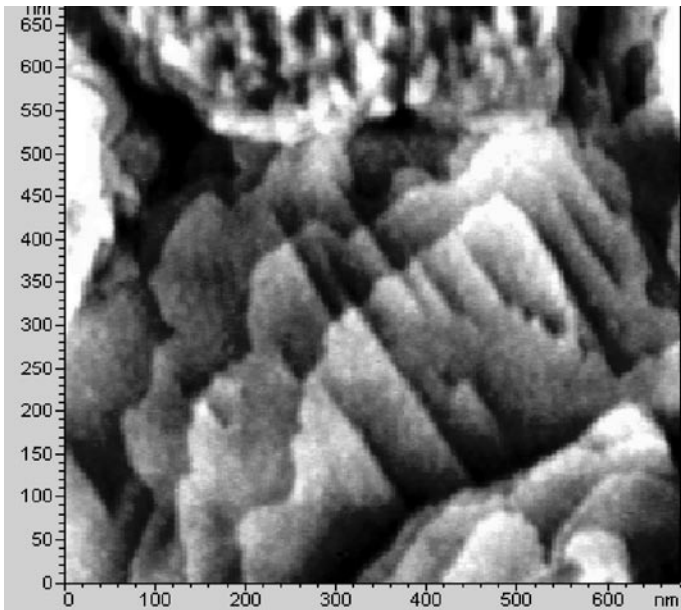
Fig. 5: AFM image (650 nm × 650 nm) of pentacene films (50 nm) deposited at 70 °C substrate temperature on untreated SiO$_2$ substrate with deposition rate is 1.5 nm/min.

shown in Fig. 6 and corresponding AFM micrograph is shown in Fig. 7. Higher substrate temperature in this range does help in stabilizing the bulk phase of pentacene. There is not significant change in microstructure (see Table 1), only a slight decrease in grain size at higher temperature.

Since we expect that nucleation density should increase at lower temperature, we can infer from here that in the temperature window used, there is no significant change in the microstructure due to temperature. Other researchers studying film growth in a larger temperature window do see decrease of grain size with temperature [8].

Effect of surface treatment and film thickness

Finally, transfer and output characteristics of untreated and OTS treated devices (T$_{sub}$ = 70 °C and deposition rate = 1.5 nm/min) of two different thickness (35 nm and 50 nm) were measured; results are summarized in Table 1. Surprisingly, no improvement of mobility was observed for OTS treated device as compared with the devices on untreated substrates. This is due to grain size effect. OTS reduces the grain size significantly, and higher grain boundary area becomes barrier for hole hopping. But, OTS improves other transistor characteristics (threshold voltage, I$_{on}$/I$_{off}$ and subthreshold swing) drastically, which is an indirect measurement of low defects/traps at pentacene/substrate interface.

Highest mobility observed with devices of thickness 35 nm, because of single phase (Fig. 8). XRD and AFM micrographs of untreated and OTS treated pentacene films are shown in Figs. 9 and 10, respectively. It is clear that the presence of bulk phase is not detrimental to the field effect
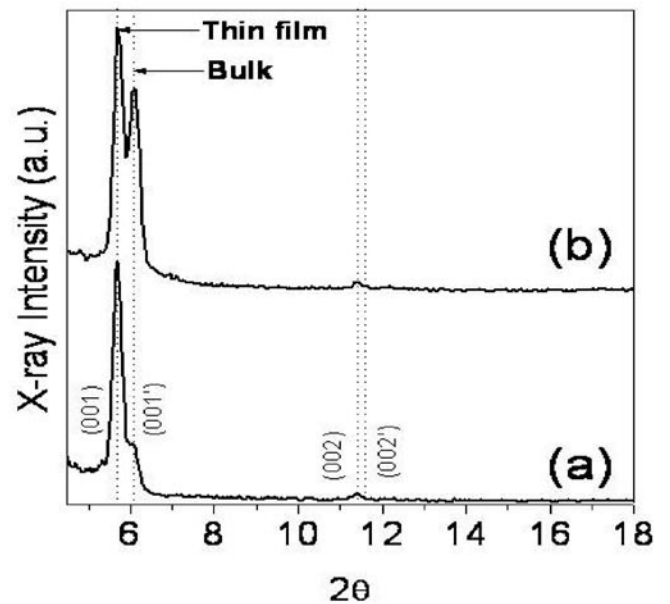
Fig. 6: XRD of pentacene films (50 nm) deposited at (a) 60 °C and (b) 70 °C substrate temperature on untreated SiO$_2$ substrate. Deposition rate is 1.5 nm/min. Dotted vertical line shows the position of thin film phase and bulk phase.
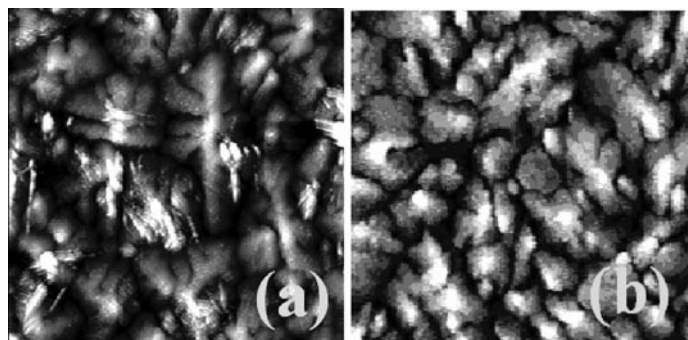
Fig. 7: AFM images (7 µm × 7 µm) of pentacene films (50 nm) deposited at (a) 60 °C and (b) 70 °C substrate temperature on untreated SiO$_2$ substrate. Deposition rate is 1.5 nm/min.

mobility. Mattheus et al. have also measured the mobility of bulk phase (14.1 Å polymorph) and found it to be 0.2 cm^2/Vs [15]. All our films show dendritic morphology, but for OTS treated substrate it becomes nodular. As pentacene-pentacene interaction and pentacenee-substrate interaction are comparable, pentacene deposition is very sensitive to change in the surface energy of the substrate. As we can see bulk phase is the preferred phase on OTS treated substrate. In general, inorganic thin films do not show such strong sensitivity to substrate as interaction energy between film- substrate is smaller compared to binding energy of inorganic crystals. Change in grain size is also a result of improved adsorption and higher surface coverage
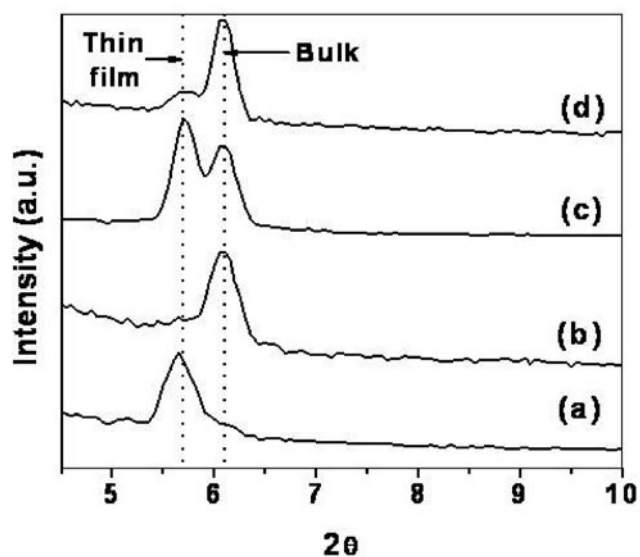
Fig. 8: XRD of pentacene films deposited at 70 °C substrate temperature on (a) and (c) untreated and (b) and (d) OTS treated SiO$_2$ substrate. Pentacene thickness is varied from 35 nm (a) and (b) to 50 nm (c) and (d). Deposition rate is 1.5 nm/min. Dotted vertical line shows the position of thin film phase and bulk phase.
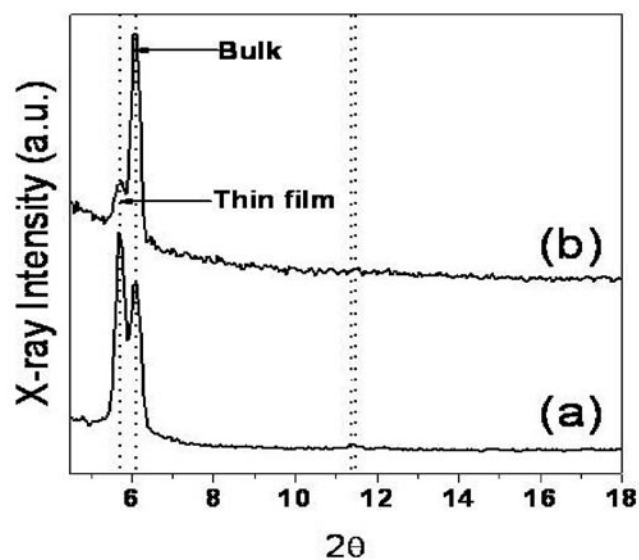
Fig. 9: XRD of pentacene films (50 nm) deposited at 1.5 nm/min and 70°C substrate temperature on (a) untreated and (b) OTS treated SiO$_2$ substrate. Dotted vertical lines show the position of thin film and bulk phase.
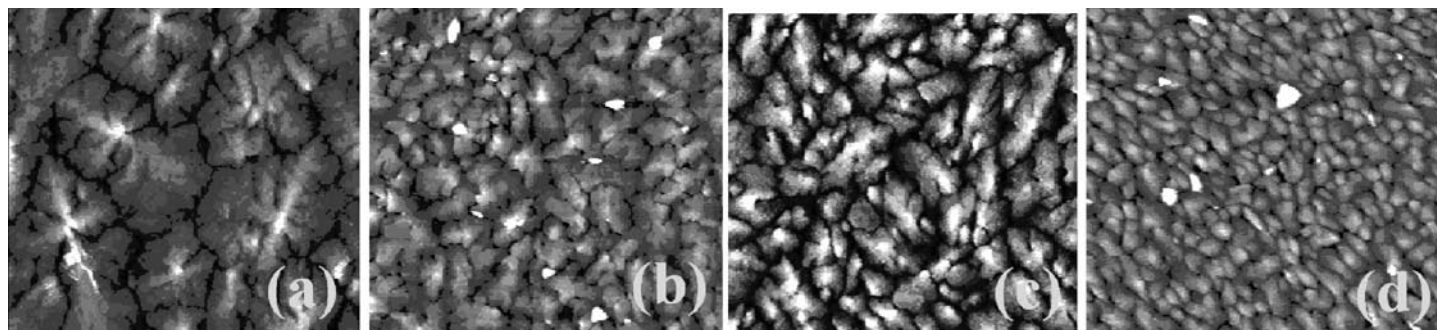
Fig. 10: AFM images (10 µm × 10 µm) of pentacene films deposited at 1.5 nm/min and 70 °C substrate temperature on (a) and (c) untreated and (b) and (d) OTS treated SiO$_2$ substrate. Pentacene thickness is varied from 35 nm (a) and (b) to 50 nm (c) and (d)

Table 1: **Summary of device results and film structure of untreated and OTS treated devices (T_{sub} = 70 °C and deposition rate = 1.5 nm/min) of two different thickness (35 nm and 50 nm)**

| Surface treatment, T_{sub}	Thickness (nm)	Mobility (μ) (cm²/Vs)	Phase	Grain size (μm)
Without OTS, 60°C	50	0.44	Thin film & bulk	2.20
Without OTS, 70°C	50	0.39	Thin film & bulk	2.05
OTS, 70°C	50	0.14	Thin film & bulk	0.78
Without OTS, 70°C	35	0.67	Thin film	4.22
OTS, 70°C	35	0.59	Bulk	1.20

of pentacene molecules on treated substrates – leading to high nucleation rate and smaller grains. Microstructure of organic thin films as a function of thickness is also different from most inorganic thin films which show increased grain size with thickness due to diffusion mediated growth of grains. Here, decrease in grain size with thickness points to easy secondary nucleation which is possible in organic films. This also leads to dominance of bulk phase at higher thickness as secondary nucleation occurs on previous pentacene layer, not on the substrate.

Conclusions

Considering the processing window where device quality pentacene is being deposited on SiO_2, deposition rate is an important parameter for penatcene thin films; higher deposition rate helps to form metastable thin film phase and dense microstructure. Lowing of substrate temperature also stabilizes metastable phase. Thickness has an important effect on phase and grain size as secondary nucleation of pentacene occurs easily. OTS treatment stabilizes the growth of bulk phase and increases nucleation density of pentacene, so lesser grain size is obtained.

Generally, for inorganic thin film crystal structure and microstructure is governed by substrate temperature or surface diffusion assisted growth, other parameters governing nucleation rate being secondary in the region of interest. For organic thin films of small molecules, microstructure and crystallinity is determined by the nucleation density, this is a consequence of weak van der Waals forces responsible for crystallization. Finally, interaction with the substrate is very important in determining the crystal phase of organic films.

References

1. J.M. Shaw and P.F. Seldler, *IBM J. Res. & Dev.* 45 **(2001)** 3.
2. R.G. Endres, C.Y. Fong, L.H. Yang, G. Witte and Ch. Wöll, *Computational Materials Science* 29 **(2004)** 362.
3. Mitsumasa Iwamoto, Takaaki Manaka, Eunju Lim and Ryousuke Tamura, *Current Applied Physics* 7 **(2007)** 334.
4. F. J. Meyer Zu Heringdrof, M. C. Reuter and R. M. Tromp, *Appl. Phys. A* 78 **(2004)** 787.
5. B. Stadlober, U. Haas, H. Maresch and A. Haase, *Physical Review B* 74 **(2006)** 165302.
6. C. D. Dimitrakopoulos, A. R. Brown and A. Pomp, *J. Appl. Phys.* 80 **(1996)** 2501.
7. H. Yanagisawa, T. Tamaki, M. Nakamura and K. Kudo, *Thin solid films* 464-465 **(2004)** 398.
8. J. Lee, J. H. Kim and S. Im, *J. Appl. Phys.* 95 **(2004)** 3733.
9. R. Ruiz, D. Choudhary, B. Nickel, T. Toccoli, K. C. Chang, A. C. Mayer, P. Clancy, J. M. Blakely, R. L. Headrick, S. Iannotta and G. G. Malliaras, *Chem. Mater.* 16 **(2004)** 4497.
10. S. Steudel, S. De Vusser, S. De Jonge, D. Janssen, S. Verlaak, J. Genoe and P. Heremans, *Appl. Phys. Lett.* 85 **(2004)** 4400
11. J. H. Park, C. H. Kang, Y. J. Kim, Y. S. Lee and J. S. Choi, *Mat. Sc. and Eng. C* 24 **(2004)** 27.
12. A. Salleo, M. L. Chabinyc, M. S. Yang and R. A. Street, *Appl. Phys. Lett.* 81 **(2002)** 4383.
13. K. S. Pyo and C. K. Song, *Thin Solid Films* 485 **(2005)** 230.
14. T. Kakudate, N. Yoshimoto and Y. Saito, *Appl. Phys. Lett.* 90 **(2007)** 081903.
15. C. C. Mattheus, A. B. Dros, J. Baas, G. T. Oostergetel, A. Meetsma, J. L. De Boer and T. T. M. Palstra, *Synth. Met.* 138 **(2003)** 475.
16. U. Haas, A. Haase, H. Maresch, B. Stadlober and G. Leising, *Polymers and Adhesives in Microelectronics and Photonics, 2004, Polytronic 2004*, 4th IEEE International Conference, 12-15 Sept, **(2004)** 219-224.
17. R. A. Street, D. Knipp and A. R. Volkel, *Appl. Phys. Lett.* 80 **(2002)** 1658.

18. S. Verlaak, V. Arkhipov and P. Heremans, *Appl. Phys. Lett.* 82 **(2003)** 745.

19. D. Guo, S. Ikeda, K. Saiki, H. Miyazoe and K. Terashima, *J. Appl. Phys.* 99 **(2006)** 094502.

20. C. Mayer, R. Ruiz, R. L. Headrick, A. Kazimirov and G. G. Malliaras, *Organic Electronics,* 5 **(2004)** 257.

21. P. M. Bouchoms, W.A. Schoonveld, J. Vrijmoeth and T. M. Klapwijk, *Synth. Met.* 104 **(1999)** 175 .

Highly Fluorescent Molecular Crystals, Nanocrystals and Aggregates Based on Diaminodicyanoquinodimethanes

T. P. Radhakrishnan

School of Chemistry, University of Hyderabad, Hyderabad - 500 046, India
E-mail: tprsc@uohyd.ernet.in

Abstract

Molecular materials in the form of crystals, nanocrystals and thin films, exhibiting strong photoluminescence and electroluminescence are of great contemporary interest for various technological and device applications, especially in view of the deleterious effect of self-quenching of light emission observed with most dye molecules. In this article we provide a brief overview of a family of highly zwitterionic diaminodicyanoquinodimethane based molecules that we have developed in our laboratory, and the corresponding materials in the form of crystals, nano/microcrystals and aggregates in colloidal state exhibiting strong fluorescence emission. Examples of systems studied, the novel and fundamentally important phenomena observed and the models developed to explain the observations are discussed.

Keywords: molecular materials, nano crystals, thin films, Diaminodicyanoquinodimethanes, photo-luminescence.

Introduction

Materials exhibiting efficient photoluminescence and electroluminescence are of great interest in the field of display devices as well as several photonic and optoelectronic applications. Molecular materials with their inherent synthetic flexibility and ease of fabrication are promising candidates. Unfortunately, majority of the molecules which show strong fluorescence in their isolated state in solution, are prone to aggregation-induced quenching of the light emission, the excitation energy being lost non-radiatively through effects such as intermolecular transfers. A large number of investigations in recent times have therefore addressed the issue of developing new molecules that exhibit strong and enhanced light emission in their aggregated and crystalline states; examples include sterically crowded siloles [1], cyanobis(biphenyl)ethenes [2], diphenylbutadienes [3] and tetraphenylethenes [4]. Enhanced emission in the solid state in these materials have been attributed to a variety of effects like restricted intramolecular motion [1,4] and ground state conformational change [2]. Some derivatives of 7,7-diamino-8,8-dicyanoquinodimethane (DADQ) were found to show weak fluorescence in the solution state, but enhanced fluorescence in highly viscous media and the solid state [5].

We have developed a family of molecules based on the DADQ framework (Fig. 1), bearing saturated ring substituents with remote functional groups [6]. Systematic investigation of the enhanced green fluorescence in the solid state of these compounds was carried out using detailed crystallographic characterizations and computational modeling.
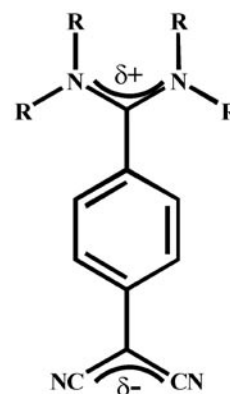
Fig. 1: The structure of DADQs. The zwitterionic form of the molecular structure inferred from crystallographic investigations is indicated.

The enhanced fluorescence was explained in terms of the suppression of excited state geometry relaxation. Polymer thin films doped with these compounds exhibit solvent vapor induced fluorescence switching. Subsequently, we have investigated aromatic derivatives of the DADQ system which also showed strong green fluorescence

response in the solid state [7]. The electronic structure of these molecules is very sensitive to the intramolecular twist between the diaminomethylene moiety and the benzenoid ring [8]. This feature was exploited to develop red fluorescent derivatives of DADQ [9]. Interestingly, these molecules were amenable to facile formation of very stable colloids [9,10] through the reprecipitation technique [11]. Luminescent molecular nanomaterials are useful in applications such as organic light emitting diodes, biological probes and sensors [12]. Using a novel digestion protocol, we were able to generate nano/microcrystals of the DADQ derivatives and investigate fundamental size-dependent optical absorption and emission [9] as well as nonlinear optical responses [13] in these molecular nanomaterials. As the remote-functionalized derivatives of DADQs are soluble in most common solvents, the reprecipitation strategy is ineffective for the preparation of their colloids. Recently we have developed a polyelectrolyte-assisted reprecipitation method to prepare their colloids which exhibit very large enhancement of the fluorescence over the solution state [14]. In the following sections we provide a brief overview of our investigations of enhanced fluorescence in three classes of materials based on the DADQ framework: (i) molecular crystals of remote-functionalized DADQs, (ii) molecular crystals and nano/microcrystals of haloanilino derivatives of DADQ and (iii) polyelectrolyte-complexed colloids of a remote-functionalized DADQ molecule.

Molecular crystals of remote-functionalized DADQs

Typical examples of this class of molecules that we have developed are shown in Fig. 2. A variety of pyrrolidino, piperazino and piperidino derivatives were synthesized by the direct reaction of the corresponding amines with 7,7,8,8-tetracyanoquinodimethane [15,16], without or with the addition of bases. The functional groups on these saturated rings are not in π-conjugation with the DADQ framework, hence do not influence directly the electronic structure and optical properties of the push-pull zwitterionic chromophore system.

Fig. 3 is a typical demonstration of the enhanced fluorescence displayed in the solid state by these compounds; the figure shows the absorption spectra (with nearly matched optical density) and fluorescence emission spectra of molecule **1** (Fig. 2) in acetonitrile solution and in the solid state [6]. The solution shows very weak fluorescence; the solid state fluorescence is found to be ~ 200 times stronger. The situation is similar for the various
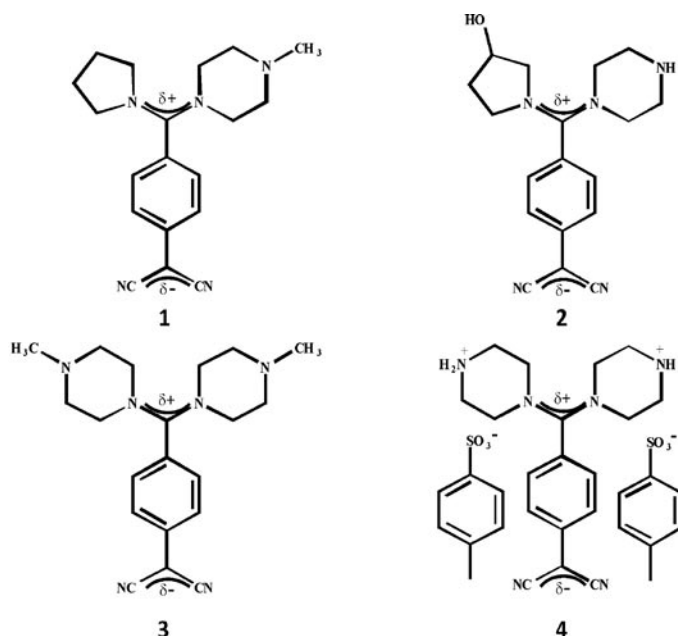
Fig. 2: Structure of some of the remote-functionalized DADQs we have studied.

remote-functionalized DADQ derivatives. In this study we also showed that these compounds doped in polymer films exhibit strong fluorescence response. The remote functionalities on the molecules improve their solubility in common solvents enabling convenient fabrication of doped polymer films. Interestingly, exposure of the polymer film embedded with these compounds to organic solvent vapors lead to strong quenching of the fluorescence. The fluorescence can be retrieved upon drying the film and the fluorescence switching repeated several times. The mechanism involved in the fluorescence enhancement in the solid state of these compounds is represented schematically in Fig. 4. The barrier to rotation about the bond connecting the diaminomethane moiety with the benzenoid ring is quite low in view of the nearly single bond-like character. The dihedral angle about this bond is typically in the range 30 – 50° in the solid state structure of most of these molecules, and is very sensitive to the dielectric constant of the environment [17]. Computational studies we have carried out [6] show that the dihedral twist increases to nearly 90° in the excited state of these molecules. The associated change in the electronic states suggests that no fluorescence emission is likely to occur in the visible range. In the solid state, this intramolecular twist in the excited state is hampered due to the packing constraints.
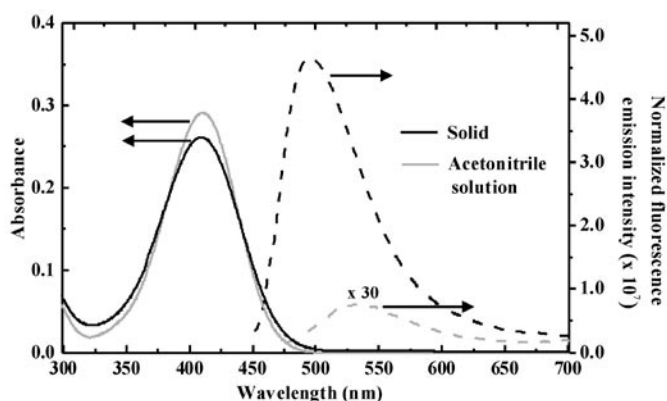
Fig. 3: Electronic absorption and normalized fluorescence emission spectra of molecule 1 (Fig. 2) in the solid state and acetonitrile solutions; note that the fluorescence spectrum in solution has been magnified by a factor of 30 [Ref. 6].
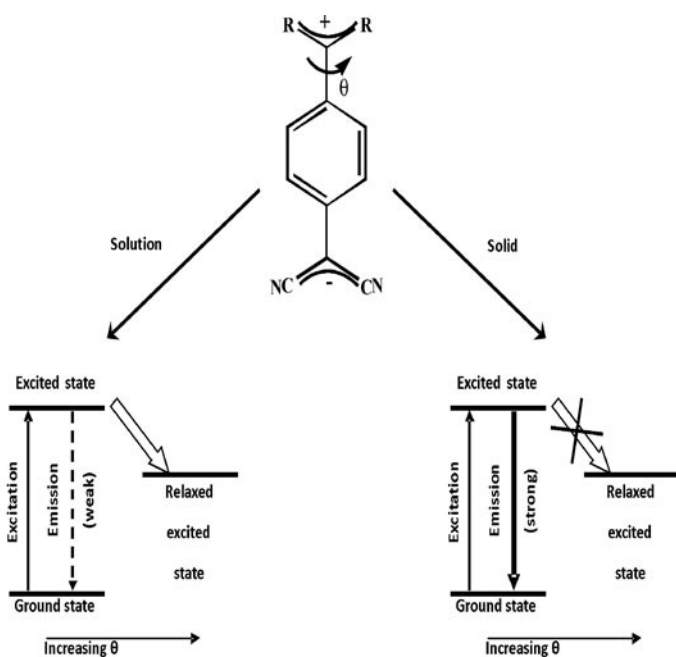
Fig. 4: Schematic representation of the mechanism of formation of strong emission in the solid state of DADQs. θ represents the intramolecular twist about the bond connecting the diaminomethylene unit with the benzenoid ring [Refs. 6, 14].

This restricted geometry relaxation would lead to efficient fluorescence emission.

Nano/microcrystals of haloanilino derivatives of DADQs

Some of the haloanilino DADQs that we have synthesized and studied are shown in Fig. 5. The general procedure we have used earlier [15, 16] was used in the synthesis as well. When 2-methyl-4-chloroaniline was used as the amine, a complex reaction occurred, with three major products being formed. Besides two monosubstituted products which exhibit pH-dependent optical responses, the bis-substitute product, **5** (Fig. 5) was also obtained, which showed the normal enhanced green fluorescence in the solid state [7]. More interestingly, simple 4-haloanilines gave products such as **6** and **7** (Fig. 5) which showed strong red fluorescence [9]. The relatively lower dihedral twist in these molecules and the more effective extended π-conjugation lead to this wavelength shift. We have carried out an extensive investigation of nano/micro crystals of **6** prepared through the reprecipitation route followed by controlled digestion at different temperatures (Fig. 6). Significant size-effects were observed in the optical absorption and emission of these molecular nanomaterials (Fig.7). These fundamentally important observations were explained using detailed crystallographic, spectroscopic and computational studies, as arising due to the increasing rigidity of the crystals as they grow from nanometer to micrometer sizes and the impact of this on the intermolecular interactions and electronic structure. Bulk material characteristics were observed when the crystal sizes reached about 1 – 2 μm. The nano/microcrystals of **6** were also found to show appreciable size-dependence in their optical limiting capabilities [13]. This study explored the contributions from nonlinear absorption and scattering to the optical limiting behavior. We have also examined the evolution of the optical responses as the molecules **7** in solution assembled into nano/microcrystals [10]. The study was conducted by incorporating increasing amount of a nonsolvent into the solution of the compound. The electronic absorption as well as fluorescence were found
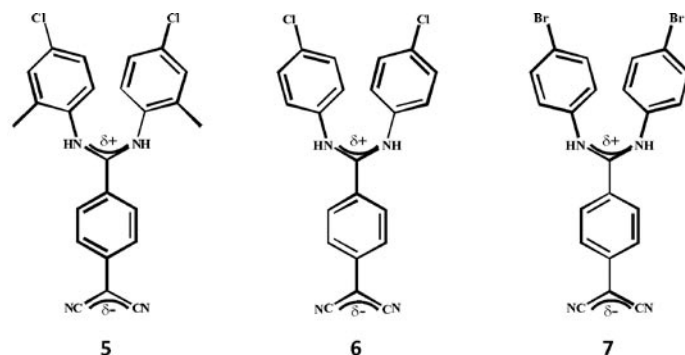
Fig. 5: Structure of some of the haloanilino derivatives of DADQs we have studied.
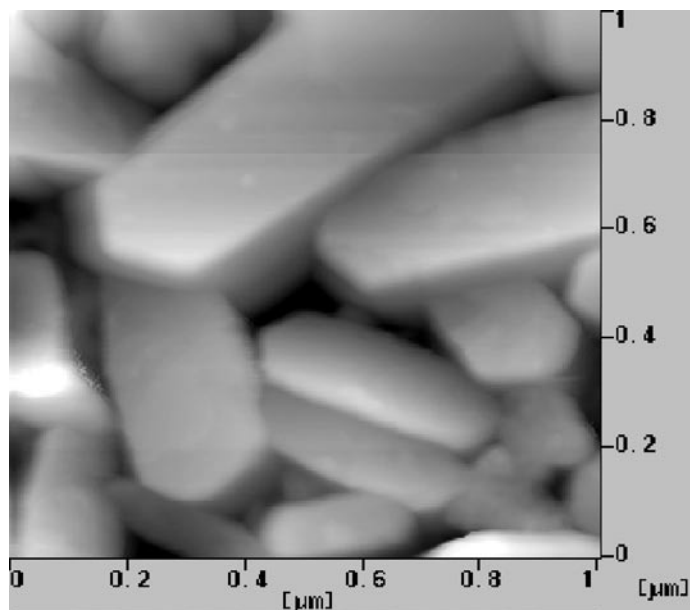
Fig. 6: Nanocrystals of 6 prepared through the reprecipitation-digestion protocol; thickness of the crystals is typically 50 – 100 nm [Ref. 9].
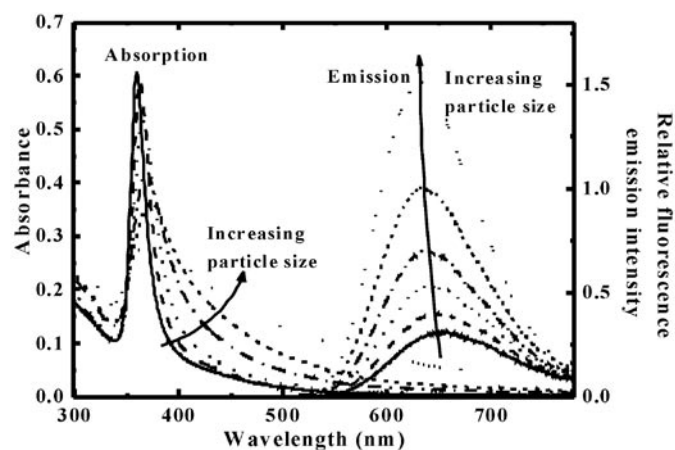
Fig.7: Dependence of the electronic absorption and emission spectra of 6 on the size of the nano/microcrystals formed through the reprecipitation-digestion protocol [Refs. 9, 18].

Polyelectrolyte-assisted reprecipitation of a remote-functionalized DADQ molecule

As the remote-functionalized DADQ molecules are highly soluble in most of the common organic solvents and water, the traditional reprecipitation technique is not

useful for the formation of their colloids and nanocrystals. Therefore we have developed a novel approach to tackle this problem. Molecule **4** (Fig. 2) was chosen for this study, as it has a salt structure. The idea was to exploit the possible complexation of the cationic DADQ system with the polyanion moiety of a polyelectrolyte such as poly(sodium 4-styrenesulfonate) (NaPSS) and then attempt the reprecipitation utilizing the insolubility of the polyelectrolyte component. Interestingly it was found that the complexation of **4** with NaPSS in aqueous solution itself led to appreciable enhancement of the fluorescence response, possibly due to the restriction on the geometry relaxation of **4** in the excited state induced by the polyelectrolyte environment. When this aqueous solution was injected into methanol in optimal proportions, stable colloid formation and a further enhancement of fluorescence were observed, the overall enhancement from solution to colloid being of the order of ~ 90 (Fig. 8) [14]. Microscopy studies established the formation of nano/microcrystals in the colloid. A model that explains the observed phenomena
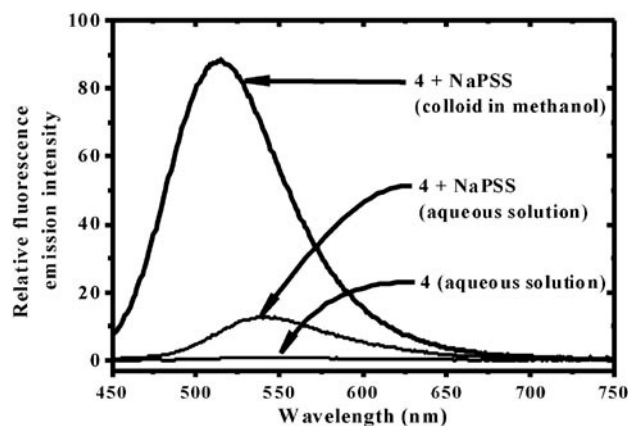
Fig. 8: Fluorescence emission enhancement observed for 4 complexed with NaPSS in aqueous solution and formed into colloids by reprecipitation of the complex in methanol [Ref. 14].

was constructed through detailed spectroscopic studies coupled with some isothermal titration calorimetry and a range of control experiments.

Conclusions

We have presented a brief overview of strongly fluorescent materials developed in our laboratory, based on the DADQ framework. The materials include crystals, nano/microcrystals and aggregates with polyelectrolytes. These compounds form a versatile class

of easily synthesized molecules amenable to variation in terms of the electronic structure and optical responses. Detailed crystallographic, spectroscopic, microscopic and computational investigations have provided a basic understanding of the correlation between the observed optical phenomena on the one hand and the molecular and lattice structure on the other, in the various forms of these novel molecular materials. They form an interesting class of compounds with potential device applications. Current explorations are focused on developing thin and ultrathin films based on this class of molecules.

References

1. a) J. Luo, Z. Xie, J. W. Y. Lam, L. Cheng, H. Chen, C. Qiu, H. S. Kwok, X. Zhan, Y. Liu, D. Zhu and B. Z. Tang, *Chem. Commun.*, (**2001**) 1740. b) Y. Hong, J. W. Y. Lam and B. Z. Tang, *Chem. Commun.*, (**2009**) 4332.

2. a) B. K. An, S. K. Kwon, S. D. Jung and S. Y. Park, *J. Am. Chem. Soc.*, 124 (**2002**) 14410. b) T. Hirose and K. Matsuda, *Chem. Commun.*, (**2009**) 5832.

3. R. Davis, N. S. S. Kumar, S. Abraham, C. H. Suresh, N. P. Rath, N. Tamaoki and S. Das, *J. Phys. Chem. C*, 112 (**2008**) 2137.

4. a) Y. Dong, J. W. Y. Lam, A. Qin, J. Sun, J. Liu, Z. Li, S. Zhang, J. Sun, H. S. Kwok and B. Z. Tang, *Appl. Phys. Lett.*, 91 (**2007**) 011111. b) Z. Zhao, S. Chen, X. Shen, F. Mahtab, Y. Yu, P. Lu, J. W. Y. Lam, H. S. Kwok and B. Z. Tang, *Chem. Commun.*, 46 (**2010**) 686.

5. D. Bloor, Y. Kagawa, M. Szablewski, M. Ravi, S. J. Clark, G. H. Cross, L. Pålsson, A. Beeby, C. Parmer and G. Rumbles, *J. Mater. Chem.*, 111 (**2001**) 3053.

6. S. Jayanty and T. P. Radhakrishnan, *Chem. Eur. J.*, 10 (**2004**) 791.

7. A. Patra and T. P. Radhakrishnan, *Chem. Eur. J.*, 15 (**2009**) 2792.

8. a) M. Ravi and T. P. Radhakrishnan, *J. Phy. Chem.*, 99 (**1995**) 17624. b) J. M. Cole, R. C. B. Copley, G. J. McIntyre, J. A. K. Howard, M. Szablewski and G. H. Cross, *Phys. Rev. B*, 65 (**2002**) 125107.

9. [9] A. Patra, N. Hebalkar, B. Sreedhar, M. Sarkar, A. Samanta and T. P. Radhakrishnan, *Small*, 2 (**2006**) 650.

10. A. Patra, N. Hebalkar, B. Sreedhar and T. P. Radhakrishnan, *J. Phys. Chem. C*, 111 (**2007**) 16184.

11. H. Nakanishi and H. Oikawa, In *Single Organic Nanoparticles*; Eds. H. Masuhara, H. Nakanishi and K. Sasaki, Springer: Berlin, 2003; pp 17-31.

12. a) E. I. Mal'tsev, D. A. Lypenko, B. I. Shapiro, M. A. Brusentseva, V. I. Berendyaev, B. V. Kotov and A. V. Vannikov, *Appl. Phys. Lett.*, 73 (**1998**) 3641. b) L. Jinshui, W. Lun, G. Feng, L. Yongxing and W. Yun, *Anal. Bioanal. Chem.*, 377 (**2003**) 346. c) E. Botzung-Appert, V. Monnier, T. Ha Duong, R. Pansu and A. Ibanez, *Chem. Mater.*, 16 (**2004**) 1609. d) L. Wang, L. Wang, L. Dong, G. Bian, T. Xia and H. Chen, *Spectrochim. Acta A*, 61 (**2005**) 129.

13. A. Patra, N. Venkatram, D. Narayana Rao and T. P. Radhakrishnan, *J. Phys. Chem. C*, 113 (**2008**) 16269.

14. C. G. Chandaluri, A. Patra and T. P. Radhakrishnan, *Chem. Eur. J.* (in press).

15. [15] L. R. Hertler, H. D. Hartzler, D. S.Acker and R. E. Benson, *J. Am. Chem. Soc.*, 84 (**1962**), 3387.

16. a) M. Ravi, D.N. Rao, S. Cohen, I. Agranat and T. P. Radhakrishnan, *Chem. Mater.*, 9 (**1997**), 830. b) M. Ravi, P. Gangopadhyay, D. N. Rao, S. Cohen, I. Agranat and T. P. Radhakrishnan, *Chem. Mater.*, 10 (**1998**) 2371. c) P. Gangopadhyay, S. Sharma, A. J. Rao, D. N. Rao, S. Cohen, I. Agranat and T. P. Radhakrishnan, *Chem. Mater.*, 11 (**1999**) 466. e) S. Jayanty, P. Gangopadhyay and T. P. Radhakrishnan, *J. Mater. Chem.*, 12 (**2002**) 2792.

17. S. Jayanty and T. P. Radhakrishnan, *Chem. Mater.*, 13 (**2001**) 2460.

18. K. Rajesh, A. Patra and T. P. Radhakrishnan, *Bull. Mater. Sci.*, 31 (**2008**) 421.

Polyol method for synthesizing a variety of materials in nanosize dimensions

B. S. Naidu, R. S. Ningthoujam, V. Sudarsan* and R. K. Vatsa

Chemistry Division, Bhabha Atomic Research Centre, Mumbai 400085
*Corresponding author; E-mail: vsudar@barc.gov.in

Abstract

Polyol method can be used to prepare a variety of materials/compounds including metals, oxides, phosphates, sulfides, fluorides etc having size in the range of few nanometers to micrometers. Essentially the preparation method involves the reaction of a polyol soluble salt of the metal ions and a precipitating agent. Some of the nanoparticles prepared by polyol methods have been characterized by XRD, TEM and photoluminescence techniques. The method offers simple and economic method without using any hazardous or moisture sensitive reagents for preparing a variety of nanomaterials.
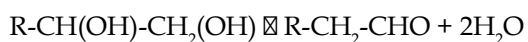
Keywords: Nanomaterials, nanoribbons, oxides, phosphates, polyol method, photoluminescence

Introduction

Polyol represents the molecule having two or more alcohol groups (O-H). It is generally known as polyalcohols. This molecule can form intra or inter molecular hydrogen bonding and the viscosities are higher than that of water [1-3]. This result in higher boiling temperatures and many reactions can be performed below its boiling point. A few examples of polyol molecules are ethylene glycol (EG), tetra-ethylene glycol (TEG), polyethylene glycol (PEG), glycerol, decanediol, etc. Lower molecular weight compounds of PEG (PEG-100-600) are liquids, whereas, higher molecular weight compounds of PEG (PEG-1000-6000) are solids. All polyols can be dissolved in polar medium and even in some organic solvents. PEG is a polymerization product of ethylene oxide and water with the general formula $H(OCH_2CH_2)_nOH$. Viscosity of PEG varies with molecular weight. For example PEG with molecular weight variation from 100 to 600 g, the viscosity increases from 50 to 135 cP.

Polyols are used in many applications like coolants/heat-transfer agents, precursor for polymer based plastic bottles, desiccants, as a preservative for specimens in laboratories etc [1-3]. In addition to this, it can be used for the synthesis of a variety of inorganic compounds/materials such as metals, alloys, composites, oxides, phosphates, sulphides and fluorides with small/nanosize dimension [4-20].

For the synthesis of metallic particles, the polyol method is used to reduce metal ions into metal particles because of its mild reducing properties. The possible chemical reaction is given below [11]

$$R\text{-}CH(OH)\text{-}CH_2(OH) \rightarrow R\text{-}CH_2\text{-}CHO + 2H_2O$$

$$R\text{-}CH_2\text{-}CHO + M^{n+} \rightarrow R\text{-}CH_2COCOCH_2\text{-}R + M + H^+$$

It is not necessary that all the polyol molecules should undergo oxidation to aldehyde molecules.

A variety of metals, alloys, and composites namely Ru, Rh, Sn, Re, W, Pt, Au, Fe-Cu, Co-Cu, Ni-Cu, Fe, Co, Ni, Cu, Pd-Ag, Fe-Pt, Fe-Pd, etc [9-15] are prepared by polyol method. Also, the polyol acts as solvent with a chelating effect which reduces the extent of agglomeration of smaller particles during the preparation [4-8]. It gives a homogeneous phase composition, narrow particle size distribution and high specific surface area. Overall, the synthesis procedure is simple, economic and is easily adaptable. There are also a number of reports on the preparation nanomaterials of oxides, phosphates, sulphides, fluorides etc based on polyol method. They include compounds such as Ln_2O_3, $LnVO_4$, $LnPO_4$ (Ln = Rare-earth ions), Fe_3O_4, Bi_2O_3, SnO_2, TiO_2, SiO_2 ZnO, ZnS, LnF_3, and CdSe, etc [4-8, 16-18]. In this article, few examples of synthesis of nanomaterials using polyol method are described. Some of the nanoparticles prepared by polyol method have been characterised by Transmission Electron Microscopy and Photoluminescence techniques.

Experimental

Synthesis of small metal particles

Around 10 ml of an aqueous solution of metal ions (0.1 M) is treated with 100 ml of polyols like EG or PEG. The solution is transferred to a round bottom (RB) flask and heated over the range of 120-195 °C for 2-24 h under Ar/N_2 flow. Schematic diagram for the procedure is shown in Fig. 1. Usually, Ag, Au and Pd metal particles can be obtained by reduction at lower temperature of 120 °C with a short duration of heat-treatment (2-3 h) [9-14.]. However, Ni, Fe, Co particles can be prepared at a higher temperature of 190 °C with a longer duration of heat treatment [21-23].

Particle sizes are usually found to be in sub-micron range. In order to reduce particle size to nano range, capping agents such as oleic acid, sodium dodecyl sulphate (SDS) and cetyl trimethyl ammonium bromide (CTAB) etc are used [24,25]. Sometimes, NaOH is used to reduce particle size [26]. Also, particle size obtained is dependent on the precursor used like $NiCl_2$, Ni-Acetate, $Ni(NH_3)_6Cl_2$ and NiOH [22].

Synthesis of oxide nanoparticles

Around 10 ml of an aqueous solution of metal ions (0.1 M) is treated with 100 ml of polyols such as EG or PEG [4-8, 16-18]. The solution is transferred to the round bottom (RB) flask and heated close to 100 °C. At this stage, precipitating agents such as urea, NH_4OH and NaOH are added and the temperature is raised to above 120-180 °C, depending on the actual material involved in synthesis and maintained at his value for two hours. After two hours, the reaction temperature is slowly reduced to room temperature and the precipitate is centrifuged, washed and dried under ambient conditions.

Synthesis of phosphate nanoparticles

In this paper we describe the synthesis of $SbPO_4$ doped with Tb^{3+} ions as representative luminescent phosphate nanomaterials. For preparation of $SbPO_4$ and lanthanide ions (Tb^{3+}) doped $SbPO_4$ nano-materials, $SbCl_3$ and Tb_4O_7 are used as starting materials. In a typical procedure for making $SbPO_4$:Tb^{3+} sample, 0.5 g of $SbCl_3$ and 0.01g of Tb_4O_7 (5 at. %) are dissolved in concentrated HCl in a beaker and the excess acid is evaporated out repeatedly. To this solution, ethylene glycol (12 ml) and glycerol (8 ml) are added and it is transferred into a two-necked 100 ml RB flask. The solution was slowly heated upto 70 °C followed by addition of 0.3 g of ammonium dihydrogen phosphate. Temperature is then raised initially to 90 °C. A slightly turbid solution is obtained. Temperature is again raised 120 °C and maintained at this value for 2 h. After the reaction, the precipitate is collected by centrifugation and then washed two times with acetone and three times with ethyl alcohol followed by drying under ambient conditions. The reaction medium after removing the precipitate is analyzed by fluorimetry to check whether any (Tb^{3+}) ions are remaining unreacted. No Tb^{3+} emission is detected revealing that all the lanthanide ions got incorporated in the $SbPO_4$ host. Samples obtained by above method are found to be dispersible in water and methanol.

Synthesis of sulfide nanoparticles

Around 10 ml of an aqueous solution of metal ions (0.1 M) is treated with 100 ml of polyols such as EG or PEG. The solution is transferred to the round bottom (RB) flask. The precipitating agents such as thiourea, Na_2S are used and slight excess of precipitating agent with respect to metal ions (in terms of molar) is added to the RB flask. Ar/N_2 gas flow is provided and the temperature is raised over the range of 120-185 °C for 2-24 h resulting in the precipitation of the nanoparticles [15,19,20]. After the reaction, the precipitate is collected by centrifugation and then washed two times with acetone and three times with ethyl alcohol followed by drying under ambient conditions. Using this, nano to sub-micron size particles can be prepared.
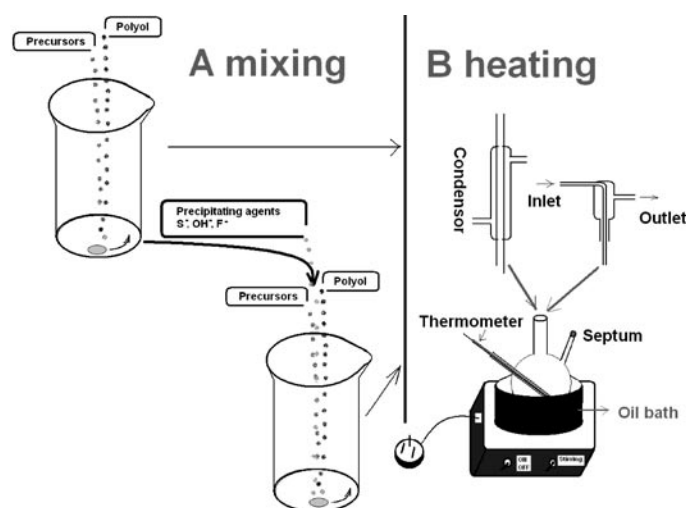
Fig. 1: Schematic diagram for the preparation of nanomaterials by polyol route.

Synthesis of fluoride nanoparticles

Procedure is same as the preparation of sulphide. Here, the precipitating agent is LiF, NaF [19].

Characterization

X-ray diffraction (XRD) studies are carried out using a Philips powder X-ray diffractometer (model PW 1071) with Ni filtered Cu-Kα radiation. The lattice parameters are calculated from the least square fitting of the diffraction peaks. Average crystallite size is calculated from diffraction line width based on Scherrer relation $D = 0.9\lambda/\beta Cos\theta$, where D is the average particles size, λ is the wavelength of X-rays and β is full width at half maximum (FWHM).
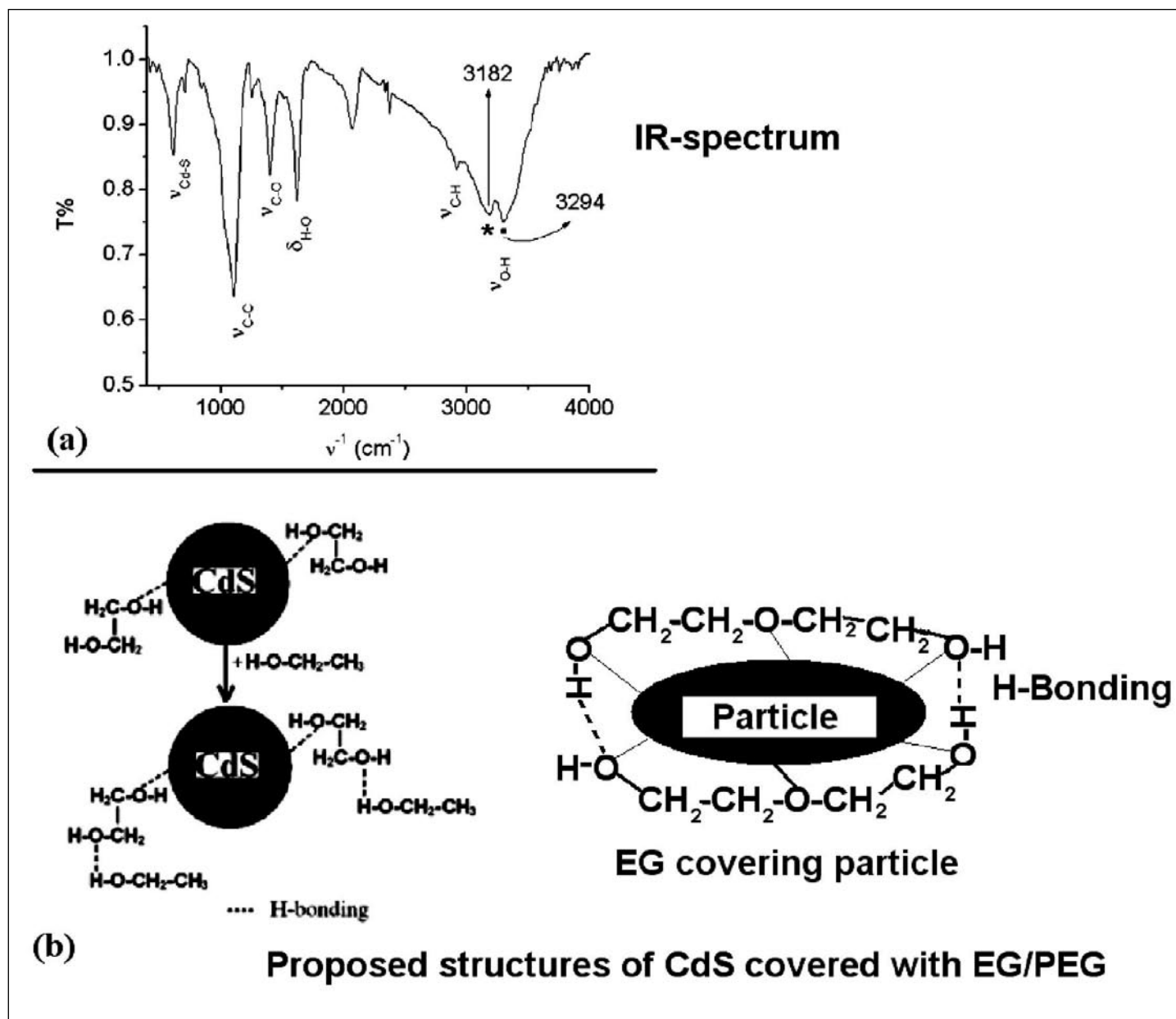
Fig.2: IR spectrum of (a) CdS nanoparticles prepared by EG and (b) schematic representation of the surface modification on the nanoparticles made by the ligand molecules.

All luminescence measurements are carried out at room temperature with a resolution of 3 nm, using a Hitachi Instrument (F-4500) having 150 W Xe lamp as the excitation source. Transmission electron microscopic (TEM) measurements (bright field low magnification and lattice imaging) are performed using 200 keV electrons in JEOL 2010 UHR TEM microscope. IR patterns are recorded for thin pellets of the samples made with KBr using a Bomem MB102 machine.

Results and discussion

In all the nanoparticles prepared by polyol method, the polyol molecules act as a stabilizing ligand on the surface of the nanoparticles and prevent the aggregation of nanoparticles. A schematic representation showing how the ligand gets stabilized on the surface of the CdS nanoparticles is shown in Fig. 2. Once the ligand gets stabilized on the surface of the nanoparticles, its motion is restricted and this results in the broadening of the different
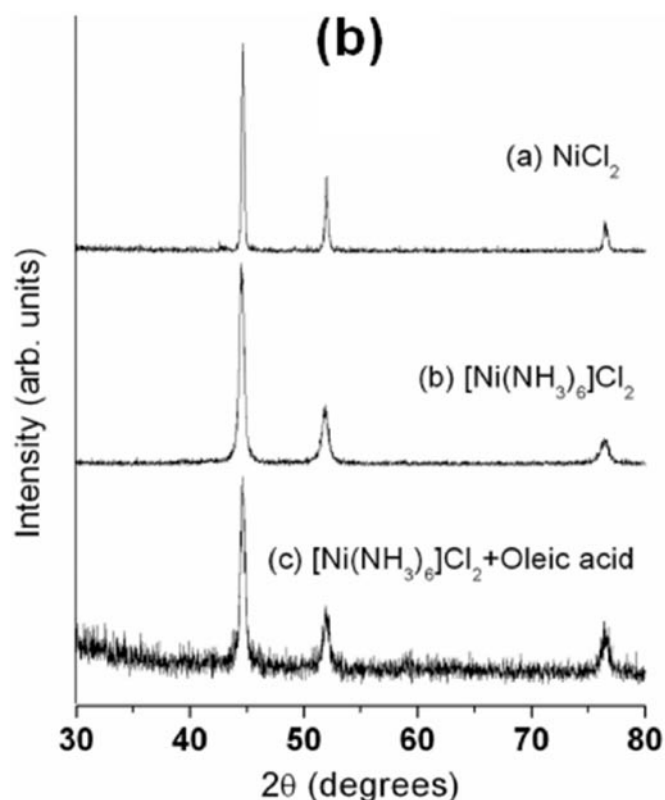
Fig. 3: XRD patterns of Ni particles prepared from different precursors (a) NiCl$_2$ and (b) [Ni(NH$_3$)$_6$]Cl$_2$ and (c) [Ni(NH$_3$)$_6$]Cl$_2$ with oleic acid.

vibrational modes of the ligand molecule. This is clear from the comparison of line widths corresponding to different vibrational modes in free ligand and ligand stabilised on the nanoparticles. A representative IR pattern from ethylene glycol stabilized CdS nanoparticles is shown in Fig. 2.

XRD patterns of Ni particles prepared by using EG as a solvent and a reducing agent with different precursors is shown in Fig. 3. The crystallite sizes are dependent on precursors used [22]. The crystallite sizes of Ni particles prepared from [Ni(NH$_3$)$_6$]Cl$_2$ and NiCl$_2$ precursor are found to be 20 and 38 nm respectively. However, Ni particles prepared from [Ni(NH$_3$)$_6$]Cl$_2$ and stabilizing agent oleic acid have a crystallite size of 12 nm. The crystallite size of Ni particles prepared from NiO powder is found to be 35 nm, which is the same as that from NiCl$_2$ precursor.

These results are further confirmed by TEM images recorded for the samples. As prepared Ni nanoparticles have got interesting magnetic properties. In the following section we discuss the TEM image of representative

semiconducting oxide nanoparticles with very small size distribution and uniformly dispersed in amorphous TiO$_2$ (Fig. 4). The samples were prepared by using ethylene glycol as a solvent and urea as a precipitating agent. Highly crystalline regions with dimensions around 5 nm can be clearly seen from the images. The lattice fringes match well with that of different planes in cassiterite structure of SnO$_2$. The nanoparticles are surrounded by poorly crystalline regions characteristic of TiO$_2$ matrix. In other words crystalline regions in the samples are surrounded by amorphous matrix, characteristic of materials with core-shell geometry. Schematic representation of particle with core-shell geometry is shown in Fig. 4(b). Strong
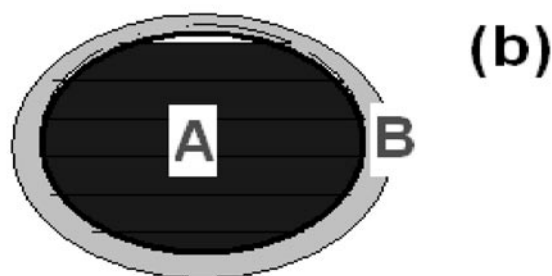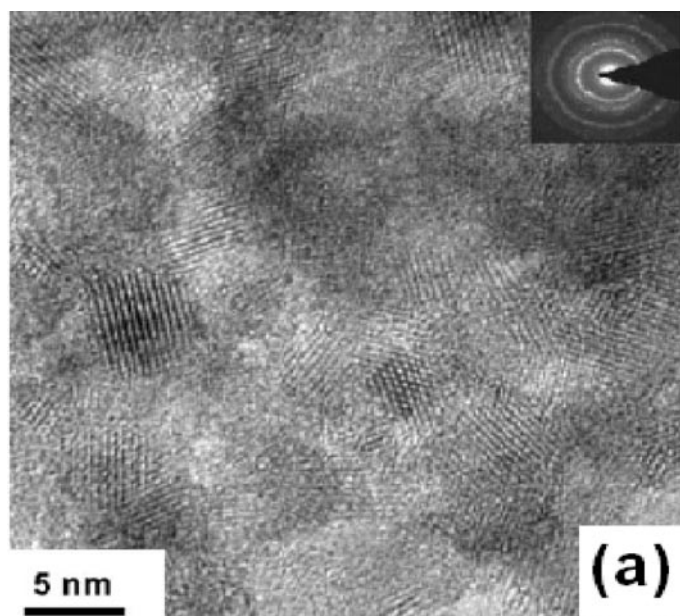
A = Crystallite Region
B = Surface

Fig. 4: HRTEM image and corresponding SAED pattern of (a) for as-prepared SnO$_2$:Eu–TiO$_2$ samples. Schematic representation of core-shell geometry existing in SnO$_2$:Eu–TiO$_2$ system is shown in Fig. 4(b).
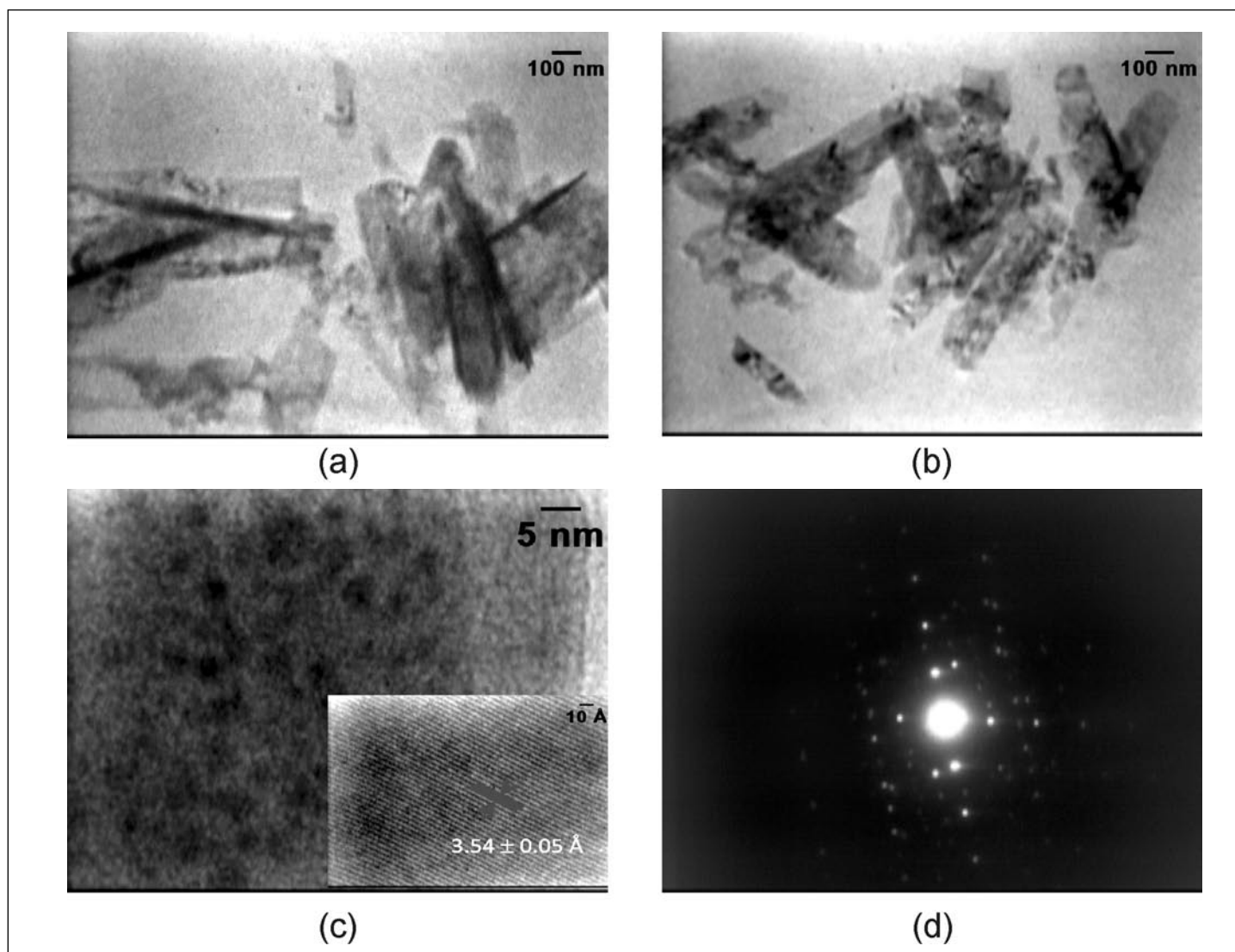
Fig. 5: *TEM images of (a) and (b) SbPO$_4$:Tb^{3+} nanoribbons, (c) SbPO$_4$:Tb^{3+} nanoparticles. Inset in Fig. 5(c) shows HRTEM image and Fig. 5(d) shows SAED pattern from nanoribbons.*
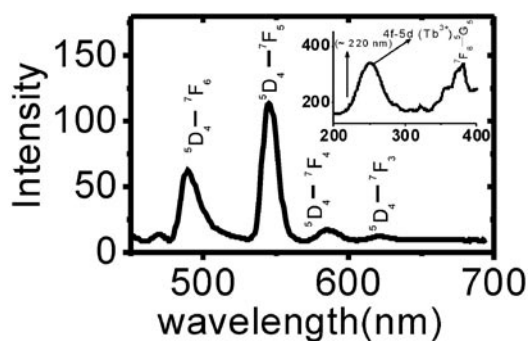
Fig. 6: *Emission spectrum of SbPO$_4$ nanoparticles/nanoribbons doped with 2.5 at % Tb^{3+} ions. Samples were excited at 250 nm.*

Eu^{3+} luminescence has been observed from these samples. Fig. 5 shows the TEM images of 5 at. % doped SbPO$_4$ nanomaterials prepared by using ethylene glycol-glycerol mixture (10 ml each). The images indicate the presence of both nano ribbons and nanoparticles of SbPO$_4$. The ribbons are having thickness in the range of 10-20 nm, length in the range of 500-700 nm and width around 100 nm (Fig. 5 (a and b)). The images are also found to have very fine nanoparticles having size in the range of 1-5 nm as can be seen from Fig. 5(c). High-resolution transmission electron microscopic (HRTEM) image of a nanoparticle is shown as an inset in Fig. 5(c). The line spacing of 3.54 ± 0.05 Å between

the lattice fringes matches well with the distance between the (ī01) planes of $SbPO_4$ lattice.

Selected area electron diffraction (SAED) patterns of both nanoribbons and particles showed highly crystalline nature of the samples (Fig. 5(d)).

Tb^{3+} doped $SbPO_4$ nanoparticles/nanoribbons showed strong Tb^{3+} emission characteristic of $^5D_4 \rightarrow {}^7F_3$, $^5D_4 \rightarrow {}^7F_4$, $^5D_4 \rightarrow {}^7F_5$, $^5D_4 \rightarrow {}^7F_6$ transitions, after excitation at 250 nm (Fig. 6). Excitation spectrum corresponding to 545 nm emission from these nanoparticles/nanoribbons is shown as an inset in the Figure. Along with less intense sharp peaks characteristic of intra 4f transitions of Tb^{3+} ions, broad peak around 250 nm, which is characteristic of 4f→5d transition of Tb^{3+} ions is also observed. The host absorption around 220 nm characteristic of $SbPO_4$ is not clearly seen as it has got buried under the intense 4f→5d transition peak. The intensity of 250 nm peak has been found to increase with increase in Tb^{3+} concentration in the nanoparticles/ nanoribbons.

Conclusions

A variety of nanoparticles can be prepared by using polyols as solvent and stabilising ligands. TEM and XRD studies have shown that the nanoparticles are highly crystalline and are having a very fine particle size distribution. The methodology does not require any toxic or moisture sensitive or exotic reagents and can be easily adapted. It has been observed that some of the nanoparticles morphology can be tuned by modifying the relative concentration of different polyols. Lanthanide ions doped nanoparticles prepared by polyol method are found to be highly luminescent.

References

1. http://chemicalland21.com/industrialchem/organic/POLYETHYLENE%20GLYCOL.htm

2. http://wapedia.mobi/en/Ethylene_glycol

3. http://www.inchem.org/documents/icsc/icsc/eics1517.htm

4. R. S. Ningthoujam, V. Sudarsan, S. V. Godbole, A. K. Tyagi, L. Kienle and S. K. Kulshreshtha, *Appl. Phys. Lett.* 90 (**2007**) 173113.

5. M. N. Luwang, R. S. Ningthoujam, S. K. Srivastava, Jaganath and R. K. Vatsa, **J.** *Am. Chem. Soc.* 132 (**2010**) 2759.

6. N. S. Singh, R. S. Ningthoujam, L. R. Devi, N. Yaiphaba, V. Sudarsan, S. D. Singh, R. K. Vatsa and R. Tewari, *J. Appl. Phys.* 104 (**2008**) 104307.

7. R. S. Ningthoujam, V. Sudarsan, A. Vinu, P. Srinivasu, K. Ariga, S. K. Kulshreshtha and A. K. Tyagi, *J. Nanosci. Nanotech.* 8 (**2008**) 1489.

8. L. R. Singh, R. S. Ningthoujam, V. Sudarsan, I. Srivastava, S. D. Singh, G. K. Dey, and S. K. Kulshreshtha, *Nanotechnology* 19 (**2008**) 055201.

9. L. K. Kurihara, G. M. Chow and P. E. Schoen, *Nanostruc. Mater.* 5 (1995) 607.

10. R. Minamia, Y. Kitamoto, T. Chikata and S. Kato, *Electrochimica Acta* 51 (**2005**) 864.

11. J. Bregado-Gutierrez, A. J. Saldı´var-Garcıa, and H. F. Lopez, *J. Appl. Polymer Science* 107 (**2008**) 45.

12. V. Tzitzios, D. Niarchos, G. Margariti, J. Fidler and D. Petridis, *Nanotechnology* 16 (**2005**) 287.

13. M. Tsuji, K. Matsumoto, N. Miyamae, T. Tsuji and X. Zhang, *Crystal Growth & Design 7* (**2007**) 311.

14. T. Tuval and A. Gedanken, *Nanotechnology* 18 (**2007**) 255601.

15. O. Palchik, R. Kerner, A. Gedanken, A. M. Weiss, M. A. Slifkinb and V. Palchik, *J. Mater. Chem.* 11 (**2001**) 874.

16. C. Feldmann, *Adv. Funct. Mater.* 13 (**2003**) 101.

17. H.-O. Jungk and C. Feldmann, *J. Mater. Sci.* 36 (**2001**) 297.

18. M. Siemonsa, T. Weirichb, J. Mayerb and U. Simona, *Z. Anorg. Allg. Chem.* 630 (**2004**) 2083.

19. C. Li, X. Liu, P. Yang, C. Zhang, H. Lian and J. Lin, *J. Phys. Chem. C* 112 (**2008**) 2904.

20. N. S. Gajbhiye, R. S. Ningthoujam, A. Ahmed, D. K. Panda, S. S. Umre and S. J. Sharma, *Pramana* 70 (**2008**) 313-321.

21. F. Fievet, J. P. Lagier, B. Blin, B. Beaudoin and M. Figlaez, *Solid State lonics* 32/33 (**1989**) 198.

22. R. S. Ningthoujam, N. S. Gajbhiye and S. Sachil, *Pramana 72, 577-586 (***2009***).*

23. F. Fievet, J.P. Lagier and M. Figlarz, Materials Research Society Bulletin, p. 29 (**December, 1989**).

24. N. S. Gajbhiye, S. Sharma and R. S. Ningthoujam, *J. Appl. Phys. 104 (***2008***) 123906.*

25. N. S. Gajbhiye, S. Sharma, A. K. Nigam and R. S. Ningthoujam, *Chemical Physics Letters 466 (***2008***) 181.*

26. A. Soni and G.S. Okram Appl. Phys. Lett. 95 (**2009**) 013101.

Pyrochlore Based Potential Electrolyte Materials

B. P. Mandal and A.K. Tyagi*

Chemistry Division, Bhabha Atomic Research Centre, Mumbai – 400085, India
*Corresponding author; E-mail: aktyagi@barc.gov.in

Abstract

The potential of $Gd_{2-y}Nd_yZr_2O_7$ series as electrolyte material have been described in this article. The ionic conductivity of the samples prepared by standard solid state route and gel combustion route has been compared. X-ray diffraction has been used for structural characterization for all the samples prepared by solid state and gel-combustion route. The total ionic conductivity increases with increase of disorder (Gd^{3+} content) in the system. The activation energy of conduction increases and the pre-exponential factor, which is proportional to the number of mobile species, also follow the same trend with increase in disorder. The total conductivity of the system does not change in reducing atmosphere which verifies negligible contribution of electronic contribution.

Keywords: pyrochlore, gel combustion method, electrolyte materials, ionic conductivity

Introduction

The materials having pyrochlore structure have been attracting a lot of attention due to their interesting physical properties and potential for technological applications like solid oxide fuel cell [1], oxygen sensors [2], superconductivity [3], luminescence [4] and ferromagnetism [5], catalysis [6] etc. In addition, zirconates are important ceramic waste forms for actinide immobilization and are among the principal host phases currently considered for the disposal of Pu from dismantled nuclear weapons [7]. Few reports are also there where MgO-zirconate based pyrochlore composites are considered to be suitable materials for inert matrix fuel [8].

Among the conductive pyrochlores, $Gd_2Zr_2O_7$ has shown great promise due to its high oxygen-ion conductivity at relatively lower temperatures compared to the commercially used electrolytes in solid oxide fuel cells [9]. In fact, the intrinsic ionic conductivity of $Gd_2Zr_2O_7$ is the highest reported among all the reported pyrochlores [10]. The unit cell of pyrochlore and fluorite are shown in Fig 1.

In this context, it is essential to mention that the samples prepared by solid state route (SSR) generally provide poor sintered density. However, the samples prepared by solid state route can give an idea about the trend of ionic conductivity on substitution. On the other hand, soft-chemical routes play an important role for the preparation of nano-materials which on further manipulation gives rise to highly dense pellets upon sintering at relatively low temperature. Among the solution-chemistry routes, the combustion technique is capable of producing the nano-crystalline powders of oxide ceramics at comparatively low calcination temperature in a short time with enhanced powder characteristics. Dense pellets can easily be prepared from soft agglomerated powders.

In this article the ionic conductivity of $Nd_{2-y}Gd_yZr_2O_7$ series, prepared by solid state route, in the temperature range 623 K to 696 K has been discussed. From these studies it has been found that when the concentration of Nd^{3+} and Gd^{3+} becomes nearly equal then ionic conductivity turns out to be maximum. But since, solid state synthesized samples in general do not have high density; therefore, gel-combustion (GC) method has been adopted to synthesize those samples which showed maximum ionic conductivity in the samples prepared by solid state route. The ionic conductivity of these samples (prepared by GC method) has been investigated in the higher temperature ranges i.e. from 648 K to 1073 K in air and reducing atmosphere.

Experimental details

The solid state synthesized samples were prepared as follows. Before the reaction, the starting materials i.e. Gd_2O_3, Nd_2O_3, ZrO_2 were heated at 1173 K for overnight. Then stoichiometric amounts of reactants, Gd_2O_3, Nd_2O_3, ZrO_2 (99.9%) were mixed to get compositions corresponding to $Gd_{2-y}Nd_yZr_2O_7$. The well-ground mixtures were heated in pellet form initially at 1473 K for 36 h, then at 1573 K for 36 h followed by one more heating at 1673 K for 48 h [11,12].

Finally, to obtain highly dense pellets the samples were heated at 1748 K for 10 h in air.
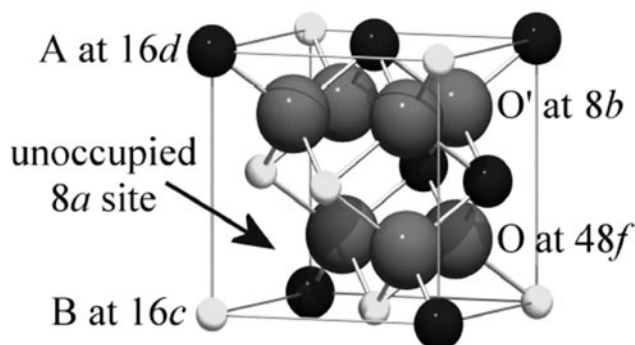
Black spheres represent A³⁺ cations, light gray B⁴⁺ and dark gray O²⁻.

(A)
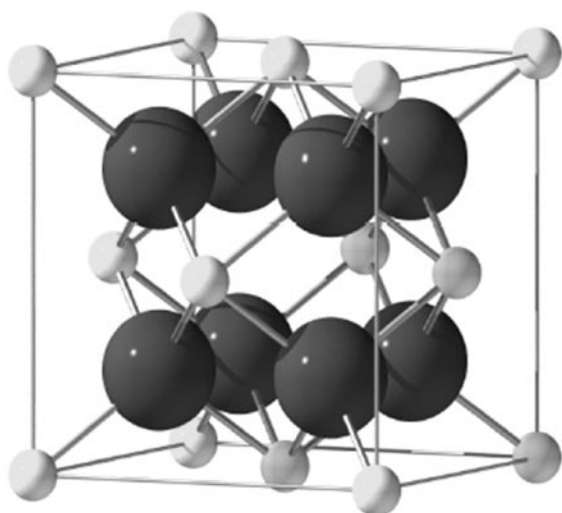
The light gray atoms represent 4⁺ cations and the dark atoms represent 2⁻ anions.

(B)

Fig. 1: Crystal structure of (A) pyrochlore and (B) fluorite

In order to synthesize the samples in nano form gel combustion method has been adopted. AR grade powders of Nd_2O_3, Gd_2O_3, zirconium oxy-nitrate $[ZrO(NO_3)_2 \cdot 3H_2O]$ and citric acid were used as the starting reagents. The rare-earth oxides were dissolved in minimum amount of dil. HNO_3. Nitrates and citric acid were taken in stoichiometric ratio. The solutions, after thermal dehydration on a hot plate were heated at 473 K. The powders obtained after auto-ignition were calcined at 873 K for 45 minutes. Subsequently, these

were cold pressed to 8 mm diameter pellets at a compaction pressure of 200 MPa using a uni-axial hydraulic press, and sintered at 1703 K for 6 h. Densities of the pellets were measured following Archimedes' principle.

The X-ray diffraction patterns were recorded in step scan mode on a Philips X'pert Pro unit with CuKα radiation and a step size 0.02°. The microstructure of the sintered pellets prepared both by solid state route (SSR) and gel combustion (GC) route were investigated using a VEGA TS 5130 MM Scanning Electron Microscope.

Ionic Conductivity Measurement

The ionic conductivity of the samples prepared in solid state route and gel combustion route were measured in different ac-impedance analyzers. For the samples prepared by SSR, the frequency-dependent conductivity was determined using an impedance analyzer (HP4194A). The impedance measurements were carried out over a frequency range of 100 Hz to 15 MHz at five different temperatures in the range 623-696 K. The samples in cylindrical pellet form, each about 8 mm diameter and 2 mm thick, were coated with air-drying silver paste for good electrical contact, and sandwiched between two square silver electrodes of 10 mm² cross-sectional area and 1mm thickness inside a vertical high-temperature cell.

For the samples prepared by gel combustion method the ionic conductivity measurements were carried over a temperature range of 648 K to 1073 K using an impedance analyzer in the frequency range 0.1 Hz to 1 MHz in air and also in hydrogen atmosphere. Platinum as current collecting electrode on either side of the sintered pellet was cured at 1223 K before the experiment.

Results and Discussion

Samples prepared by solid state route

The XRD patterns of all the samples were recorded and analyzed. When the radii of A and B cations in $A_2B_2O_7$ are similar, the compound crystallizes in the defect-fluorite form and the superstructure peaks completely disappear. The ionic radii of Gd^{3+}, Nd^{3+} and Zr^{4+} are 0.98 Å (in 8-fold coordination) 1.02Å (in 8-fold coordination) and 0.72 Å (in 6-fold coordination) respectively. The r_A/r_B of $Gd_2Zr_2O_7$ is 1.35 and that of $Nd_2Zr_2O_7$ is 1.42 which indicates that the possibility of swapping of A and B cation is higher in $Gd_2Zr_2O_7$ than that in $Nd_2Zr_2O_7$. In the solid solution, $Gd_{2-y}Nd_yZr_2O_7$, the degree of disorder increases from y = 2.0 to y = 0.0. For determination of the extent of

disorder, Rietveld analysis has been done on the XRD patterns of some of the samples. The x-parameter of *48f* oxygen increases from 0.332(1) for *y* = 2.0 to 0.344(1) for *y* = 0.0.

The densities of all the pellets were found to be around 90 - 92% of the theoretical density.

Ionic conductivity of the samples prepared by solid state method

The ac impedances at different temperatures were plotted in the complex plane for all samples studied. Fig. 2 shows the plot for the sample with y = 1.0. Two semicircular arcs are clearly visible at each temperature value. The low-frequency arc corresponds to the contribution from the grain boundaries while the high-frequency arc represents the bulk contribution to the impedance.

These two contributions were separated by fitting semi-circles to each of the arcs, and the dc bulk and grain boundary resistance values, R_{dc} and R_{gb} respectively, were obtained from the intercepts of these arcs on the Z' axes.

The dc conductivity follows the Arrhenius behavior

$$\sigma_{dc} T = \sigma_0 \exp(-E / k_B T)$$

where *E* is the activation energy for conduction, *T* is the temperature, k_B is the Boltzmann constant, and σ_0 is a pre-exponential factor that depends upon the concentration of mobile species. The values of activation energy *E* were determined from the slopes (Fig not shown).

Fig. 2: Complex impedance plot of GdNdZr$_2$O$_7$ prepared by solid state route at 642 and 661K.

It has been found that both the bulk conductivity σ_{dc} and its activation energy *E* show a dependence upon the Nd^{3+} content, *y*. The variation of σ_{dc} with Nd content (y) is shown in Fig 3. There exists an intermediate composition (y ≈ 1.0) at which the dc conductivity shows maxima at all temperatures studied in our experiments. This peaking behavior, with the increase in bulk σ_{dc} of about an order of magnitude at around *y* = 1.0 over that in Gd$_2$Zr$_2$O$_7$ (*y*=0.0), is significant since it has been reported that Gd$_2$Zr$_2$O$_7$ has the highest conductivity among the rare-earth zirconate pyrochlores. Our results suggest that the conductivity of the Gd$_2$Zr$_2$O$_7$ system can be tailored. The activation energy for bulk conduction was found to steadily increase as Nd^{3+} content decreases.

Fig. 3: Variation of bulk dc conductivity with Nd concentration of the samples prepared by solid state route at different temperatures.

It has also been observed that the pre-exponential factor σ_0 behaves in a manner similar to *E*. It steadily increases with decreasing Nd^{3+} content, indicating that the effective number of mobile oxygen ions increases as Gd replaces Nd at the *A* site. This is consistent with the observation that there is greater disorder upon incorporation of Gd^{3+} in the lattice. The variation of *E* and σ_0 with *y* for bulk conduction is shown in Fig. 4. The increase in σ_0 would lead to an increase in conductivity, but the increase in *E* would hinder the oxygen ion migration. Thus the two processes are competing, and the drop in conductivity as y reduces from 1.0 to 0.0, while both σ_0 and *E* are increasing, could be attributed to the fact that the increase in *E* compensates for

the increase in number of mobile species thus decreasing the ease with which the ions can migrate. The apparent increase in activation energy of migration has been attributed to increased correlation among the mobile ions.

Samples prepared by gel combustion method

The XRD pattern of the product calcined at 873 K shows the presence of main peaks corresponding to basis cell of pyrochlore lattice. However, due to presence of broad peaks and noisy background for the samples calcined at 873 K, the superstructure peaks, characteristic of pyrochlore orderings are difficult to visualize. The superstructure peaks starts to become prominent upon further heating (Fig not shown).

The SEM micrographs of the sintered pellets reveal that these are dense pellets with very few pores (Fig not shown). The average sizes of the grains are around 0.8-1.0μm. The density measured by Archimedes principle of all the pellets was found to be more than 90% of theoretical density.

Ionic Conductivity of the samples prepared by gel combustion method

The ionic conductivity of these samples was determined from measured impedance data. Typical impedance spectra of the material $Nd_{1.2}Gd_{0.8}Zr_2O_7$ measured in air at 773 K, 823 K and 873 K are shown in Fig. 5. At 773 K only arc due to grain boundary was observed and this semicircular arc was simulated and fitted using the ZView software to obtain R_g, R_{gb} and capacitance.

The absence of the arc due to grain contribution could be due to frequency limitation of the Solartron instrument. In this case the capacitance value of the grain conductivity-relaxation process is very small. It can be seen that as the measuring temperature increases both R_g and R_{gb} decrease significantly. At temp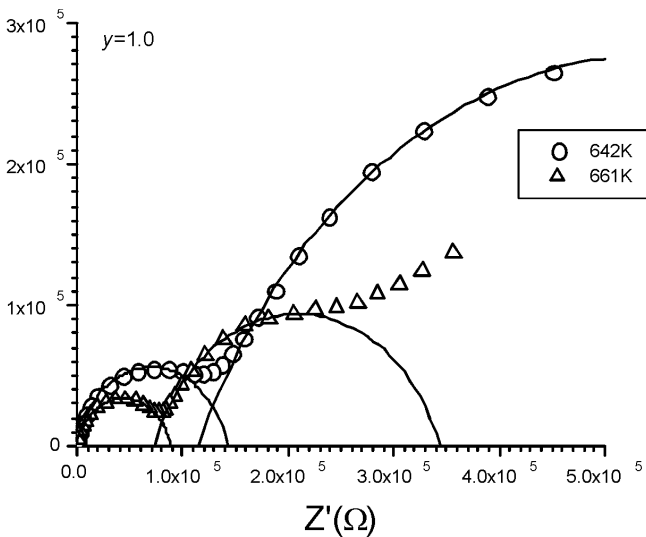erature above 873 K the arc due to grain boundary contribution was found to disappear and electrode polarization process dominating the electrical conduction mechanism and therefore simply total resistance was estimated.

In case of oxide ion conductors, when grain boundary resistance is evaluated in a small temperature range of measurement, the variation of grain size of samples sintered at different temperatures is studied as a function of grain boundary resistance. In some cases, with the decrease of grain boundary resistance the grain size increases. However, in the present work, all the three pyrochlore compositions were sintered at 1703 K and grain size was
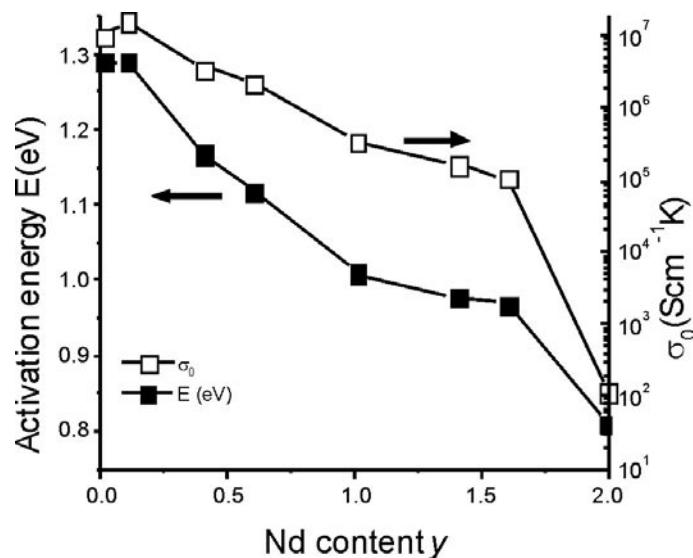
Fig. 4: Change in activation energy (left vertical axis) and pre-factor (right vertical axis) with Nd concentration in $Gd_{2-y}Nd_yZr_2O_7$ series (samples prepared by solid state route).
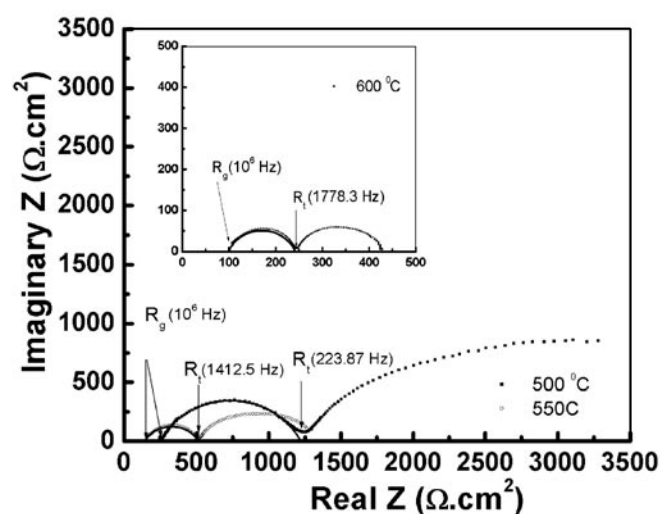
Fig. 5: Impedance spectra of $Gd_{0.8}Nd_{1.2}Zr_2O_7$ sample at 773, 823 and 873 K in air (samples prepared by gel combustion route)

found to increase slightly with Gd^{3+} concentration with value in the range 0.8-1.0 μm.

The values of E and σ_0 can be obtained from the slope and intercept of linear fits to the data. The activation energy ranges from 0.98 to 1.06 eV with increase in Gd^{3+} content in the series which agrees with oxide ion migration. The results are summarized in Table 1.

Table 1: Electro-physical properties of the different compositions in the series Gd$_{2-y}$Nd$_y$Zr$_2$O$_7$ (y = 0.8, 1.0, 1.2) in air and H$_2$ atmosphere

Samples	Electrical conductivity (S/cm)						E$_a$ (eV) in H$_2$ flow
	773 K		873 K		923 K		
	air	H$_2$	air	H$_2$	air	H$_2$	
y = 1.2	3.88E-5	3.10E-5	1.95E-4	2.11E-4	3.66E-4	3.90E-4	1.01 eV
y = 1.0	1.99E-5	2.36E-5	1.15E-4	1.29E-4	2.61E-4	2.63E-4	1.10 eV
y = 0.8	1.02E-5	1.30E-5	6.27E-5	7.07E-5	1.36E-4	1.57E-4	1.11 eV

The interesting observation is that the activation energy in air (E$_a$) and the pre-exponential factor (σ_0) increases with increase in Gd^{3+} content in the solid solution. It has been reported earlier that with increase in Nd^{3+} content in the Gd$_{2-y}$Nd$_y$Zr$_2$O$_7$ series the degree of order increases [13]. On the other hand, with increase in Gd^{3+} content in the same series, the degree of disorder in the crystal increases which causes hindrance to the mobility of oxide ions which in turn results in an increase in the activation energy. The pre-exponential factor is proportional to the number of mobile species (concentration of oxygen ion vacancy) which increases on increasing the disorder in the system. Since only single activation energy is observed in the measured temperature range for all the samples, the concentration of mobile species in the pre-exponential factor is temperature independent. Another important observation is that the electrical conductivity of all the samples measured in the reducing atmosphere between 723-923 K, does not differ significantly from the values obtained in air (Table 1).

In the present work, the electrical conductivity of Gd$_{2-y}$Nd$_y$Zr$_2$O$_7$ is reported in two extreme oxygen partial pressure ranges e.g., air and H$_2$ atmosphere and between 773-923 K no significant change in conductivity is observed (Table 1)**.** With different gas mixture compositions at four intermediate oxygen partial pressures, the electrical conductivity was also measured and as expected no change of conductivity was observed with respect to that in air. Thus for all the synthesized pyrochlores in the present work, Nd^{3+}, Gd^{3+} and Zr^{4+} ions are very stable in H$_2$ environment till the measuring temperature as high as 923 K. Therefore, it can be concluded that in the measured temperature range these materials possess only oxygen ionic conduction even at low P$_{O_2}$ and no significant electronic conduction is introduced into the electrolyte, a criterion which is essential for an electrolyte material for application in electrochemical devices like solid oxide fuel cell, oxygen sensor etc.

Conclusions

The nano powder of several single phasic zirconates pyrochlores could be prepared using citrate-nitrate combustion route easily. The presence of ultra fine grains in sintered pellets was established by SEM studies. The ac impedance analysis shows that the pre-exponential factor and the activation energy for intra-grain conduction increase with increase in Gd^{3+} content in the series. The materials showed exceptional stability in reducing atmosphere also.

References

1. B.P. Mandal, A. Banerji, V. Sathe, S.K. Deb and A.K. Tyagi, *J. Solid State Chem.* 180 (**2007**) 2643.

2. M.T.Weller, R.W.Hughes, J.Rouke, C.S.Knee and J.Reading, *Daltn Trans.* 3032 (**2004**).

3. J. Yamaura, Y. Muraoka, F. Sakai, and Z. Hiroi *J. Phys. Chem. Solids,* 63 (**2002**) 1027.

4. J. K. Park, C. H. Kim, K. J. Choi, H. D. Park, and S. Y. Choi, *J.Mater. Res.,* **16** (**2001**) 2568.

5. M. J. P. Gingras, B. C. den Hertog, M. Faucher, J. S. Gardner, S. R. Dunsiger, L. J. Chang, B. D. Gaulin, N. P. Raju, and J. E. Greedan, *Phys. Rev. B,* **62** (**2000**) 6496.

6. F. Sayed, V. Grover, K. Bhattacharyya, D. Jain and A. K. Tyagi, *J. Phys. Chem C* (Communicated)

7. M. K. Patel, V. Vijaykumar, D. K. Avasthi, S. Kailas, J. C. Pivin, V. Grover, B. P. Mandal and A. K. Tyagi, *Nucl. Instrum. Methods Phys. Res. B* 266 (**2008**) 2898

8. A. Imaura, N. Touran and R.C. Ewing, *J. Nucl. Mater.* 389 (**2009**) 341

9. A. J. Burggraaf, T. van Dijk and M. J. Verkerk, *Solid State Ionics* 5 (**1981**) 519.

10. M. P. van Dijk, K. J. deVries and A. J. Burggraaf, *Solid State Ionics 9* (**1983**) 913.

11. B. P. Mandal and A K Tyagi, *Mater. Sci. Eng. B* 136 (**2007**) 46.

12. B. P. Mandal and A K Tyagi, *J. Alloys Compds* 437 (**2007**) 260.

13. B. P. Mandal, S.K. Deshpande, and A. K. Tyagi, *J. Mater. Res.* 23 (**2008**) 911.

Ternary Niobates and Tantalates: Materials for microwave Dielectrics

Masood A Nath[a], M. Thirumal[b], Vishnu Shanker[a #] and A. K Ganguli[a*]

[a]Department of Chemistry, Indian Institute of Technology, Hauz Khas, New Delhi 110016, India
[b]Department of Chemistry, University of Delhi, Delhi 110007, India
[*]Corresponding author; E-mail: ashok@chemistry.iitd.ernet.in

Abstract

Niobium and tantalum-based ternary oxides have been found to be good candidates for electronic applications because of their excellent dielectric properties. The investigations on these materials continue to remain a hot area of scientific research due to their wide range of applications in microwave technology. The niobates and tantalates of the type $A(B_{1/3}B'_{2/3})O_3$ or $A_3BB'_2O_9$ such as $Ba_3MgNb_2O_9$ (BMN), $Ba_3MgTa_2O_9$ (BMT), $Ba_3ZnNb_2O_9$ (BZN), $Ba_3ZnTa_2O_9$ (BZT) etc., are perovskite related oxides with disordered (cubic) or ordered (-B-B'-B'-B-) hexagonal structure depending on the temperature and other conditions of synthesis. The substitution studies at A, B and B' site of the perovskites are discussed along with the phase stability, ordering, sintering behavior and dielectric properties. The other class of oxides (AB_2O_6) which also has niobates and tantalates in their B-site exhibits excellent dielectric properties have been reviewed. The various methods of synthesis of these oxides have been included.

Keywords: niobates, tantalates, dielectric constant, dielectric loss, microwave properties.

Dielectric Properties

Dielectric materials are used mainly in capacitors, dielectric resonators, filters to stabilize oscillators and as electrical insulators. Good dielectric materials should posses a high dielectric constant, a high dielectric strength, (they should be able to withstand high voltages without undergoing degradation) and low dielectric loss, the loss of electrical energy as heat on application of potential should be minimum. Dielectric properties [1] arise due to short-range motion of electrical charges under the influence of an applied electric field. This leads to the polarization of charges and hence storage of electrical energy, which is used as capacitors for charge storage device at low frequency whereas at high frequency (microwave region) these materials are used as resonators, filters etc.

The Need for Niobium and Tantalum Based Materials

Though in the past two decades there has been a continuous growth of wireless communication technology operating at microwave frequencies still there is an ever-increasing demand for low-cost and high performance dielectric materials. The progress and performance of materials depends on the source [2] and cost [3]. The interest in tantalum and niobium based dielectric materials has thus continue growing due to lowering cost and the high performance of these ceramics. Ternary niobates and tantalates of various metals are widely used in contemporary technology. In wireless communication system at microwave region, such materials are of immense interest due to their applications as filters, oscillators, dielectric resonators in mobile phones communication, and satellite telecommunications [4] technology. In addition, these materials exhibit ferro-, piezo-, pyro-electric, electro-optical, and other properties [5-6]. Materials based on them are employed in the production of ceramic generators of ultrasound, sound pickups, piezoelectric microphones and telephones, strain gauges, hydro acoustic collectors (receivers) of energy, laser crystals etc. [7]. The development of the latest technology and the consequent requirement for new materials has led to exceptional interest in the niobates and tantalates of tervalent metals. The successful combination of various physical properties like chemical inertness, high resistance to heat and moisture and mechanical strength of the niobates and tantalates of the tervalent metals makes them to be placed among the most important materials of advanced technologies. Several niobium and tantalum based dielectric oxides with perovskite structure have been found to have potential applications in communication technology [8-10]. However, search for new compounds with optimal dielectric properties continues to be of great interest.

[#]Current Address: Department of Chemistry, National Institute of Technology, Warangal, A.P. 506 004, India

One of the applications of these materials is as dielectric resonators, which have a resonant frequency (f_r) in the microwave region, typically between 1 and 10 GHz. To be an effective dielectric resonator, such material should have a sufficiently high relative permittivity to allow miniaturization of the component (ε_r >10), low dielectric losses (tan δ) at microwave frequencies to improve selectivity and a temperature coefficient of resonant frequency as close to zero as possible for temperature stability (τ_f ~ 0 ppm/^{0}C) [11-13]. Rather than tan δ, the quality factor (Q) is often measured, where Q ~ 1/tan δ, so a high Q is essential in dielectric resonators.

Kawashima et al [14] showed for the first time that a material having perovskite structure with formula $BaZn_{0.33}Ta_{0.67}O_3$ (BZT) can have excellent dielectric properties suitable for microwave devices. Materials of the general formula $Ba(B'_{0.33}B''_{0.67}O_3)$, where B′=Zn or Mg and B′=Nb or Ta have shown very interesting dielectric properties at high frequency [15,16]. Dielectric materials of tantalates such as $BaZn_{0.33}Ta_{0.67}O_3$ (BZT) [16] and $BaMg_{0.33}Ta_{0.67}O_3$ (BMT) [17] are currently available with ε_r around 30–35, near-zero τ_f and Q.f of 150000–300000 GHz. Desu and Bryan [18] showed that microwave loss quality Q could be improved by sintering at high temperature and the control of ZnO loss from the sample was found to be important, in controlling the properties of sintered ceramics. Tremendous research efforts were undertaken to improve the properties [19] as well as to understand the dominant mechanism of the dielectric loss in these materials [20-21]. Intrinsic microwave dielectric loss in $Ba(B'_{1/3}B''_{2/3})O_3$ originates from the two-phonon difference absorption process [22]. The only way to minimize this loss is to achieve a complete 1:2 ordering of B′ and B″ cations. However, recent studies suggest that extrinsic dielectric loss due to the point defects or second phase may dominate in practical ceramics [23]. The presence of the point defects (e.g., vacancies, dopant ions etc.) may alter the phonon spectrum resulting in a one-phonon absorption mechanism at microwave frequencies. For example, the problem of stabilization of the oxidation state of Ni in $Ba(Zn_{1/3}Ta_{2/3})O_3$ ceramics doped with Ni and Zr has been recently addressed by Rong *et al* [21]. The dielectric properties of some of the ternary niobate and tantalate complex perovskites of barium such as $Ba(Mg_{1/3}Ta_{2/3})O_3$, $Ba(Mg_{1/3}Nb_{2/3})O_3$ (BMN), $Ba(Ni_{1/3}Ta_{2/3})O_3$ (BNT), $Ba(Ni_{1/3}Nb_{2/3})O_3$ (BNN), and $Ba(Zn_{1/3}Nb_{2/3})O_3$ (BZN), BMT, BMN, BNT, BNN, and BZN are given in Table 1 [24].

Fig. 1a shows the dependence of the ceramic density on sintering temperature. A number of investigations indicated that both the low dielectric loss and high dielectric constant could be only realized in ceramics having a relative density of higher than calculated density 94% [15-19]. The density of BMT, BMN, BZN, and BNN samples increased with sintering temperature to a maximum and then gradually decreased at higher sintering temperature as shown in Fig. 1a. From the figure it is clear that the sintering temperature of tantalates are relatively higher than their niobium counterparts with pronounced difference in the dielectric constant value between niobium and tantalum. The relative densities were calculated from

$$\rho = \frac{\rho_m}{\rho_{th}} \times 100$$

where ρ_m is the measured density and ρ_{th} is the theoretical density. Theoretical density of BMT, BMN, BNT, BNN, and BZN samples is reported to be 7.657, 6.236, 8.017, 6.554, and 6.511 g/cm³, respectively [25].

Table 1: Dielectric properties of $Ba(B'_{1/3}B''_{2/3})O_3$ type compounds (adapted from Kolodiazhnyi et al [24])

Composition	ε	Q x f (THz)	τ_f (ppm/°C)
$Ba(Mg_{1/3}Ta_{2/3})O_3$	24	430	+5.4
	23-24	300	-2.0 to +2.0
$Ba(Mg_{1/3}Nb_{2/3})O_3$	32	55	+33
	31-34	40	+21
	32	71	+30
$Ba(Ni_{1/3}Ta_{2/3})O_3$	23	50	-18
	22	95.5	-10.5 to -13.5
$Ba(Ni_{1/3}Nb_{2/3})O_3$	36	70	+20
	35.4	35	-4.9 to +5
$Ba(Zn_{1/3}Nb_{2/3})O_3$	41	87	+31
	41	55	+31

The dielectric constant (ε_r) versus sintering temperature of BMT, BMN, BNT, BNN, and BZN ceramics is shown in Fig. 1b. With the increase in sintering temperature (T_{sint}) dielectric constant is found to increase. The increase in ε_r related with an increase in ceramic density. In the case of BMT and BZN samples, however, ε_r initially increases until it reaches a maximum of 24 and 40 for a sintering temperature of 1650 and 1440 °C, respectively. At a higher T_{sint}, the dielectric constant of BMT and BZN samples slightly decreases due to the appearance of secondary phase
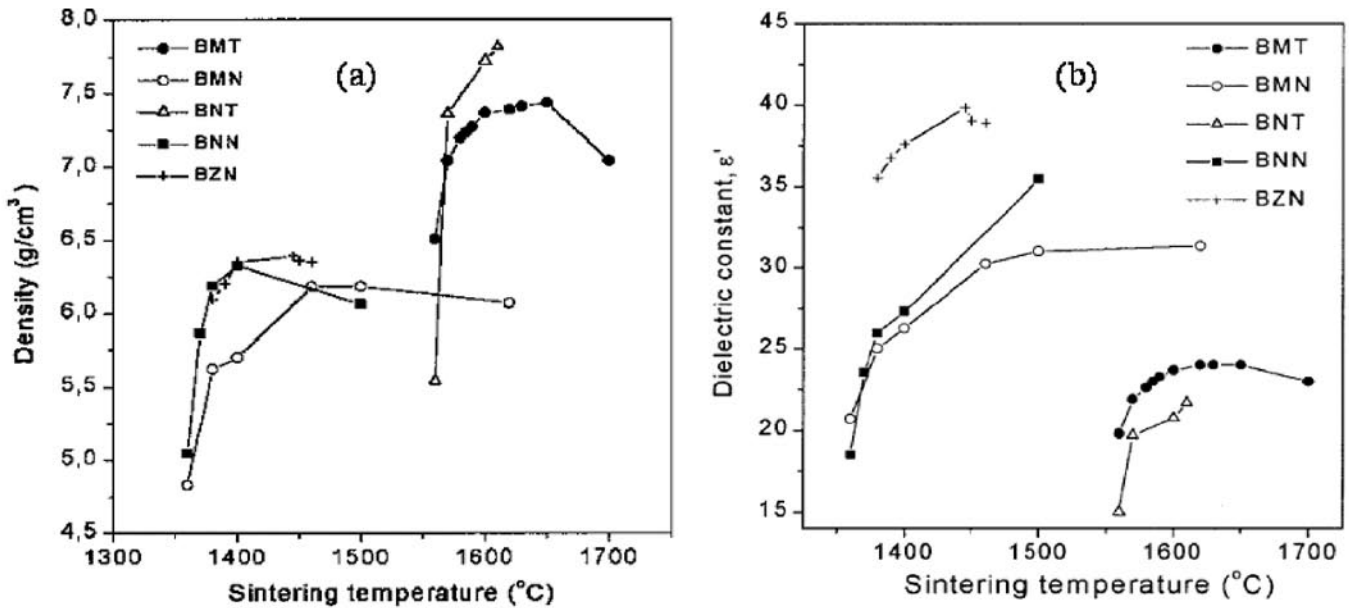
Fig. 1: (a) Density of BMT, BMN, BZN, BNN, and BNT samples sintered at different temperatures and (b) Variation of dielectric constant with sintering temperature (adapted from Kolodiazhnyi et al [24]).

as is evident from SEM studies [24]. The maximum values of ε_r at 10 GHz obtained for BMT, BMN, BNT, BNN, and BZN were 24, 31.4, 21.5, 35.4 and 40 respectively. These values are in a good agreement with those reported in the literature (Table 1).

The increase in ceramic density with sintering temperature is also evident from Zhang et al [26] in the synthesis of $Zn_{1-x}Mg_xNb_2O_6$ ceramics, the particles are densely packed. The homogeneous and uniform microstructure was observed for all x values. The grains exhibit two different size ranges and the fraction of large grain(~40 μm) is greater than that of small grains(~5 μm). The maximum dielectric constant of this compound ranged from 23.6 to 19.2, the Q.f values between 81220 to 33112 GHz and the τ_f from -70.56 to -29.46 ppm/^{0}C as x varied from 0 - 1. Another class of ternary oxides of the type AB_2O_6 oxides where A is an alkaline-earth oxide and B is Nb or Ta have also been investigated for their microwave dielectric properties [27-29]. Most of the niobates of this type have the columbite structure while the tantalates have a variety of related structures depending on the 'A' cation. For example $MgTa_2O_6$ has the trirutile structure while $CaTa_2O_6$ has the aeschynite and $ZnTa_2O_6$ has the tri-α-PbO_2 structure.

In the AB_2O_6 columbite structure, the A and B cations are at the center of octahedra surrounded by six oxygen atoms. The AO_6 and BO_6 octahedra form independent zig-zag chains by sharing edges, and the chains are connected by sharing corners in the order AO_6 chain-BO_6 chain-BO_6 chain (Fig. 2a). In the fully ordered state, this forms repeat as ABBABB octahedral layers, with an orthorhombic α-PbO_2 type structure, first solved by Sturdivant [30]. The unit cell is orthorhombic, space group no. 60 (*Pbcn*), with lattice parameter ratios of approximately 1:1.14:2.5 (Fig. 2b) [31]. Pullar et al [32] reported the lattice parameters, densities and cell volumes for columbite niobates. The lattice parameters and crystal structure of $MgNb_{2-x}Ta_xO_6$ (0 < *x* < 2) using MgO as a starting material have been reported[33], except the $MgTa_2O_6$ all other compositions crystallize in the orthorhombic crystal system. The dielectric properties are shown in Fig. 3. The dielectric constant does not vary much with composition lying in the range 14.8 to 16.0 at 500 kHz. The dielectric loss is nearly constant till *x* = 1 and varies between 0.025 and 0.035 at 500 kHz. The loss is somewhat higher for the *x* = 2 composition and has a value of 0.17.
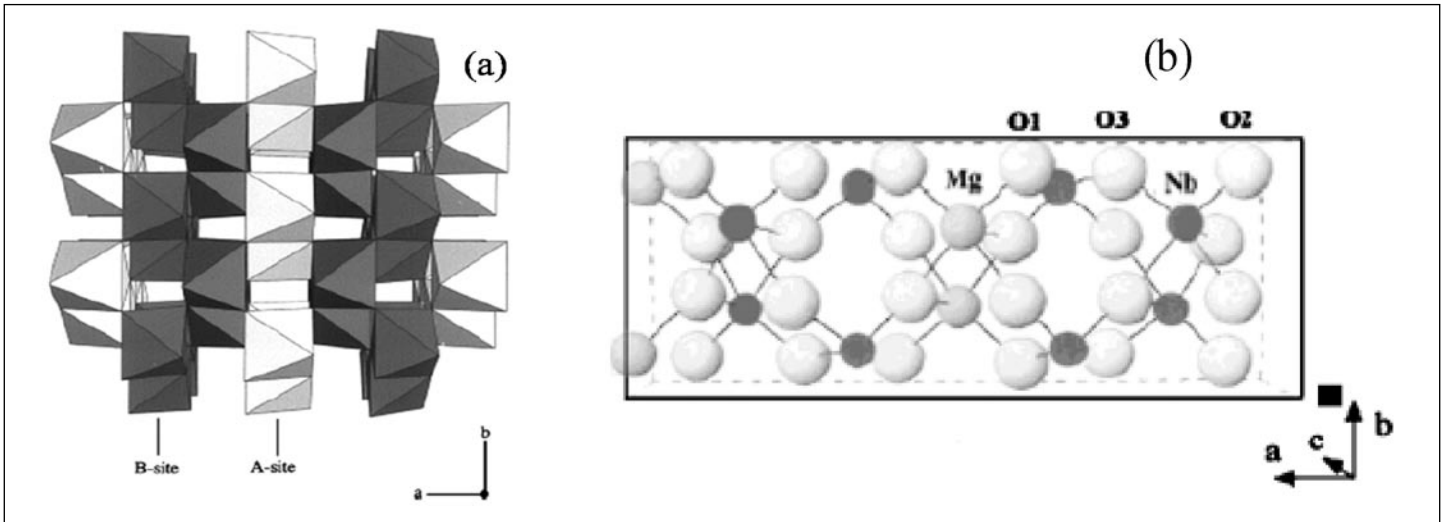
Fig. 2: (a) Columbite octahedral structure (A=M²⁺, B=Nb⁵⁺) (b) Unit cell of columbite MgNb₂O₆ projected along the c [001] axis (adapted from M. Maeda et al [31]).
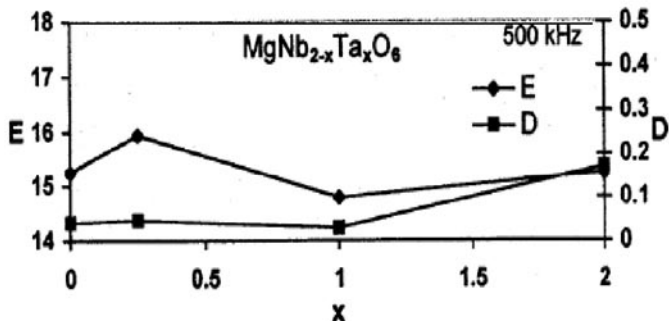

Fig. 3: Plot of variation of dielectric constant (E) and loss (D) with composition at room temperature and at a frequency of 500 kHz (adapted from Thirumal et al [33])

The powder X-ray diffraction studies of the calcined samples of MgNb$_{2-x}$Ta$_x$O$_6$ show single phases for the entire range of solid solution. All the oxides containing niobium crystallize in the orthorhombic columbite structure, while the pure tantalum analog crystallizes in the tetragonal structure [34]. Powder XRD taken on the disks after sintering at 1250 °C also show a single phase. It must be noted that our earlier studies starting with MgO instead of Mg(NO$_3$)$_2$.6H$_2$O lead to at least 15–20% of secondary phases (mainly Nb$_2$O$_5$ or Ta$_2$O$_5$) along with the major AB$_2$O$_6$-type phase [32]. These oxides had been sintered up to 1300 °C. Thus, by using Mg(NO$_3$)$_2$.6H$_2$O increases the reactivity and allows the formation of pure phases even at low temperatures of 1100 °C. Scanning electron micrographs of oxides of MgNb$_{2-x}$Ta$_x$O$_6$ sintered at 1250 °C shows particle size of 7 to 10 microns, and the particle size decreases with increasing tantalum concentration. In our earlier study using MgO as a source [33] the particle size is less than 3 μm. This shows that Mg(NO$_3$)$_2$.6H$_2$O not only leads to pure phases but also increases the sinterability of the particles. The grains are densely packed, with hardly any pores.

Variaton of dielectric constant of the sintered disks with frequency for the entire range of compositions is shown in Fig. 4a. There is a small decrease in the dielectric constant with frequency. The dielectric constant at 500 kHz for different compositions was found to be in the range 16 to 28 while the dielectric loss varies from 0.01 to 0.002 (Fig. 4b). The dielectric constant at 500 kHz for MgNb$_2$O$_6$ was found to be 24 and for MgTa$_2$O$_6$ it was 28. We also found that the dielectric constant of the pure end members, x = 0 and x = 2 are higher compared to the solid solution (x = 0.5, 1.0 and 1.5) as shown in Fig. 4a. It must be noted that within the same structure (columbite) the dielectric constant decreases as Ta is substituted. However, for x =2 composition, MgTa$_2$O$_6$ shows a much higher dielectric constant (ε = 28). This may be due to the different structure (tetragonal, trirutile) of MgTa$_2$O$_6$ compared to the columbite structure present in all other oxides.

The temperature coefficient of dielectric constant (τ$_f$) was also reported by Thirumal *et al* [34] for all the materials synthesized by using Mg(NO$_3$)$_2$6H$_2$O. For MgNb$_2$O$_6$ the dielectric constant varies from 24 to 23.5 with increasing the temperature from 25 to 300 °C. The dielectric constant
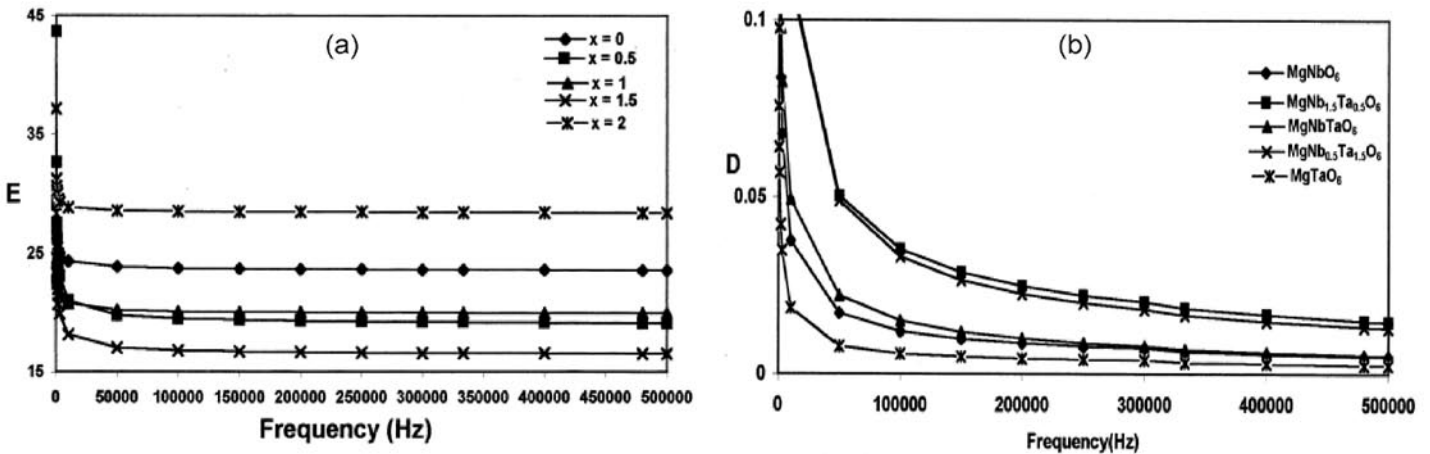
Fig. 4: Plot of the variation of (a) dielectric constant (ε) and (b) dielectric loss with frequency at room temperature for MgNb$_{2-x}$Ta$_x$O$_6$ system (adapted from Thirumal et al [34]).

decreases systematically with increase in temperature (negative temperature coefficient of the dielectric constant). However, the decrease is very small, and the temperature coefficient of dielectric constant was found to be -2 to 3 ppm/^{0}C at 500 kHz (even for other Nb-substituted compositions, τ_ε was found to be of similar value). In MgTa$_2$O$_6$, however, the dielectric constant increases by a small value from 27.9 to 28.3 as temperature is increased from 25 to 250°C. Thus, it has a positive temperature coefficient of the dielectric constant (τ_ε = 0.9 ppm/^{0}C). In Table 2, the dielectric properties of other columbites are shown. Similar oxides synthesized from our lab have been reported elsewhere [35].

Crystal structure and Effect of Substitution

A large number of compounds containing niobium and tantalum as one of the B' ions in the perovskite A(B$_{1/3}$B'$_{2/3}$)O$_3$ or A$_3$BB'$_2$O$_9$ were prepared by Roy[36] and independently by Galasso et al [37]. These oxides crystallize as ordered hexagonal phases (triple perovskites) with an 1:2 ordering of the B-cations (-B-B'-B'-B-) resulting hexagonal structures (Fig. 5). The first description of 1:2 order was given by Galasso et al.[38] for Ba(Sr$_{1/3}$Ta$_{2/3}$)O$_3$, in which a 1:2 layering of Sr and Ta (..SrTaTaSr..) along the [111] direction (ordering vector 1/3.[111] yields a hexagonal superstructure with a_{ord} = $ac\sqrt{2}$ and c_{ord} = $ac\sqrt{3}$ with *p$\bar{3}$m1* symmetry (Fig. 5). This arrangement was subsequently observed in other niobate and tantalate members of the A^{2+}(B$^{2+}_{1/3}$B$^{5+}_{2/3}$)O$_3$ family with A^{2+} = Ca, Sr, Ba; B^{2+} = Mg, Ca, Sr, Mn, Fe, Co, Ni, Cu, Zn; and B^{5+} = Nb, Ta. [39–41].

The 1:2-ordered A^{2+}(B$^{2+}_{1/3}$B$^{5+}_{2/3}$)O$_3$ tantalates and niobates e.g., Ba(Mg$_{1/3}$Ta$_{2/3}$)O$_3$(BMT), Ba(Zn$_{1/3}$Ta$_{2/3}$)O$_3$(BZT) and Ba(Zn$_{1/3}$Nb$_{2/3}$)O$_3$ (BZN), have been extensively studied because their very low dielectric losses and are ideally suited for dielectric resonator applications in commercial microwave communication devices.

Several of these investigations have been focused on kinetic aspects of the formation of the layered 1:2 order, which can nucleate and grow along <111> directions of the parent cubic structure [42]. The microstructures are typically composed of nanosized domains, on all possible orientational variants of the 1:2 order and the resultant high volume of disordered and elastically strained domain boundaries can adversely affect the dielectric properties [43]. Although the niobate and tantalate members of this family exhibit identical ordered structures, the covalency of Nb and Ta may be responsible for the stability of ordering. For a given stoichiometry the transition to a disordered B-site arrangement in the more ionic tantalates always occurs at a higher temperature compared with their niobate counterparts. The difference in stability has important ramifications for the processing of niobate microwave ceramics such as Ba(Zn$_{1/3}$Nb$_{2/3}$)O$_3$ for which the transition (~1375 °C) to the lower dielectric loss occurs during cooling from the sintering temperature (~1500 °C). Therefore, optimization of the dielectric properties requires the incorporation of a lower temperature anneal or slow cooling treatment to coarsen the ordered domains [44-46].

Substitutions at A, B and B' sites in the perovskite structure influence the dielectric properties to a great extent.

Table 2: Comparison of all available microwave results for columbite niobates
(adapted from Pullar et al [32])

Composition	ε	Qxf (GHz)	τ_f (ppm)	f_r (GHz)	Sintering	Expt. Density
$ZnNb_2O_6$	23.2	84500	-75.8	6.29	1200°C/2h	94.4%
	23.7	81220	~ -58	6-8	1150°C/2h	99%
	23.0	82200	-71.2	6-10	1150°C/2h	97%
	23.7	74500	-55	4-6	1200°C/2h	98.1%
$MgNb_2O_6$	19.9	79600	-64.9	6.79	1300°C/2h	93.9%
	21.4	93800	-70	10	1300°C/2h	>95%
	19.2	68805	~ -70	6-8	1350°C/2h	95.5%
	23	104000	-61	NA	1400°C/4h	98%
$CaNb_2O_6$	18.8	49600	-52.9	6.89	1350°C/2h	97.5%
	19.6	21500	+13.3	10	1400°C/2h	>95%
	14.7	22300	-22.6	NA	1400°C/2h	92%
$MnNb_2O_6$	20.9	12900	-74.3	6.77	1150°C/2h	94.1%
	22.4	34300	-59.6	10	1150°C/2h	>95%
$CoNb_2O_6$	22.0	41700	-66.6	6.67	1150°C/2h	95.6%
	22.8	11300	-44.7	10	1100°C/2h	>95%
	20	6800	-70	4	1100°C/5h	88%
$NiNb_2O_6$	22.6	40100	-38	10	1150°C/2h	>95%
	23.6	18900	-62	4.36	1300°C/4h	98%
	20.7	19800	-33	9	1300°C/2h	99.8%
$CuNb_2O_6$	17.1	7100	-45.1	7.44	1000°C/2h	92.5%

(NA = Data not available)

A-site substitution

Oxides with A = Ba, Sr; B = Zn, Mg and B′ = Nb and Ta have been found to have appropriate dielectric properties. $Ba_3ZnTa_2O_9$ was the first low loss dielectric material reported [14] for applications at microwave frequencies. Since then several studies [15,16] on related oxides have been carried out on other tantalates. These oxides crystallize in the disordered cubic structure or in a hexagonally ordered structure. Here, we discuss some substitution studies of the above perovskite related oxides, carried out in our lab.

$Ba_{3-x}Sr_xMgNb_2O_9$

To investigate the influence of the size on the A -site ion on the structural and dielectric properties, substitution of smaller Sr ion in the Ba sites in $Ba_{3-x}Sr_xMgNb_2O_9$ has been done by Thirumal *et al*[47]. At 1300 °C the entire range of oxides ($0 \leq x \leq 3$) are fully ordered as observed by x-ray diffraction and can be indexed satisfactorily on a hexagonal cell.

$Ba_{3-x}Sr_xZnNb_2O_9$

An earlier study [15] on the solid solution, $Ba_{3-x}Sr_xZnNb_2O_9$, reported possibility of ordered structures at high Sr concentration for samples sintered at 1500 °C. Single phases were obtained for all the compositions ($Ba_{3-x}Sr_xZnNb_2O_9$, $0 \leq x \leq 3$) synthesized at 1000 °C. These oxides crystallize in the
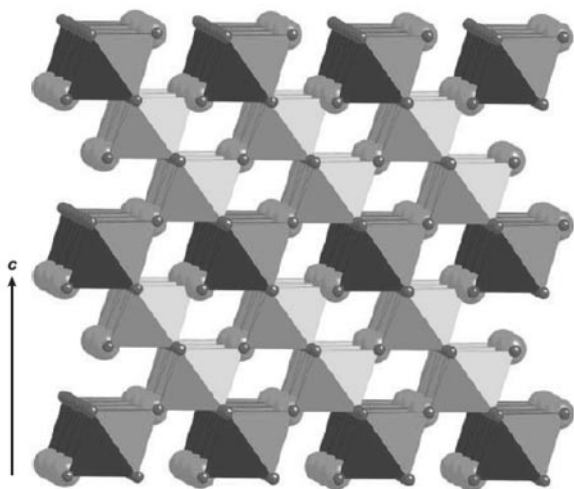
Fig. 5: 1:2-ordered $A(B_{1/3}B'_{2/3})O_3$ structure viewed along $(110)_c$ to highlight the tripled <111> layered repeat of the B and B' cation sites (adapted from Davies et al [43]).

cubic structure and their lattice parameter 'a' systematically decreases with increase in the 'Sr' concentration. The pure $Sr_3ZnNb_2O_9$ phase (x = 3) did not melt even at 1300 °C and gave an ordered hexagonal structure with lattice parameters a = 5.646(6) Å; c = 6.907(3) Å.

The dielectric constant increases with strontium concentration, from x = 0 to x = 1.0, having a maximum value around 40 for the x = 1 composition (at 500 kHz). With further increase of Sr concentration it decreases to 32 (for x = 1.25) and it remains almost constant till x = 1.75. Dielectric loss (D) remains almost constant (0.01) at 500 kHz for the entire solid solution studied.

B -site substitution

$Sr_3Zn_{1-x}Mg_xNb_2O_9$

Detailed studies[47] on $Sr_3Zn_{1-x}Mg_xNb_2O_9$ showed all the pxrd reflections could be satisfactorily indexed with a ~5.65 Å and c ~ 6.91 Å after 1300 °C. These were further heated at 1425 °C which retained the hexagonal structure. The room temperature dielectric properties on sintered pellets (1300 °C) show frequency stable dielectric constant around 20-27 for all the compositions in the 100 Hz-500 kHz range. The dielectric loss was ~0.001 for all the compositions. Dielectric constant at microwave frequencies (5.4 -5.9 GHz) for the pellets sintered at 1425 °C varies between 20-22 for various members of the $Sr_3Zn_{1-x}Mg_xNb_2O_9$ family [48]. All the samples have a low loss. The temperature coefficient of the resonant frequency is quite low varying between - 27

and + 4.3 ppm/°C. Thus our studies show that it is possible to tune the properties by suitable substitution.

$Sr_3Zn_{1-x}B_xNb_2O_9$ (B = Co, Ni and Cu)

A single phase was obtained when cobalt was substituted for zinc in SZN. The lattice parameter decreases with cobalt content. The oxides sintered at 1300 °C retained the cubic structure. Similarly copper undergoes substitution at the zinc site in SZN. However, sintering these samples at 1300 °C led to a cubic phase till x = 0.25, above which biphasic mixtures formed for all the compositions. When nickel was substituted in SZN, a limited solid solution was obtained. These oxides crystallize in the cubic structure similar to cobalt and copper substituted SZN phases. Phase analysis using powder x-ray diffraction shows single cubic phase upto x = 0.5 beyond which (x = 0.75 and 1) a 10% of $Sr_5Nb_4O_{15}$ was observed and the percentage of this secondary phase increases with increase in nickel concentration.

The dielectric properties (dielectric constant and dielectric loss) decrease with increase in frequency. For cobalt substituted the dielectric constant for the end members (x = 0.75, 1.0) at 500 kHz is 26 whereas the intermediate compositions have slightly lesser values. In case of copper and nickel similar values of dielectric constant are observed. The dielectric losses are in the range of ~ 0.03 - 0.001.

$Sr_3Mg_{1-x}B_xNb_2O_9$ (B = Co and Cu)

Cobalt undergoes substitution in strontium magnesium niobate (SMN) and all the oxides crystallize in the cubic structure and remain stable even at 1300 °C. Nickel substitution in the SMN calcined at 1000 °C also crystallizes in the cubic structure. These oxides when sintered further at 1300 °C retained the cubic cell for all the compositions except for the x = 0 and 0.25 compositions which becomes hexagonally ordered. This is evident from the appearance of 100 reflection (hexagonal cell) at d ~ 5.0 Å. Also with the increase in nickel concentration, the $Sr_5Nb_4O_{15}$ phase also increases for both calcinated and sintered oxides. Similarly copper substitution in the SMN shows that the calcinated oxides crystallize in the cubic structure. However, these oxides when sintered at 1300 °C, gets converted into ordered hexagonal system. This occurs for composition till x = 0.5. Above this composition, a biphasic mixture containing 6-8% $Sr_5Nb_4O_{15}$ is formed indicating that the Cu substitution in SMN is possible only upto x = 0.5 composition at 1300 °C.

For cobalt substituted compounds there is increase in dielectric constant from 25 - 30 with increase in cobalt concentration at 500 kHz. The dielectric loss for x = 0.25 composition is ~ 0.06 which is much less than the other compositions studied in this family. For copper substitution the dielectric constant ranges from 21 - 25 at 500 kHz. The dielectric loss varies between 0.01 - 0.002 for all compositions.

$Ba_3Zn_{1-x}B_xTa_2O_9$ (B = Mg, Ni, and Cu)

The substitution of magnesium in barium zinc tantalite (BZT) leads to a single phase for the entire composition range at 1000 °C. However, when the oxides were sintered at higher temperature (1200 °C), fully ordered structures with presence of many more superstructure reflections were obtained. The lattice parameter 'a' and 'c' do not change significantly with change in composition. Similarly nickel substitution in BZT also shows single phase till x = 0.5. Above which the secondary phase of $Sr_5Nb_4O_{15}$ start appearing and increases with the increase in nickel concentration. All the perovskite related oxides obtained at 1000 °C crystallize in the cubic structure and lead to hexagonal ordering on sintering at 1200 °C. Copper substitution in the BZT leads to pure phase for the entire family of oxides forming a solid solution. The powder x-ray diffraction data shows that all these oxides crystallize in the cubic disordered structure. Further sintering at 1300 °C retain the cubic structure with the formation of secondary phase ($Sr_5Nb_4O_{15}$) of around 10-12% in all the compositions.

The dielectric constant for all the compositions of $Ba_3Zn_{1-x}B_xTa_2O_9$ is around 30 in the 10 - 12 GHz range of frequency. These materials have very low dielectric loss, low τ_f values and reasonable dielectric constants and may also be competitive with the best materials known for microwave applications.

$Ba_3Mg_{1-x}B_xTa_2O_9$ (B = Cu and Cd)

After calcination at 1000 °C, Cd ion substitution leads to a single phase. Cu substitution gives single phase at higher Cu concentration. It was also noted that similar Cu substitution in BMN yielded pure phases at 1000 °C for the entire range. Further calcining the Cd - substituted BMT sample at 1200 °C, a secondary phase, $Ba_5Ta_4O_{15}$, started forming along with the main perovskite phase and the percentage of the phase increases with increasing Cd concentration.

$Ba_3Zn_{1-x}B_xNb_2O_9$ (B = Mg, Cu)

For both B = Mg and Cu, single phases are obtained till x = 0.75. They crystallize as cubic phases. On sintering at 1200 °C, the Cu-doped samples at x > 0.75 crystallize in the hexagonal structure. The Mg doped materials show low dielectric loss of around 0.001 at 500 kHz.

B' -site substitution

$Ba_3ZnTa_{2-x}Nb_xO_9$ and $Ba_3MgTa_{2-x}Nb_xO_9$ ($0 \leq x \leq 1$)

The PXRD patterns of oxides of the type $Ba_3ZnTa_{2-x}Nb_xO_9$ ($0 < x \leq 1$) could be indexed in a cubic cell for all the compositions sintered at 1000 °C [47]. Sintering further at 1425 °C, we observe the presence of hexagonal ordering till x = 0.5 in the $Ba_3ZnTa_{2-x}Nb_xO_9$ family. It has been earlier noted that pure $Ba_3ZnTa_2O_9$ gets hexagonally ordered[14-16] beyond 1400 °C. $Ba_3ZnTa_{2-x}Nb_xO_9$ samples sintered at 1425 °C was found to have bulk density above 96 % of the theoretical value for all compositions.

Oxides belonging to $Ba_3MgTa_{2-x}Nb_xO_9$ ($0 \leq x \leq 1$) family show the presence of a cubic phase for the materials synthesized at 1000 °C. A small amount (5%) of $Ba_5Ta_4O_{15}$ impurity phase is observed in these samples. On sintering these samples further at 1425 °C leads to a 1:2 hexagonal ordering for the entire solid solution studied. The amount of impurity phase ($Ba_5Ta_4O_{15}$) was found to be around 5 % for all the compositions.

All the compositions showed the dielectric constant of around 30 at 500 kHz in the case of $Ba_3ZnTa_{2-x}Nb_xO_9$. The dielectric constant at gigahertz frequency (5 GHz) showed a slight increase in the dielectric constant with increase in concentration of Nb. All the compositions show a very low dielectric loss (0.001-0.006) at GHz frequency. For $Ba_3MgTa_{2-x}Nb_xO_9$, the dielectric constant is in the range of 15 - 20 at 500 kHz. All the compositions show a similar dielectric behavior at GHz range as that of the $Ba_3ZnTa_{2-x}Nb_xO_9$.

Synthesis

Dielectric materials are prepared by variety of routes such as ceramic (solid state route) [49], molten flux [50], solgel [51,58,59], co-precipitation [52], reverse miceller route [53-54], vapor phase transport [55], hydrothermal methods [56], or high pressure method [57]. Other techniques which are also used in the synthesis of solids are ultra rapid quenching of materials from very high temperature, irradiation heating by intense laser beams, melting of solids by electron beam heating.

In the synthesis of ceramic materials a very important process is sintering. It is the process of obtaining highly dense and compact powder or disc at high temperature by bonding together of particles. It occurs through diffusion of atoms to eliminate high surface energy associated with the unsintered particles. The surface energy per unit volume is inversely proportional to the particle diameter. Thus, smaller particles sinter more rapidly than the bigger particles. On a microstructural scale, this bonding occurs as cohesive necks and grows at the points of contact between particles. Sintering improves properties of a material such as hardness, density, toughness, electrical conductivity, thermal expansion and the dielectric constant. However, each of these properties may show different behavior depending on the degree of sintering. Highly dense ceramic disks are required to study their properties (conductivity, dielectric constant, etc). Hence, the sintering of the disks is a necessity for the study of dielectric materials.

In addition to these techniques, other methods of synthesis are also known like microemulsion, hydrothermal, solvothermal, polymer precursor etc. These methods are mostly employed for the synthesis of nanoparticles.

Current status of other related microwave dielectric oxides

Other microwave dielectrics having complex perovskite structure include $(Ba_{(1+x)/3}La_{(2-x)/3})(Zn_{1/3}Ti_{(2-x)/3}Nb_{x/3})O_3$, $(Ba_{1/3}Ln_{2/3})(Zn_{1/3}Ti_{2/3})O_3$ (Ln = La, Pr and Nd) and $(Ba_{1/3}La_{2/3})(Zn_{1/3-x}Mg_xTi_{2/3})O_3$ possess excellent dielectric characteristics[60]. These perovskites of interest have been synthesized by solid state reaction and are found to crystallize in the cubic structure (space group *Pm3m*). Dielectric constant of the materials is found to be > 35. Among the above oxides, $(Ba_{1/3}La_{2/3})(Zn_{1/3}Ti_{2/3})O_3$ shows the best dielectric properties with quality factor (Q) of 3139 at 6.67 GHz and a temperature coefficient of resonant frequency (τ_f) of -10.8 ppm/°C. Further, the temperature coefficient of resonant frequency (τ_f) shows a large and systematic variation (with a continued decrease and a change of sign from positive to negative) with increase in Nb content. Moreover the simultaneous substitution of Ba and Nb ion at A- and B-site leads to an increase in dielectric constant which could be rationalized by using simple additive rule of the ionic polarizability.

Continuous efforts are on for identifying new dielectric materials, to cater to our future needs of faster and noise – free communication systems. Attempts to design appropriate materials by selecting various chemical compositions with novel structures have led to incredible developments. However, a complete control on the properties of the celebrated microwave materials like BZT and BMT has not been achieved yet. Problems remain, for example, volatilization of ZnO leading to formation of secondary phase[61-64] during synthesis and processing of BZT is known for decades and the major secondary phase during formation of BZT has been identified[65,66] and their dielectric properties have been reported[66] recently. The presence of ZnO helps under some conditions but also poses problems as it is well known for volatilization. The oxides without zinc for example, Ni or Mg might give some inroads in understanding the relation between structure and property, but the literature on the Ni containing BNN[67-69] phase reveals inconsistencies in structural transformation details and even in the dielectric properties. Sintering of BMT requires very high temperatures and many structural and sintering information are still challenging and interesting. The challenge in this area, at present, is in understanding the microstructural details, sintering, and cation - ordering transformations.

Other Applications

In addition to microwave dielectric properties there are tremendous applications of ternary niobates and tantalates. These applications include photocatalytic, magnetic, optical, lumniscent, piezoelctric and pyroelectric properties.

Conclusions

Various ceramic oxides having niobates and tantalates, possessing different structures and exhibiting excellent dielectric properties have been discussed along with their synthesis, substitution studies, phase stability , sintering conditions and grain size .

References

1. A. R. West, "Solid State Chemistry and its Applications", John Wiley & Sons., 1984.
2. http://news.bbc.co.uk/2/hi/africa/1468772.stm (August 1, 2001, accessed September 2008).
3. L. D. Cunningham, ''Columbium (Niobium) and Tantalum,'' US Geological Survey Minerals Year Book 2002.
4. H. Ohsato, *J. Ceram. Soc. Jpn.*, 113 (**2005**) 703.

5. Ya.G.Goroshchenko, *"Khimiya Niobiya i Tantala" (Chemistry of Niobium and Tantalum), Izd.Naukova Dumka, Kiev.,* **1965.**

6. F. Fairbrother, *"The Chemistry of Niobium and Tantalum" (Translated into Russian), Izd. Khimiya, Moscow,* **1972.**

7. G. A. Smolpnskii and N. N. Krainik, *"Segnetoelpktrikii Antisegnetoelektriki" (Ferroelectrics and Antiferroelectrics), Izd. Nauka, Moscow,* **1968.**

8. P. K. Davies, J. Tong, and T. Negas, *J. Am. Ceram. Soc.,* 80 (**1997**) 1727.

9. S. Y. Cho, K. S. Hong and K. H. Ko, *Mater. Res. Bull.,* 34 (**1999**) 511.

10. S. Kucheiko, H. J. Kim, D. H. Yeo and H. J. Jung, *Jpn. J. Appl. Phys.,* 35 (**1996**) 668.

11. M. T. Sebastian, Dielectric Materials for Wireless Communication. Elsevier Science, Oxford, U.K., 2008.

12. C. N. R. Rao, J. Gopalakrishnan and K. Vidyasagar, *Ind. J. Chem.,* A23 (**1984**) 265.

13. Y. Kobayashi and M. Miura, IEEE MTT-S *Int. Microwave Symp. Dig. San Fransico.,* 1985.

14. S. Kawashima, M. Nishida, I. Ueda, H. Ouchi and S. Hayakava, *Proc. Ferroelectr. Mater. Appl.,* 1 (**1977**) 293.

15. S. Nomura, T. Toyama and K. Kaneta, *Jpn. J. Appl. Phys.,* 21 (**1982**) L642.

16. S. Kawashima, M. Nishida, I. Ueda and H. Ouchi *J. Am. Ceram. Soc.,* 66 (**1983**) 421.

17. K. Matsumoto, T. Hiuga, K. Takada, and H. Ichimura, *IEEE Trans. Ultrason., Ferroelectr. Frequency Control,* 33 (**1986**) 802.

18. S.B. Desu and H. M. O'Bryan, *J. Am. Ceram. Soc.,* 68 (**1985**) 546.

19. H. Matsumoto, H. Tamura, and K. Wakino, *Jpn. J. Appl. Phys.,* 30, (**1991**) 2347.

20. J. Petzelt and N. Setter, *Ferroelectrics,* 150 (**1993**) 89.

21. G. Rong, N. Newman, B. Shaw, and D. Cronin, *J. Mater. Res.,* 14 (**1999**) 4011.

22. V. L. Gurevich and A. K. Tagantsev, *Adv. Phys.,* 40 (**1991**) 719.

23. S.H. Ra and P. P. Phule, *J. Mater. Res.,* 14 (**1999**) 4259.

24. T. Kolodiazhnyi and A. Petric, *J. Mater. Res.,* 17 (**2002**) 3182.

25. F. S. Galasso, Structure, Properties and Preparation of Perovskite-Type Compounds, Pergamon Press, Oxford, U.K., 1969.

26. C. Zhang, J. Wang, Z.-X. Yue, Z.-L. Gui, and L.-T. Li, *Ceram. Int.,* 30, (**2004**) 87.

27. M. Maeda, T. Yamamura and T. Ikeda, *Jpn. J. Appl. Phys. Suppl.,* 26 (**1987**) 76.

28. H. J. Lee, K. S. Hong, S. J. Kim and I. T. Kim, *Mater. Res. Bull.,* 32 (**1997**) 847.

29. H. J. Lee, I. T. Kim and K. S. Hong, *Jpn. J. Appl. Phys.,* 36 (**1997**) L1318.

30. J. H. Sturdivant, *Z. Kristallogr.,* 75 (**1930**), 88.

31. M. Maeda, T. Yamamura, and T. Ikeda, *Jpn. J. Appl. Phys.*

32. C. R. Pullar *J. Am. Ceram. Soc.,* 92, (**2009**) 563.

33. M. Thirumal and A. K Ganguli., *Proc. Indian Acad. Sci. (Chem. Sci.).,* 113 (**2001**) 603.

34. M. Thirumal, and A.K. Ganguli, *Materials Research Bulletin* 36 (**2001**) 2421.

35. Vishnu Shanker, Ashok K. Ganguli, *Bull. Mater. Sci.,* 26 (**2003**) 741

36. R. Roy, *J. Am. Ceram. Soc.,* 27 (**1954**) 581.

37. F. Galasso, L. Katz and R. Ward, *J. Amer. Chem. Soc.,* 81 (**1959**) 820.

38. F. Galasso, J. R. Barrante and L. Katz, *J. Am. Chem. Soc.,* 83 (**1961**) 283.

39. F. Galasso and J. Pyle, *J. Phys., Chem.,* 67 (**1963**) 533.

40. F. Galasso and J. Pyle., *Inorg. Chem.,* 2, (**1963**) 482.

41. F. Galasso and J.Pyle, *J. Phys. Chem.,* 67 (**1963**) 1561.

42. P. K. Davies, J. Tong and T. Negas, *J. Am. Ceram. Soc.,* 80 (**1997**) 1727.

43. P.K. Davies, H.Wu, A.Y. Borisevich, I.E. Molodetsky and L. Farber., *Annu. Rev. Mater. Res.* 38 (**2008**) 369.

44. I. Molodetsky and P. K. Davies. *J. Eur. Ceram. Soc.,* 21 (**2001**) 2587.

45. W. Hui, PhD dissertation, Univ. Penn. 2005.

46. V. M. Goldschmidt, S.N. Vindenskaps, *Akad. I. Mat. Naturv. KI,* (**1926**) 8.

47. M. Thirumal and A.K. Ganguli., *Prog. Crystal Growth and Charact.,* 44 (**2002**) 147.

48. M. Thirumal, I. N. Jawahar, K P. Surendiran, P. Mohanan and A. K. Ganguli, *Mater. Res. Bull.,* 37 (**2002**) 185.

49. M. Barwick, F. Azough and R. J. Freer, *Europ. Ceram. Soc.,* 26 (**2006**) 1767.

50. A. K. Ganguli, V. Grover and M. Thirumal, *Mater. Res. Bull.,* 36 (**2001**) 1967.

51. M. Kakihana, *J. Sol-Gel Sci. Technol.,* 6 (**1996**) 7.

52. K. Vidyasagar, J. Gopalakrishnan and C. N. R. Rao, *Inorg. Chem.,* 23 (**1984**) 1206.

53. M. P. Pileni, *J. Phys. Chem.,* 97 (**1993**) 6961.

54. S. Vaidya, P. Rastogi, S. Agarwal, S. K. Gupta, T. Ahmad, A. M. Antonelli, K. V. Ramanujachary, S. E. Lofland and A. K. Ganguli, *J. Phys. Chem. C.,* 112 (**2008**) 12610.

55. Y. Zhang, K. Yu, S. Ouyang and Z. Zhu, *Mater. Lett.,* 60 (**2006**) 522.

56. Y. J. Ma, J. H. Cho, Y. H. Lee and B. I. Kim, *Mater. Chem. and Phys.,* 98 (**2006**) 5.

57. G. V. Bazuev, T. I. Chupakhina, V. G. Zubkov, A. P. Tyutyunnik, Y. G. Zainulin, E. A. Neifeld and N. I. Kadyrova, *Mater. Res. Bull.,* 41 (**2006**) 804.

58. M. P. Pechini, U. S. Pat., 330 (**1967**) 697.

59. P. R. Arya, Pika Jha and A. K. Ganguli, *J. Mater. Chem.,* 13 (**2003**) 415.

60. S. L. Samal, G. L. N. Rao, K. C. James Raju, and A. K. Ganguli., Jpn. *J. Appl. Phys.* 48 (**2009**) 061401.

61. S. B. Desu and H. M. O'Bryan *J. Am. Ceram.Soc.,* 68, (**1985**) 546.

62. J-I. Yang, S. Nahm,C-H Choi, H-J Lee, and H-M Park, *J. Am. Ceram. Soc.,* 85, (**2002**) 165.

63. V. Tolmer and G. Desgardin, *J. Am. Ceram. Soc.,* 80, (**1997**) 1981.

64. S. J. Webb, J. Breeze, R. I. Scott, D. S. Cannell, D. M. Iddles, and N. McN. Alford, *J. Am. Ceram. Soc.,* 85, (**2002**) 1753.

65. P. K. Davies, A. Borisevich and M. Thirumal, *J. Eur. Ceram. Soc.,* 23, (**2003**) 2461.

66. M. Thirumal and P. K. Davies, *J. Am. Ceram.Soc.,* 88, (**2005**) 2126.

67. J. K. Park and D.Y. Kim, *J. Am. Ceram. Soc.,* 84, (**2001**) 218.

68. T. Kolodiazhnyi, A. Petric, A. Belous, O. V'yunov, and O. Yanchevskij, *J. Mater. Res.,*17, (**2002**) 3182.

69. M. Thirumal and P. K. Davies, unpublished results.

Materials Chemistry Aspects in Pyrochemical Reprocessing

Suddhasattwa Ghosh, B. Prabhakara Reddy and K. Nagarajan*

Fuel Chemistry Division, Chemistry Group,
Indira Gandhi Centre for Atomic Research, Kalpakkam 603 102, Tamilnadu, India
*Corresponding Author; email: knag@igcar.gov.in

Abstract

Molten salt electrorefining, the pyrochemical process ideally suited for reprocessing spent metal fuels of Fast Breeder Reactors is based on the differences among the thermodynamic stabilities of the chlorides of fission products and fuel materials, U and Pu. In this process, carried out at 773 K, spent metallic fuel of U-Pu-Zr alloy is used as the anode and the eutectic salt of LiCl-KCl is used as the electrolyte. There are two options for the cathode: either a solid rod or liquid cadmium can be used as the cathode depending on the need to selectively recover U or recover U and Pu together. Process modelling is based on thermodynamic equilibria existing at the interfaces between anode and electrolyte and cathode and electrolyte. By proper choice of cathode material, separation between lanthanides and actinides can be enhanced. Metal fuel cycle involves reduction of actinide oxides to their metals. Direct electrochemical reduction process for actinide oxides in molten salt electrolytes has been developed in the recent years. The material chemistry aspects of all the processes are discussed in this paper.

Keywords: reprocessing, electrorefining, modelling, direct oxide reduction

Introduction

Nuclear fuel reprocessing constitutes the key step in the nuclear fuel cycle in which valuable fuel materials, uranium and plutonium, are recovered from the irradiated fuel for use in refabrication into fuel for irradiation. The various reprocessing methods achieve the separation of the fuel materials from the fission products by exploiting the differences among the physical or chemical properties of their compounds. Reprocessing methods could be broadly classified into aqueous and non-aqueous methods. PUREX process, based on the solvent extraction using n-tributyl phosphate (TBP), is an aqueous process and by far the largest commercial experience exists only with this process [1]. Several non-aqueous processes, employing molten salts and molten alloys, have been developed so far. They include: the Fluoride Volatility process, based on the differences in the volatilities of the fluorides [2], Salt Transport Process using the equilibration between magnesium alloys and magnesium chloride based salts[3], Melt Refining Process in which the fuel is heated in a zirconia crucible at 1673 K etc. However, many of these methods have not been developed beyond laboratory scale. Only three methods are currently under serious consideration in various countries in the world for implementation for future commercial plants and they are: the molten salt electrorefining process ideally suited for processing metallic fuels [4], oxide electrowinning process for oxide fuels[5] and the fluoride volatility process combined with electrochemical reduction in fluoride salts [6]. The major advantages of the non-aqueous processes are: (a) compatibility with the higher radiation levels encountered with the irradiated fuels cooled for a shorter duration, owing to the use of molten salts and alloys , (b) less criticality problems due to the absence of aqueous reagents, (c) ability to handle larger amounts of fuel materials for a given process volume than the aqueous processes resulting in more compact plants and the associated advantages such as less cost, potential for co-location with reactors etc. (d) inherent proliferation resistance due to co-processing of uranium, plutonium and minor actinides (Np, Am, Cm) (e) less problems in waste management due to the lower waste volume which is mostly in the form of solid as well as absence of minor actinides from waste. However, the process technology is rendered complex by the use of high temperatures and corrosive chemicals and the selection of materials for the process vessels and equipment for these processes needs to take into account several materials chemistry aspects. Molten salt electrorefining, as mentioned earlier, is the most suited one for treating spent metallic fuels. The strategy for meeting the growing energy demand in our country envisages the introduction of metal fuelled fast breeder reactors (FBRs) in the commercial domain after 2020 so that fuel doubling time is brought down. Hence

development of the molten salt electrorefining process and the associated technology is very important. The materials chemistry aspects of this pyrochemical reprocessing method will be discussed in this paper.
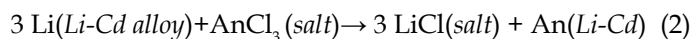
Molten salt electrorefining process

A schematic diagram of for the molten salt electrorefining process is shown in Fig.1 [7]. In this process, the fuel materials, U and Pu are separated from the spent metallic fuel by exploiting the differences in the thermodynamic stabilities of the respective chlorides. The spent metallic fuel, contained in a perforated basket serves as the anode of the electrorefining cell, operated at 773 K and LiCl-KCl eutectic salt in which small amount of UCl_3 and $PuCl_3$ are initially loaded is the electrolyte. Due to the large negative Gibbs energies of formation of the alkali, alkaline earth and rare earth chlorides, these fission product metals in the spent metal anode are easily oxidized and get transferred to the electrolyte salt. These fission products prefer to stay in the electroyte as chlorides as they are more difficult to be reduced, again due to the large thermodynamic stability. The noble metals as well as the components of the steel cladding, such as Fe and Cr require higher anode potentials for oxidation and so, remain unoxidised in the anode. The chlorides of the fuel materials, U and Pu along with that of the minor actinides, Np, Am etc. are of intermediate thermodynamic stability and hence these metals in the spent fuel get oxidized to form the chlorides, go to the salt phase and are also reduced at the cathode, there by getting deposited as metals on the cathode. With respect to the cathode, there are two options: (a) a solid rod or (b) liquid cadmium. When a solid rod is used as the cathode, it results in the selective deposition of U whereas liquid cadmium cathode enables co-deposition of U and Pu. Thermochemistry plays a role in the difference between the deposition behaviours on the two cathodes. If the following equilibrium reaction is considered to occur at the electrolyte salt/cathode interface,

Pu (*cathode*) + UCl_3 (*salt*) ↔ U (*cathode*) + $PuCl_3$ (*salt*)   (1)

In the case of solid cathode, the equilibrium constant for the above reaction is merely dictated by the difference between the Gibbs energies of formation of the two chlorides, as the activities of the metals are unity and the activity coefficients of the two chlorides in the electrolyte are also unity, their mole fractions being almost equal. Thus the equilibrium constant is of the order of 10^6. However, in the case of liquid cadmium cathode, the activity coefficients

of U and Pu are 88 and 10^{-2} respectively, virtually bringing down the equilibrium constant to a value of 1 enabling co-deposition of U and Pu. In the recent years, the thermochemical interaction of the cathode material with the actinides and lanthanides has been brought into play in achieving better separation between the two groups of metals. Instead of a non-reactive metal rod, aluminium which has higher affinity for actinides than lanthanides has been used as the cathode rod and larger separation factors have been reported [8].The complete flow sheet for the reprocessing of metallic fuels using the molten salt electrorefining process is shown in Fig. 2. In this process flow sheet, the electrorefining step is followed by "consolidation step" in which the U deposited on the solid cathode is separated from the salt occluding it by distilling off the salt and then it is melted. Similarly, U and Pu deposited on the cadmium cathode are separated from cadmium by distilling of cadmium and then they are melted. After a few batches of the spent metal fuel are reprocessed, the electrolyte salt gets loaded with large amounts of the fission product chlorides which would raise the solidus temperature of the salt above the process temperature and also increase the heat load due to the decay heat from the lanthanide fission products. Hence the salt is purified from the fission products by passing it through a zeolite column and recycled and the impurities are sent for disposal as waste. However, the actinide chlorides in the salt must be removed from the salt before purification for which equilibration with Li-Cd alloy is used. This process is also based on the relative stabilities of lithium chloride and the actinide chlorides.Lithium reduces the actinide chlorides to the respective metals that are extracted into the alloy phase.

3 Li(*Li-Cd alloy*)+$AnCl_3$ (*salt*)→ 3 LiCl(*salt*) + An(*Li-Cd*) (2)

These actinide metals are reoxidised to their chlorides and loaded into the electrolyte salt for the next batch processing by using cadmium chloride as the oxidant.

Studies on the molten salt electreorefining of alloys of U such as U-Zr, U-Ce-Pd etc. were carried out in our laboratory using an argon atmosphere laboratory scale facility that houses the equipment for the studies on all the unit operations of the process flow sheet [9]. Studies on electrorefining of plutonium are in progress. Fig.3. shows the electrorefining cell in the laboratory scale facility and the plutonium metal deposited on a solid cathode. An engineering scale facility for pyroprocess studies on kg scale

has been set up and commissioned in which experience with bulk processing as well as remotisation of the process will be generated. Electrorefining experiments using kg amounts of U alloys are being carried out in this facility.

Fig.4 shows the engineering scale facility and the U metal deposit on a solid cathode. It incorporates a power
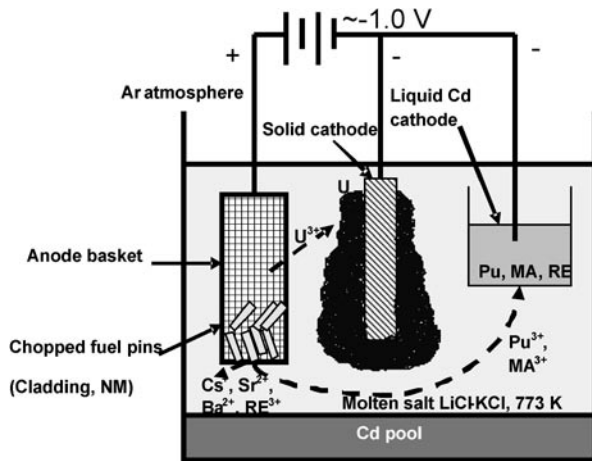

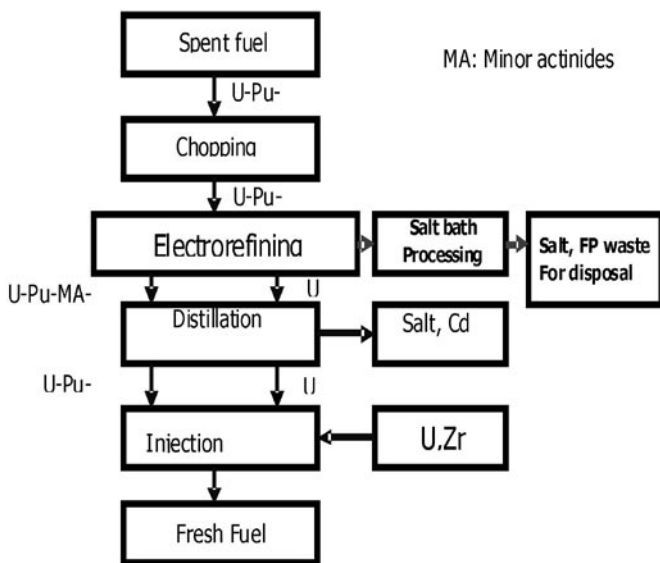Fig.1: Schematic diagram of the electrorefining process

Fig.2: Process flow sheet of the molten salt electrorefining process

manipulator and an in-cell crane tfro enabling remote operation of the equipment. The operational experience will help in designing a reprocessing plant for the processing the spent metal fuels from the Fast Breeder Test Reactor (FBTR) at Kalpakkam.

Fig. 3: Electrorefining cell and the deposit of plutonium on solid cathode

Thermochemical modelling of the molten salt electrorefining process

Modelling the molten salt electrorefining process is necessary not only for understanding the process but also for predicting the behaviour of the system under various process conditions. Two groups of models, one based on thermochemistry [10] and the other based on electrokinetics [11] have been reported in the literature. The models based on thermochemistry are based on the chemical equilbria among pairs of metals in the anode/cathode and their chlorides in the salt. In an electrorefining cell having liquid cadmium as the anode and cathode, the equilibria for the U and Pu elements can be represented by the following equation:

$$UCl_3 \, (salt) + Pu \, (Cd) = PuCl_3 \, (salt) + U \, (Cd) \qquad (3)$$
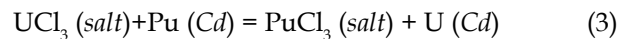
$$\frac{a_{U,Cd} \cdot a_{PuCl_3,salt}}{a_{Pu,Cd} \cdot a_{UCl_3,salt}} = K_{eq} = \exp(-\Delta G_R^0 / RT) \qquad (4)$$

where $\Delta G°_R$ is the Gibbs energy change for the above reaction. The terms **a** in the above equations and n in equation 5 refer to the activity and number of moles, respectively of the specified components. Since both the Cd electrodes are in equilibrium with the same salt phase, the following equation can be deduced

$$\left(\frac{n_{U,anode}}{n_{Pu,anode}} \right) = \left(\frac{n_{U,cathode}}{n_{Pu,cathode}} \right) \qquad (5)$$
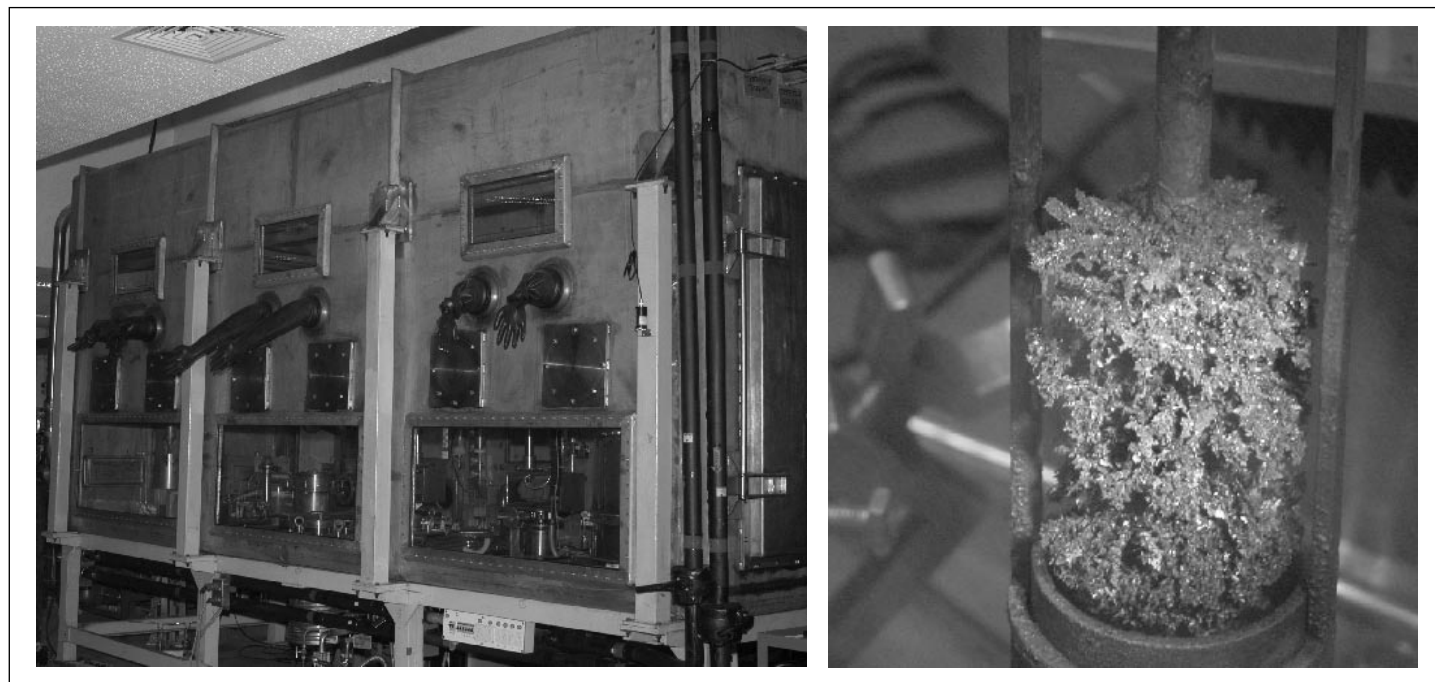
Fig. 4: Engineering scale demonstration facility and the U metal deposit on a solid cathode

This condition called "equal EMF condition", is based on the consideration that the ratio of the activities of U and Pu in the anode is equal to that in the cathode rather than the activities of individual metals being equal, as in classical equilibrium considerations.

A code PRAGAMAN has been developed [12] for the numerical simulation of the electrotransport behaviour of uranium and plutonium in the electrorefining cell. It is based on a system of non-linear equations arrived at using mass balance and thermodynamic equilibria considerations which are solved using Matlab to arrive at the concentration profiles of eight elements and their chlorides in the anode, salt and cathode phases. It takes into account the various conditions of solubility that can exist in the anode and cathode due to the amounts of fuel material being processed and the amounts of anode and cathode cadmium. Fig. 5(a) and (b) show the results of computation using the code for a typical scenario in which the anode cadmium is initially saturated with U but unsaturated with Pu.

Under these conditions, rate of U transport to cathode dominates over that of Pu, as is evident from Fig. 5a. Between point (a) and (b), both the electrodes are saturated with U and during this time only U gets transported, as is evident from Fig 5a. After (b), the anode becomes unsaturated
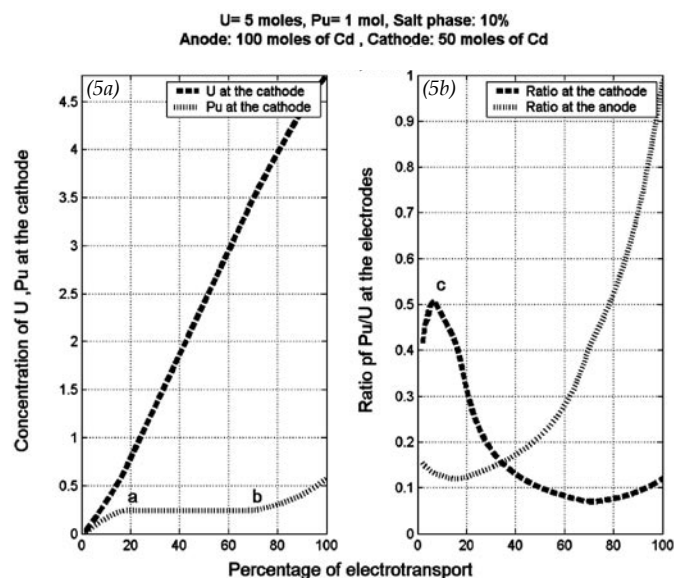

Fig. 5: Computational results for the electrotransport of U and Pu

with U and again the transport of Pu commences. But still the rate of transport of U dominates over that of Pu to the cathode. The computations also show that the amount of U and Pu transported to the cathode get slightly enhanced in the presence of lanthanide fission products and minor actinides.

Selection of materials for pyroprocess applications

In the electrorefining process flow sheet developed by ANL, USA, any solid metal rod was proposed as the cathode for separation of U and Pu and liquid cadmium for co-recovery of the two. One of the difficulties faced in making the reprocessing by electrorefining a continuous one rather than a batch process is the step of removing the deposit on the cathode rod by scrapping. Investigations using graphite rod as the cathode have shown that by periodically applying mechanical vibrations the deposit gets removed easily which makes the process amenable for automation. In the electrorefining process, a significant amount of the lanthanide fission products are also deposited along with the actinides that go into the refabricated fuel. In view of the lower absorption cross sections of the lanthanides in the fast spectrum, this was not held against the process. However, it would be still desirable, if better separation of lanthanides and actinides is achieved. Recent studies at ITU, Germany, using solid aluminium rod cathode have shown that higher stabilities of actinide-aluminium compounds compared to that of lanthanide-aluminium compounds help to achieve higher separation factors for lanthanides. When the materials for the process equipment are considered, one has to take into account the fact that liquid cadmium is being used and hence materials that would come into contact with cadmium should be free from nickel due to the high solubility of nickel in cadmium. Hence 430 steel or Cr-Mo steels are used for making container materials for the process. The consolidation step of distilling the salt/cadmium followed by melting the actinide metals is done in a graphite crucible. As graphite could react with the uranium and plutonium metals, generally, a coating of yttrium oxide or aluminium oxide is given inside the graphite crucible. The refabrication of metallic fuels is carried out by injection casting in which quartz tubes are used as moulds. To prevent the chemical interaction between the actinide metals and quartz, the inner walls of quartz are coated with zirconium oxide or yttrium oxide which are highly stable and do not react with U metal.

It is well known that chloride salts are highly hygroscopic and readily absorb moisture. Hence the pyroprocess facility has to be maintained under high purity inert atmosphere containing only vppm amounts of moisture and oxygen. Further, commercially available LiCl and KCl have to be purified to remove any residual moisture and melted under a flowing chlorine gas to form the eutectic. This is necessitated because the chlorides react with moisture to form hydroxides of Li and K which on heating would form the respective oxides that would not melt at 773 K and also interfere with the process. Hence treating them with chlorine will reconvert the hydroxides, if any, into the respective chlorides.

References

1. M. Benedict, T. Pigford, **1957**, *Nuclear Chemical Engineering*, McGraw Hill, Chapter 2.

2. J. Uhlir, M. Hron, V. Priman and Z. Valvoda, *Proceedings of the 7th OECD/NEA International Information Exchange Meeting on Actinide and Fission Product Partitioning and Transmutation*, Jeju, Japan, 14-16 october **2002**.

3. Johnson, *J.Nucl.Mater.*, 51 (**1974**) 163.

4. C.E. Stevenson, *The EBR-II Fuel Cycle Story*, American Nuclear Society, **1986**A.V. Bychkov,, *Chemical Separation Technologies and Related Methods of Nuclear Waste Management*, ed. G.Choppin, Kluwer, p 301,

5. NATO Science Series, 2, Environmental security, Vol 53.

6. F. Lisy, P. Soucek, and R. Zvejskova, *Proceedings of GLOBAL 2001*, Paris, France, 9-13 September **2001**.

7. T. Inoue, *Proc. International Pyroprocessing Research Conference (IPRC 2006)*, Idaho National Laboratories, Idaho, USA, 6-8 August, **2006**.

8. P. Souček, L. Cassayre, R. Malmbeck, E. Mendes, R. Jardin and J.P. Glatz, *Radiochim. Acta.*, 96 (**2008**) 315.

9. K. Nagarajan, T. Subramanian, B. Prabhakara Reddy, P.R. Vasudeva Rao and Baldev Raj, *Nucl. Tech*,162 (**2008**) 59.

10. Johnson, *J. Nucl.Mater.*, 154 (**1988**)169.

11. T. Kobayashi and M. Tokiwai M., *J.Alloys.Comp.*, 197 (**1993**) 7.

12. Suddhasattwa. Ghosh, B. Prabhakara Reddy, K.Nagarajan and P.R. Vasudeva Rao, *Nucl. Tech* 170 (**2010**) 430.

Major Material Characterization Techniques at BARC

Technique	Nature of information obtained	Division in which the facility is available in BARC
Transmission Electron Microscope (TEM)	Size, morphology, crystal structure of the nanomaterials. Nature of grain boundaries, their orientation etc	Materials Science Division
Scanning Electron Microscope with EDAX facility	Morphology of thin films. Nature of grain and grain boundaries in materials like alloys, nano composites etc.	Chemistry Division Technical Physics Division Materials Science Division
Electron probe micro analysis (EPMA) and imaging	Phase separation in glassy materials. Information regarding the Interface existing between different phases in the glassy materials.	Materials Science Division
Secondary Ion Mass spectrometer	For characterising the surface of different materials and depth profiling	Technical Physics Division
Atomic Force Microscope (AFM)	Morphology, Surface roughness	Chemistry Division Fuel Chemistry Division Applied Spectroscopy Division
Scanning Tunneling microscope (STM)	Imaging of the conducting surfaces, I-V characteristics the conducting and semiconducting thin films	Chemistry Division Applied Spectroscopy Division
Atomic Force Acoustic Microscopy	Thin film elastic and viscoelastic properties, stress, strain, bulk modulus	Applied Spectroscopy Division
Scanning Near-field Optical Microscopy (SNOM)	Morphology, thin film compositions	Applied Spectroscopy Division
Metallurgical microscope	Microstructure of solids	Fuel Chemistry Division
X-ray photoelectron spectroscopy (XPS), Auger Electron Spectroscopy (AES), Ultra Violet Photoelectron spectroscopy (UPS)	Oxidation state of the elements. Chemical nature of the elements or ions present on the surface of different materials.	Technical Physics Division
X-ray fluorescence (ED-XRF & TXRF)	Composition of materials	Fuel Chemistry Division Analytical Chemistry Division
X-ray diffractometer (with high temperature facility)	Identification of different crystalline phases, studies involving phase transitions	Chemistry Division Fuel Chemistry Division
Single crystal X-ray diffractometer	Structural elucidation of organic molecules and organo-metallic complexes	Chemistry Division
Small Angle X-ray Scattering instrument	For understanding the short range order existing in a variety of soft condensed materials	Solid State Physics Division
EXAFS and ARPES synchrotron beamline	Material physics and chemistry studies	Applied Spectroscopy Division

Grazing Incidence X-ray reflectrometer (GIXR)	Thin film roughness, thickness, multilayer interface, material density	Applied Spectroscopy Division
Static and dynamic light scattering	Dynamics of different micellar systems and surfactants	Chemistry Division Fuel Chemistry Division
Neutron diffractometer	Understanding the crystal structure of organic and inorganic materials. Information regarding magnetic interactions in different materials.	Solid State Physics Division
Small Angle Neutron scattering Instrument	For understanding the short range order existing in a variety of soft condensed materials	Solid State Physics Division
Positron Annihilation Spectroscopy	To understand the nature of defect centres present in a variety materials like semiconductors, polymers etc.	Radiochemistry Division
Perturbed angular Correlation (PAC)	PAC can discriminate among local environments of probe atoms in solids. Internal fields in solids exert torques on nuclear moments. Such interactions lead to frequencies of precession of probe nuclei that are proportional to the internal fields and are characteristic of the probe's lattice location.	Radiochemistry Division
Fe^{57} Mossbauer spectroscopy	Environment around Fe^{3+} in different magnetic materials and inorganic complexes	Solid State Physics Division
Photo Acoustic Spectrometer	Band gap of powder materials	Radiochemistry Division
Steady-state and time-solved luminescence instrument	Luminescence from all kinds of samples over the region of UV-Visible and NIR region (230-1700 nm). Lifetimes can be measured in the range of few nano seconds to few milli seconds.	Chemistry Division
Thermoluminescence reader	Thermoluminescence property of solid state materials	Food Technology Division
FTIR spectrometer	Structural information from different vibrational modes of groups or bonds present in different materials	Chemistry Division Fuel Chemistry Division
Raman Spectrometer	Structural information from different vibrational modes of groups or bonds present in different materials	Chemistry Division High Pressure Physics Division Material Science Division
Electron paramagnetic resonance (EPR) & Electron-nuclear double resonance (ENDOR) spectrometer	Structural environment around paramagnetic centres	Radiochemistry Division Food Technology Division
NMR	Structural information	Bio-organic Division
Vibrating sample magneto meter	Magnetic properties of materials	Chemistry Division Solid State Physics Division

SQUID magneto meter	Magnetic properties of materials	Technical Physics Division
Differential Scanning calorimeter (DSC)/Modulated DSC/ Thermo gravimetric instruments	Information regarding the heat changes involved in chemical reactions	Chemistry Division Fuel Chemistry Division Materials Science Division
Thermo-mechanical analyzer	Thermal expansion coefficients of solids	Chemistry Division Technical Physics Division Radio-Analytical Chemistry Division
Temperature programmed desorption/reduction/oxidation instrument	Gas adsorption/desorption and redox characteristics of different materials	Chemistry Division
Electrical conductivity set up for measuring both AC and DC electrical conductivity	Conduction mechanism in different materials	Chemistry Division
AC-Impedance Analyzer	Ionic conductivity and dielectric properties of solids	Chemistry Division
Surface area and Pore size analyzer	To measure the surface area and pore size distribution of powder samples	Chemistry Division Fuel Chemistry Division
Mercury porositimetry	Porosity and pore size distribution	Fuel Chemistry Division
Stereo pycnometer (He)	Density of solids	Fuel Chemistry Division
Gas Chromatograph (GC)	Analysis of gas mixtures Product analysis of a heterogeneous catalytic process	Chemistry Division Radiation & Photochemistry Division Analytical Chemistry Division
GC-MS	Analysis of gas mixtures and for product identification in a chemical process.	Radiation & Photochemistry Division Bio-organic Division
Ellipsometer (Phase modulated)	Thickness of thin films	Applied Spectroscopy Division
Vickers hardness	Micro-hardness values of different materials	Technical Physics Division
Hydrogenation set up	Kinetics of Hydrogen absorption by materials	Chemistry Division
Diamond Anvil cells	High pressure behaviour of materials	High Pressure Physics Division
Zeta Potential Analyzer	Surface Charge	Analytical Chemistry Division
PE Hysteresis, Piezo-electric measurement facility	For ferroelectric and Relaxor Materials	Chemistry Division

News and Forthcoming Events

Year 2011 is being celebrated as International Chemistry Year throughout the world.

Some of the international conference being organised in the year 2011 are:

1. DM-ISEAC-2011, 4th ISAEC International Discussion Meet on Electrochemistry and its Applications, Feb 7-10 2011, Mascot Hotel Thiruvantapuram Kerala, India, http://www.iseac.org; e-mail: editoriseac@gmail.com

2. Hybrid Materials 2011, 6-10 March, Strasbourg, France; www.hybridmaterialsconference.com

3. 46th EUCHEM Conference on Stereochemistry, 1-6 May, Brunnen, Switzerland. jerome.lacour [at] unige.ch

4. Colloids and Materials, 8-11 May , Amsterdam, Netherlands, www.colloidsandmaterials.com

5. International Conferences on Materials for Advanced Technologies (ICMAT 2011), 26 June-1 July, Singapore. http://www.mrs.org.sg/icmat2011/

6. 10th International Symposium on Materials Chemistry (MC-10), 4-7 July, Manchester UK. http://www.rsc.org/ConferencesAndEvents/RSCConferences/MC10/

7. 22nd International Symposium: Synthesis in Organic Chemistry, July 11-14, Chrichill, U.K. www.csj.jp/kenkyu/confall.html

8. 18th International Conference on Composite Materials (ICCM 18) Jeju Island, Korea, August 21-26, http://iccm18.org/

9. Nanopolymer 13-14, Sept., Düsseldorf, Germany. www.ismithers.net/conferences/XNAN11/nanopolymers-2011

Achievements, Honours and Awards received by the SMC members

Name of the member & affiliation	Name of the award/honour	Conferred by
Dr. S. N. Achary *BARC, Mumbai*	TA-ITAS Young Scientist Award	Indian Thermal Analysis Society
Dr. S.R. Bharadwaj *BARC, Mumbai*	"Regional Editor - INDIA" for Journal of Thermal Analysis and Calorimetry	Springer
Dr. Amreesh Chandra *IIT, Kharagpur*	Max Planck India Fellowship Award	Max-Planck Society, Germany
Dr. P. Sujatha Devi *CGCRI, Kolkata*	P. K. Kunju Sahib Memorial award for Excellence in Chemistry	M.S.M. College, Kayamkulam, Kerala
Prof. Ashok K. Ganguli *IIT, Delhi*	Fellow of Indian Academy of Sciences	Indian Academy of Sciences, Bangalore
Dr. C. S. Gopinath *NCL, Pune*	CNRS Professorship	CNRS, France
Dr. Vinita Grover Gupta *BARC, Mumbai*	DAE-Young Scientist Award	Department of Atomic Energy
Prof. Prafulla K. Jha *Bhavnagar University, Bhavnagar*	Regular Associateship	Abdus Salam International Center for Theoretical Physics,Trieste, Italy
Dr. G. P. Kothiyal *BARC, Mumbai*	Life Time Achievement Award	An Educational Trust (KBE Chanshetti Guruji Pratishan, Solapur)
Dr. C. Majumder *BARC, Mumbai*	Fellow, Maharashtra Academy of Sciences	Maharashtra Academy of Sciences
Dr. T. Mukherjee *BARC, Mumbai*	Acharya P. C. Ray Memorial Lifetime Achievement Award	Indian Chemical Society
Dr. R. S. Ningthoujam *BARC, Mumbai*	Young Associate, Maharashtra Academy of Sciences	Maharashtra Academy of Sciences
Dr. M.R. Pai *BARC, Mumbai*	Young Associate, Maharashtra Academy of Sciences	Maharashtra Academy of Sciences
Dr. Pankaj Poddar *NCL, Pune*	Scientist of the Year	NCL Research Foundation
Dr. Sunil Sabharwal *BARC, Mumbai*	INS Award	Indian Nuclear Society, Mumbai
Dr. Pramod Sharma *BARC, Mumbai*	DAE-Young Scientist Award	Department of Atomic Energy
Kartik N. Shinde *RTM Nagpur University, Nagpur*	Young Scientist Award	Bhartiya Vigyan Sammelan, SEES, Indore
Dr. A. K. Tyagi *BARC, Mumbai*	R. D. Desai Memorial Award	Indian Chemical Society
	Rajib Goyal Prize in Chemical Sciences	Kurukshetra University
	DAE-SRC Outstanding Researcher Award	Department of Atomic Energy

In this issue

Feature articles